Title

Towards Multi-Fidelity Simulation of Dynamic Stall: Numerical Simulation and a Variational Formulation of Vortex Dynamics

Author

Khalifa, Nabil M

Publication Date

2024

Peer reviewed|Thesis/dissertation

UNIVERSITY OF CALIFORNIA,
IRVINE

Towards Multi-Fidelity Simulation of Dynamic Stall: Numerical Simulation and a Variational Formulation of Vortex Dynamics

DISSERTATION

submitted in partial satisfaction of the requirements
for the degree of

DOCTOR OF PHILOSOPHY

in Mechanical and Aerospace Engineering

by

Nabil Mamdouh Mohamed Mahmoud Khalifa

Dissertation Committee:
Associate Professor Haithem E. Taha, Chair
Professor Dimitri Papamoschou
Professor Peter Taborek
Professor Arash Kheradvar

2024

DEDICATION

This thesis is dedicated to my beloved family, whose unwavering support and encouragement have been the cornerstone of my achievements. To my friends, whose companionship and understanding have made this journey more meaningful and memorable. And above all, to Allah, whose infinite wisdom and guidance have illuminated my path and bestowed upon me the strength and perseverance to reach this milestone

TABLE OF CONTENTS

LIST OF FIGURES

LIST OF TABLES

Page

ACKNOWLEDGMENTS

I would like to thank my wife, mother, family, friends, and my lab colleagues for their support throughout this journey. Also, I am grateful to my advisor for facilitating one of the best PhD experiences ever, including academic guidance and personal and professional mentoring.

This work is made possible by the support of: National Science Foundation grants CMMI-1846308 and CBET-2005541 and Air Force Office of Scientific Research award FA9550-19-1-0126.

VITA

Nabil Mamdouh Mohamed Mahmoud Khalifa

EDUCATION

Doctor of Philosophy in Mechanical and Aerospace Engineering **2024**
University of California, Irvine *Irvine, CA*

Master of Science in Aerospace Engineering **2018**
Cairo University *Giza, Egypt*

Bachelor of Science in Aerospace Engineering **2013**
Cairo University *Giza, Egypt*

RESEARCH EXPERIENCE

Graduate Research Assistant **2019–2024**
University of California, Irvine *Irvine, CA*

TEACHING EXPERIENCE

Teaching Assistant **2019–2024**
University of California, Irvine *Irvine, CA*

REFEREED JOURNAL PUBLICATIONS

Vortex dynamics: A variational approach using the principle of least action **2024**
Physical Review Fluids

On computational simulations of dynamic stall and its three-dimensional nature **2023**
Physics of Fluids

Geometric-control formulation and averaging analysis of the unsteady aerodynamics of a wing with oscillatory controls **2021**
Journal of Fluid Mechanics

REFEREED CONFERENCE PUBLICATIONS

Variational Formulation of Vortex Dynamics **2022**
AIAA SCITECH 2022 Forum

Geometric Control Study of the Beddoes-Leishman Model in a Pitching-Plunging Airfoil **2022**
AIAA SCITECH 2022 Forum

Static and dynamic characteristics of the aerodynamic forces on pitching airfoils between 0 to 360 degrees angle of attack **2022**
AIAA SCITECH 2022 Forum

Compressible unsteady aerodynamic loads on oscillating airfoils in a subsonic flow **2022**
AIAA SCITECH 2022 Forum

Comparing the performance of different turbulence models in predicting dynamic stall **2021**
AIAA SCITECH 2021 Forum

ABSTRACT OF THE DISSERTATION

Towards Multi-Fidelity Simulation of Dynamic Stall: Numerical Simulation and a Variational Formulation of Vortex Dynamics

By

Nabil Mamdouh Mohamed Mahmoud Khalifa

Doctor of Philosophy in Mechanical and Aerospace Engineering

University of California, Irvine, 2024

Associate Professor Haithem E. Taha, Chair

This Dissertation investigates the three-dimensional nature of dynamic stall and introduces a new variational formulation for vortex dynamics, both contributing to a deeper understanding of aerodynamic phenomena. The first part of the research involves numerical simulation of the flow around a harmonically pitching NACA 0012 airfoil using Unsteady-Reynolds-Averaged Navier–Stokes (URANS) and Detached Eddy Simulation (DES) solvers, including Delayed-DES (DDES) and Improved-DDES (IDDES). Both two- and three-dimensional simulations are conducted, with results compared against experimental measurements. It is found that three-dimensional simulations, particularly those using DES solvers, outperform two-dimensional ones in capturing the different stages of dynamic stall and predicting the lift dynamics. The IDDES simulations, which are inherently three-dimensional, accurately model the cascaded amalgamation of vortices forming the dynamic stall vortex, supporting the hypothesis that dynamic stall is intrinsically a three-dimensional phenomenon.

Since the complex flow in dynamic stall is mainly related to vortex-vortex interactions, richer models of vortex dynamics are needed to develop a reduced-order model for dynamic stall in the future. For this goal, the second part of the study introduces a new variational formulation for vortex dynamics based on the principle of least action. Unlike the traditional Kirchhoff-Routh (KR) function, which

describes vortex dynamics through first-order differential equations of motion derived from the Biot-Savart law, this new formulation results in second-order differential equations that define vortex accelerations. This leads to more complex dynamics, such as unique patterns formed by equal-strength, counter-rotating vortices with different initial velocities. Moreover, the new model can incorporate arbitrary external body forces; when an electrodynamic force is considered, it reveals rich, counter-intuitive behaviors that cannot be captured by the KR formulation.

Chapter 1

Introduction

The dynamic stall phenomenon typically arises when an airfoil undergoes a rapid change in its angle of attack near the static stall angle [Visbal and Garmann, 2018, McCroskey et al., 1976]. This phenomenon is marked by a significant flow separation, followed by reattachment at various stages of the cycle. The different stages of dynamic stall are depicted in fig. 1.1 in chronological order. Over the past few decades, dynamic stall has been extensively researched, starting from the early works of McCroskey, Carr, and McAlister [McCroskey et al., 1976, McCroskey, 1981, 1982, Carr, 1988], to more recent studies by Visbal [Visbal, 2014, Visbal and Garmann, 2018, 2019] and Ansell [Gupta and Ansell, 2018]. Numerous studies have reported the potential for lift modeling and enhancement by leveraging dynamic stall [Taha et al., 2021, Pla Olea et al., 2022, Pla Olea and Taha, 2024, Zakaria et al., 2017, Hassan and Taha, 2020]. Moreover, dynamic stall is prevalent in various applications, including helicopters [Leishman, 2006], wind turbines [Larsen et al., 2007], energy harvesting [dos Santos et al., 2021, Deb et al., 2020], and high-speed flow applications [El-Nadi et al., 2022].

Numerous experimental studies [McCroskey et al., 1976, McCroskey, 1981, Carr, 1988, Mulleners and Raffel, 2013, Gupta and Ansell, 2018] have examined the effect of Reynolds number (Re) on the

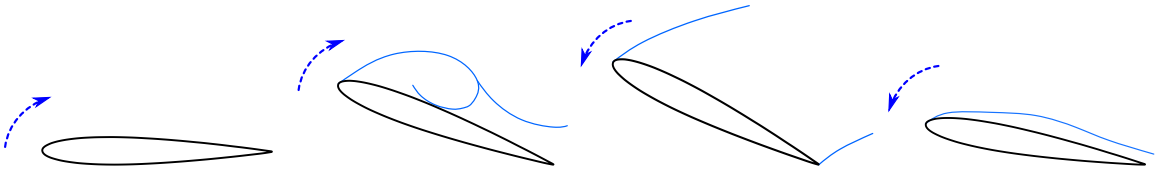

Figure 1.1: Dynamic stall stages: (1) attached flow at lower angles of attack (upstroke), (2) dynamic stall vortex creation and convection above the airfoil (upstroke), (3) complete stall when the DSV sheds into the wake (downstroke) and (4) flow reattachment (downstroke)

progression of dynamic stall. Specifically, a recent study [Lee and Gerontakos, 2004] conducted at a moderate Re of 1.35×10^5 will be utilized for validation in this thesis. The dynamic stall maneuver observed in the experimental study by Lee and Gerontakos [2004] has been numerically simulated by various researchers [Wang et al., 2010, 2012, Gharali and Johnson, 2013, Singh and Páscoa, 2019]. Interestingly, none of these numerical studies were able to replicate the experimental results accurately. One the main goals of this study is to demonstrate that accurate numerical simulation of dynamic stall must be conducted in three dimensions with a focus on capturing turbulent scales. Despite the fact that the studied body is an infinite-span, two-dimensional airfoil, the flow physics are inherently three-dimensional; hence, dynamic stall is fundamentally a 3D phenomenon.

The resulting numerical framework will act as our high-fidelity simulation for the dynamic stall phenomenon. As it is evident from current results presented in the thesis and available literature, the dynamic stall phenomenon is a phenomenon that is rich in vortex dynamics and vortices interaction. Since most of the available models in unsteady aerodynamics rely on the point vortex model, a model that is kinematic in nature and does not allow true dynamical representation of dynamical system, we proposed our variational model that will overcome most of these drawbacks. The variational model that is based on the Principle of Least action acts as a first-order extension of current point vortex model that allow for true dynamical representation of the system (i.e., allow for generic initial condition and take into account different conservative or non-conservative forces).

Vortex dynamics represents one of the main pillars of fluid mechanics. The theoretical edifice has been growing since the seminal papers of the founder Helmholtz [1858, 1867]. He introduced the vorticity equations, and established the circulation conservation laws when the fluid motion

emerges from a potential force. The analogy between potential-flow and electricity, discovered by Maxwell [1869], has led to simple models of vortex dynamics [Lamb, 1924, Milne-Thomson, 1973]. For example, the standard law that is ubiquitously used in the literature to describe the motion of two-dimensional vortices (infinite vortex filament) is the *Biot-Savart law* [Newton, 2013], which provides first-order ODEs in the positions of the vortices, in contrast to the second-order ODEs describing any typical dynamics problem. That is, the potential-flow formulation is a kinematic representation of the flow field; it lacks dynamical features [Gonzalez and Taha, 2022]. Therefore, it does not permit consideration of arbitrary forces and arbitrary initial velocities of the vortex system. A true fluid *dynamic* model would result in second-order ODEs in the position of the vortices.

Kirchhoff and Hensel [1883] studied N free-point vortices of constant strength in an unbounded domain, and described their motion based on the Biot-Savart law. Interestingly, the resulting ODEs possessed a Hamiltonian structure [Goldstein et al., 2002, Lanczos, 2020]. Based on this finding, they defined a Hamiltonian function (the Kirchhoff function) for constant-strength point vortices. Interestingly, this Hamiltonian was not derived from basic definitions or first principles. It is not defined in terms of the physical quantities (e.g., kinetic and potential energies) that typically constitute the Hamiltonian function for a mechanical system. It was constructed from the reciprocal property of the stream function of point vortices. Therefore, its use outside this case is questionable, and its extension to other scenarios may not be clear except for a few cases as described below. To account for the interaction with a body, Routh [1880] extended Kirchhoff's model using the method of images. Afterwards, Lin [1941,] provided the most generic and complete formulation of point vortices interacting with a body in two dimensions. He was able to show the existence of a hybrid function W composed of Kirchhoff's and Routh's, which described the Hamiltonian dynamics of a system of vortices and called it the *Kirchhoff-Routh* function. Arguably, the W function could be considered as the underlying foundation of every application and study that includes constant-strength point vortices [Cottet et al., 2000, Alekseenko et al., 2007, Aref, 2007]. It is interesting to mention that Lin [1941,] relied on the concept of *generalized Green's* function, which was extended

later by Crowdy [2020] to multiply-connected domains relying on prime functions (see Section 16 in Crowdy [2020] for the extended KR function in multiply-connected domains). Nevertheless, in all these representations [Kirchhoff and Hensel, 1883, Lin, 1941,], the resulting ODEs were first-order in the position variables.

In this dissertation, we rely on the principle of least action and its application to the dynamics of a continuum inviscid fluid by Seliger and Whitham [1968]. Exploiting this variational principle, we develop a variational formulation for the dynamics of massive vortices of constant strength that are modeled as circular patches (Rankine vortices) with a negligible core size. This effort is considered as a first-order extension of the common vortex dynamics models using the KR function and Bio-Savart law which takes into account the inertia inside the vortex core. In contrast to previous efforts, the defined Lagrangian and the dynamical analysis are derived from first principles. Interestingly, the new formulation results in a second-order ODE defining vortex accelerations, consequently allowing for richer dynamics if the initial velocity is different from the Biot-Savart induced velocity. Moreover, the resulting dynamics recover the KR ODEs in the limit of a vanishing core size. Also, since the model emerges from a formal dynamical analysis, it could take into account different body forces arising from a potential energy. Such a capability is demonstrated in this study by considering an electromagnetic force acting on charged vortices cores. The resulting interaction between the electrodynamic force and the hydrodynamic vortex force leads to a rich, nonlinear behavior that could not be captured by the standard KR formulation. Finally, this new variational formulation can easily be extended to arbitrary time-varying vortices with deforming boundaries and these extensions will be considered in future work.

Chapter 2

Dynamic Stall Phenomenon and Numerical Setup

2.1 Background

Benton and Visbal [2019] provides a concise yet comprehensive description of dynamic stall development. Initially, along the upstroke, a Laminar Separation Bubble (LSB) [McCroskey, 1981, 1982] forms near the airfoil's Leading Edge (LE). Concurrently, a flow reversal occurs at the Trailing Edge (TE), where a turbulent boundary layer begins to propagate upstream. The interaction between the LSB and the turbulent boundary layer then leads to the formation of the Dynamic Stall Vortex (DSV) through a complex process. Detailed descriptions of the DSV creation based on experimental studies are provided by Mulleners and Raffel [2013, 2012]. Specifically, when the reversed flow reaches the LSB, it bursts, forming a Leading Edge Vortex (LEV) [Pruski and Bowersox, 2013]. At the same time, the rear separated turbulent flow evolves into a Turbulent Separated Vortex (TSV) above the airfoil. Subsequently, the LEV and TSV merge to form the DSV, which then convects over the airfoil's upper surface. This dynamic is presented in recent

numerical studies by Visbal and Garmann [2018] and Visbal [2014], where Wall-Resolved Large Eddy Simulation (WRLES) [Larsson et al., 2016] is employed as a high-fidelity numerical tool to capture this complex dynamic. They concluded that high-fidelity simulation tools are essential to accurately predict complex separations and turbulent boundary layer interactions, as lower-order models (e.g., averaging techniques) might not capture critical physical aspects.

In this study, various turbulence models and numerical simulation techniques are employed to highlight the three-dimensional nature of the dynamic stall phenomenon. The models include the Reynolds-Averaged Navier-Stokes (RANS) and its unsteady version URANS, as well as the Detached Eddy Simulation (DES) and its enhanced versions, Delayed Detached Eddy Simulation (DDES) and Improved Delayed Detached Eddy Simulation (IDDES). The RANS and URANS methods primarily rely on turbulence closure models [Pope, 2000, Wilcox et al., 1998], which can lead to questionable results when simulating flows with significant separations, such as dynamic stall. Their main limitation is that they average turbulent scales rather than resolving them. For instance, these solvers cannot accurately predict the static lift curve of an airfoil beyond the stall angle [Spalart, 1997, Petrilli et al., 2013, Goc et al., 2021]. An alternative approach, although more computationally expensive, that can resolve the large (and usually most significant) scales of turbulence is the Large Eddy Simulation (LES) [Sagaut, 2006]. In the LES method, large turbulent scales are resolved through a spatial filter, while smaller scales filtered out are modeled using an ad-hoc model called Sub-Grid Scales (SGS). Interestingly, even with SGS modeling, LES remains the second most computationally demanding technique after Direct Numerical Simulations (DNS). The high computational demand for external flows is primarily due to the requirements within the boundary layer viscous sub-layer [Schlichting et al., 1960], where the no-slip boundary condition is satisfied, and significant shear stress occurs. Conversely, for free shear layers and mixing layers, the LES technique is quite feasible. To mitigate the high computational demands of LES near the wall, Detached Eddy Simulation (DES) [Spalart, 1997, Shur et al., 1999, Spalart, 2000, Travin et al., 2000, Strelets, 2001] was introduced as a hybrid RANS/LES solver.

The core concept behind DES is to combine the strengths of RANS and LES techniques by applying RANS near the wall, where turbulent scales are much smaller than the grid spacing, and LES in free shear layers away from the body, where the resolved turbulent scales match the local mesh size. Since LES solutions are not sensitive to SGS modeling away from the wall (i.e., in free shear layers), the RANS turbulence model can effectively serve as the SGS model for LES. This innovative approach enabled the development of this hybrid solver [Shur et al., 1999, Spalart, 1997, Bunge et al., 2007]. The solver's dual role is managed by a switch that depends on grid spacing relative to the RANS length scale, L_t. For instance, the RANS length scale for the k-ω turbulence model is defined as $L_t = \frac{k_t^{1.5}}{\epsilon}$, where k_t represents the turbulent kinetic energy and ϵ is its dissipation rate. Essentially, if the local mesh is fine enough for LES, it will be activated; otherwise, RANS will be employed. This formulation, the first version of DES, is known as DES97, as conceived by Spalart [1997].

In DES simulations, RANS is tasked with modeling the entire boundary layer, which includes the viscous sub-layer, log-layer, and outer layer [Tennekes and Lumley, 2018]. However, this version of DES has a significant drawback: the limiter (switch) is applied uniformly across the domain. This can be problematic in regions where the mesh size is very fine within an attached boundary layer. In such cases, LES may be activated, supplanting the RANS solver, even though the mesh is not fine enough for a feasible LES simulation. This results in a reduced eddy viscosity within the boundary layer, leading to fictitious separation, termed Grid-Induced Separation (GIS) by Menter and Kuntz [2004]. To address this issue, DES97 was upgraded by Spalart et al. [2006] to Delayed-DES (DDES). An additional shielding function was introduced to prevent the LES from encroaching on the RANS boundary layer region. DDES follows the same DES principle in resolving the flow: RANS models all the boundary sub-layers, while LES handles the free shear layer regions (i.e., outer flows). Despite the shielding function, DDES still faces a drawback in the boundary layer region. The results from DDES do not conform to the universal log-layer law within the boundary layer, particularly for highly separated flows and turbulent boundary layers—a phenomenon known as "*log-layer mismatch*" in the literature.

A new approach was introduced by Spalart, Shur, and colleagues [Shur et al., 2008, Travin et al., 2006, Nikitin et al., 2000] to address the mismatch issue by allowing the LES solution to more accurately penetrate turbulent boundary layer regions. In this method, rather than relying entirely on RANS within the boundary layer, the Wall-Modeled LES (WMLES) is used to resolve the outer and log layers, which constitute around 80% of the boundary layer, while the viscous sub-layer is still modeled by RANS. Additionally, the interface between the RANS and WMLES solvers is no longer dictated by the limiter value and grid size (i.e., user-defined). Instead, it depends on the grid and/or the solution itself, making it impossible to be directly specified by the user. This formulation is known as Improved-DDES [Shur et al., 2008, Travin et al., 2006, Nikitin et al., 2000]. For more details about WMLES and its implementation, readers are referred to Larsson et al. [2016], and for information on different variants of DES solvers, to Spalart [2009], Mockett [2009]. In terms of RANS modeling, all the previously mentioned solvers can utilize the Spalart and Allmaras [1992] (S-A) closure model directly or the k-ω SST model [Menter, 1994, Wilcox, 2008], which has been adapted for DES integration by Travin et al. [2002] and Gritskevich et al. [2012]. In the current study, the k-ω SST is preferred over the S-A model because it can handle severe pressure gradients in the boundary layer and is a complete two-equation turbulence model [Pope, 2000, Wilcox et al., 1998].

Computational simulations of dynamic stall have been conducted in numerous studies, and providing a comprehensive discussion of these efforts is beyond the scope of this work. However, discussing some relevant efforts may be prudent. Martinat et al. [2008] utilized URANS and DDES with various turbulence models to replicate McAlister et al. [1978] experimental study results. The simulations were conducted for both 2D and 3D domains. Results from both simulations did not perfectly match the experimental lift coefficient data from McAlister et al. [1978]. Nevertheless, the DDES simulations showed better agreement with the experimental data than URANS; and the 3D simulations performed even better overall. Wang et al. [2010] conducted 2D URANS simulations of Lee and Gerontakos [2004] experimental dynamic stall maneuver, comparing different turbulence closure models. The numerical results agreed with the experimental lift coefficient

values during the upstroke but failed to match the downstroke values. In a subsequent study, Wang et al. [2012] performed URANS simulations with more advanced turbulence closure models, along with DDES simulations; both sets of simulations were conducted for 2D and 3D domains. The results predicted the maximum lift coefficient using 2D URANS simulation but did not correctly capture the downstroke loads. Their 3D simulations were based on the findings of Martinat et al. [2008], but interestingly, the lift values obtained from the 3D simulation diverged from the experimental measurements even more than the 2D ones. Similar 2D DDES simulations were performed by Wang et al. [2012] and Singh and Páscoa [2019]. The latter [Singh and Páscoa, 2019] conducted DES and URANS simulations over a 2D mesh for the dynamic stall maneuver of Lee and Gerontakos [2004]. As expected, they were able to predict the upstroke accurately but failed to capture the maximum lift coefficient. Additionally, the resulting values during the downstroke did not match the experimental measurements. However, their work provided more information about the flow field; they compared the wake velocities at a unit chord downstream of the airfoil with experimental measurements. This comparison showed that, unlike all URANS simulations, the DDES results nearly matched the experimental wake measurements. Finally, Gharali and Johnson [2013] conducted 2D URANS simulations on a meticulously crafted grid. They efficiently predicted the lift curve slope, achieving good matching with the lift peak value and the downstroke lift, within the limitations of RANS. This finding underscores the importance of mesh considerations in simulations of complex flow fields, even when using less demanding methods like URANS, let alone the DES family of simulations. Consequently, a meticulous approach to mesh generation is adopted in the current study, particularly for the LES part, as will be shown later.

The simulations mentioned above highlight the critical importance of 3D simulations in accurately capturing the complex flow physics of dynamic stall. One of the primary aims of this thesis is to test the hypothesis regarding the three-dimensional nature of dynamic stall and emphasize the significant role of the Turbulent Separated Vortex (TSV) and its interaction with the Leading Edge Vortex (LEV) during the dynamic stall process. This investigation employs various simulation techniques, including URANS, DDES, and IDDES, comparing their results with the experimental data of Lee

and Gerontakos [2004]. The numerical setup and settings of each solver, along with validation for the simulations, are discussed in section 2.2. The dynamic stall simulation results for each technique are then presented in section 3.1. Subsequently, a detailed discussion of the dynamic stall stages and the capability of each solver to capture its dynamics is provided in section 3.2, followed by a discussion and conclusion.

2.2 Numerical Setup

Simulations were conducted for the NACA 0012 airfoil pitching around the quarter-chord point at a Reynolds number of $Re = 1.35 \times 10^5$ and a reduced frequency of $k = \omega c/2u_\infty = 0.1$ (where c is the chord length, u_∞ is the free stream velocity, and ω is the motion frequency), matching the dynamic stall maneuver of the experiment by Lee and Gerontakos [2004]. The pitching motion is defined as:

$$\alpha(t) = \alpha_m + \alpha_o \sin(\omega t), \tag{2.1}$$

where α_m is the mean angle of attack set at 10°, α_o is the pitching amplitude set at 15°, and ω is selected corresponding to $k = 0.1$. The numerical simulations and grid generation were performed using Ansys Fluent 19.2 and ICEM CFD 19.2 software, respectively, while the motion was implemented by a User Defined Function (UDF) in Fluent. All the simulations were carried out on the "HPC" cluster computer available at the University of California, Irvine. The grid generation and case setup will adopt most of the information available in the previous study by the authors [Khalifa et al., 2021].

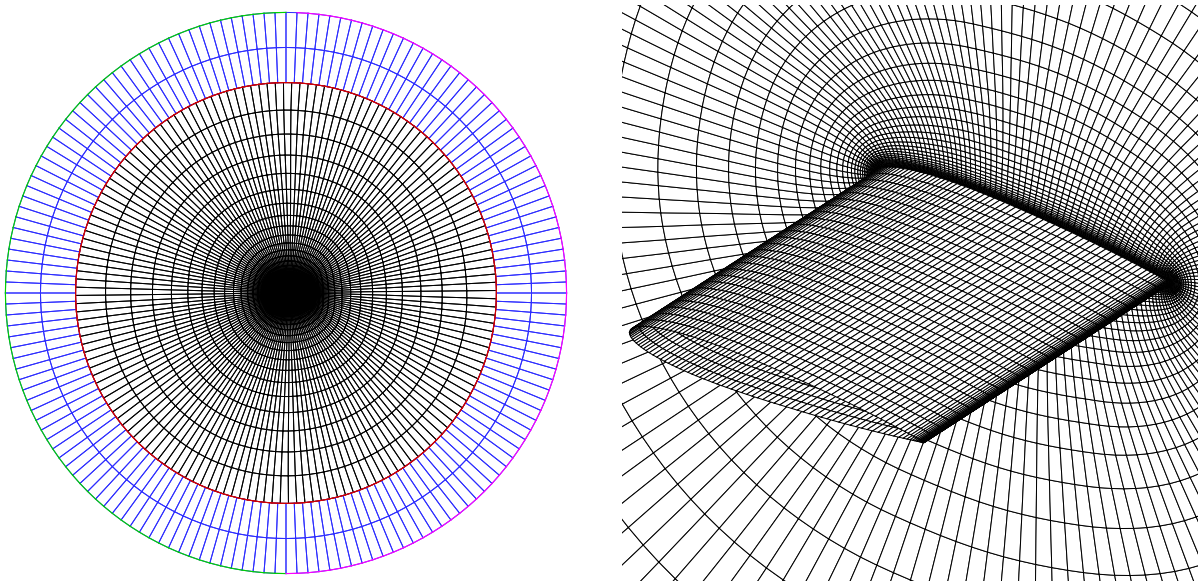

(a) (b)

Figure 2.1: Different mesh representations: (a) 2D section showing different zones: rotating one in black, static outer shell in blue, interface surface in red, inlet in green and outlet in magenta; (b) 3D view showing element distribution.

2.2.1 Grid

Initially, a 2D mesh was generated and then extruded to create a 3D mesh. This resulting mesh was utilized for both URANS and DES simulations. The surface mesh was meticulously crafted to ensure high quality suitable for 3D DES simulations. Although DES simulations have stringent requirements, the RANS solver can operate with most grid types without such stringent demands. Moreover, RANS can accommodate various grid types with different discretization schemes, unlike the LES solver. Therefore, the mesh was designed with DES simulations in mind, ensuring that it would also be suitable for RANS. The mesh was divided into two distinct zones, as illustrated in fig. 2.1a: a static outer shell zone with inlet and outlet surfaces, and a rigid rotating zone encompassing the airfoil, with an interface between these two zones. This division of the mesh domain was adopted to facilitate the airfoil rotation. The interface was positioned far from the airfoil to ensure it would not interfere with the LES portion of the solution.

The mesh size in an LES simulation is critical because it serves as the spatial filter of the solution,

thus defining the resolved spectrum of turbulence scales. It can be considered analogous to the sampling frequency in any temporal transformation. However, the spatial filter introduces complexities: instead of being implemented in a single dimension like the temporal case with Δt, it is a multi-dimensional transformation performed simultaneously in three dimensions ($\Delta X, \Delta Y, \Delta Z$). Therefore, the grid size must be chosen carefully, considering the interplay between these dimensions. If the grid size (i.e., spatial sampling) is very fine in one direction compared to the other two, it may be ineffective for the LES solver. Moreover, unlike temporal filtration (or discretization), finer meshes do not always result in better simulations [Travin et al., 2000], indicating that one cannot perform a grid refinement study for LES to achieve a "*grid independent solution*" as typically done with RANS solvers [Travin et al., 2000]. This also applies to the time step in LES simulations. Consequently, a grid independence study was only conducted for RANS simulations in this study.

Another crucial aspect in mesh generation is the resolution of wake mixing layers—a region where flow separates from the body, generating multiple turbulent scales due to mixing. This phenomenon is broadly defined by Menter [2012] as the Separating Shear Layer (SSL), which must be resolved by the LES solver. Recall that, due to the hybrid nature of DES, RANS is activated inside highly viscous boundary layer regions, while LES is activated inside the free shear layer. The mixing scales in the SSL require a finer mesh in this region for LES to be effectively activated and to resolve them correctly. Otherwise, the DES limiter defined by the grid spacing will allow the RANS solver to handle this part of the wake, which will dampen most of the vortical structures in this region. Therefore, proper LES resolution necessitates extra mesh refinement in the region where the SSL occurs (i.e., near the TE). However, this extra refinement near the TE is closely tied to the previous discussion of selecting mesh sizes in different directions. For instance, if a very fine planar mesh is used but with large spanwise spacing, then this extra refinement will be ineffective, and the DES limiter will still activate the RANS solver based on the coarser mesh size. Conversely, if the mesh is refined equally in all directions, then the LES could be activated near a boundary layer region, inducing GIS if the local mesh size is inadequate for proper LES boundary layer resolution. This

discussion highlights the importance of selecting appropriate mesh sizes for different regions in the simulation and the benefit of the DDES shielding function in protecting the RANS boundary layer solution from unnecessary intervention by the LES solver.

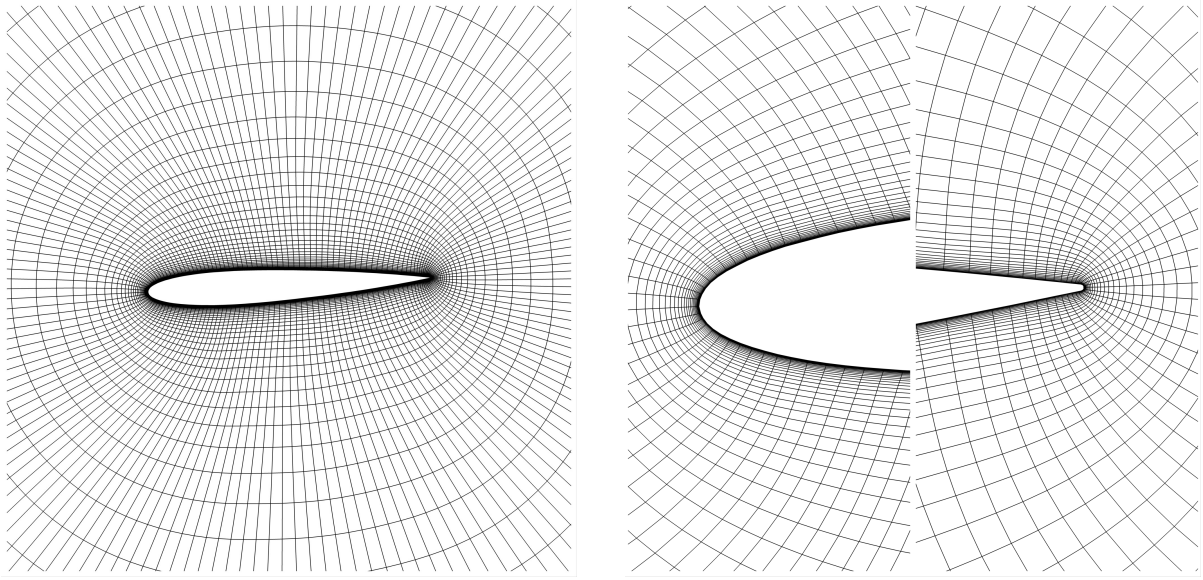

(a) (b)

Figure 2.2: Different mesh domains: (a) Growth rate and spacing near airfoil wall; (b) Treatments of leading and trailing edges.

Regarding the mesh type, Kozelkov et al. [2016] demonstrated that unstructured meshes used for DES simulations require more elements to achieve the same solution quality as a structured mesh. Their study showed that unstructured-polyhedral meshes needed two to three times more elements than a block-structured-hexahedral mesh, and this factor could be as high as six for tetrahedral meshes. While unstructured meshes are suitable for DES and DDES, they are less ideal for IDDES because WMLES implementation on an unstructured grid is not yet practical [Travin et al., 2006]. Consequently, a multi-block-structured mesh was employed for the current study. The mesh topology is an O-grid over a rounded trailing edge (TE) airfoil; the TE is rounded to facilitate the use of the O-topology. The 2D planar mesh comprised quadrilateral elements, and the 3D mesh was generated from hexahedral elements, as shown in fig. 2.1. The number of elements and their distribution across the domain were chosen following the guidelines of Spalart and Streett [2001] and the DES NACA 0012 grid implemented by Shur et al. [1999]. The distribution of elements

considers different regions in the mesh, such as viscous, focus, and departure regions [Spalart and Streett, 2001].

The primary requirement for the RANS solver using the k-ω turbulence model is the height of the first cell at the wall for boundary layer treatment. This height was determined using Schlichting's skin friction formula [Schlichting et al., 1960] to ensure a non-dimensional wall-distance y^+ less than or equal to unity. Additionally, the first cell height was further reduced by one-fourth to account for the dynamic motion of the airfoil, resulting in a final value of $h = 1.1 \times 10^{-4}c$. The boundary layer treatment consists of 30 layers with a slower expansion rate than typically required for standard RANS simulations, as recommended by Shur et al. [1999]. This slower expansion rate allows the boundary layer mesh to extend further into regions where severe viscous stresses are absent (i.e., outside the boundary layer). Moreover, the increased number of layers and the slow expansion rate will be beneficial for the WMLES in the IDDES simulations. The small expansion ratio is crucial for LES solvers, which are highly sensitive to abrupt changes in cell length. Another important aspect of the meshing process was the special attention given to the TE region to address the SSL issue previously discussed.

The spanwise width was selected following the recommendation of Shur et al. [1999]. They indicated that a width of $1c$ is adequate to capture the flow field characteristics for a streamlined body at high, but moderate, angles of attack. Additionally, they referenced the study by Najjar and Vanka [1995], which used a spanwise width domain of $2\pi c$ to predict the drag over a normal flat plate, considered a bluff body. Although Najjar and Vanka [1995] noted that the 2π span was significantly larger than the distance between consecutive streamwise ribs, this width was chosen to ensure the dynamics in the spanwise direction were accurately captured. Travin et al. [2000] utilized a $1D$ spanwise width in their pioneering DDES simulation over a cylinder, reporting no significant differences between cases using πD, $2D$, or larger spans. In a recent study on the onset of dynamic stall by Benton and Visbal [2019], the spanwise width was set to $0.05c$, aligning with Menter [2012]'s recommendation, provided periodic boundary conditions are used. This boundary

condition is crucial for simulating an infinite airfoil within a computational domain. The spanwise width is sufficient as long as periodic boundary conditions are applied and the domain extends to cover two consecutive streamwise ribs, as demonstrated in fig. 3.1b with our $1c$ selection. The spanwise spacing was determined based on the non-dimensional wall distance z^+ in the z-direction, with 25 equally spaced elements over the one chord length. All these considerations were implemented in a mesh with a $20c$ radius ($15c$ for the rotating part and $5c$ for the outer shell), containing 160 elements over the airfoil and 62 normal to its surface, resulting in a total of 2.48×10^5 elements with the origin located at the quarter chord, as shown in fig. 2.2.

2.2.2 Solver Settings

The pressure-based solver was employed for all simulations as the flow is incompressible, and all simulations were conducted as transient in time. URANS, DDES, and IDDES simulations shared the same case setup unless otherwise stated. Incompressible air was selected as the material for all mesh zones, and a UDF was developed to define the motion of the inner-rigid-rotating zone, while the outer shell zone remained static. The boundary condition for the airfoil surface was set as a no-slip wall. The inlet semi-circle surface was specified as a velocity inlet with turbulence intensity and length scale set to 5% and 10%c, respectively. The inlet intensity was chosen based on the assumption of fully turbulent flow [Pope, 2000]. The outlet surface was designated as an outflow rather than a constant pressure boundary. This selection was made because an outflow boundary allows vortices to cross the boundary, whereas a constant pressure boundary would damp the vortical structures along with their associated pressure gradients as they convect through the boundary. The boundary conditions for the two bounding side walls were set to translational periodic. This choice enabled the resolution of turbulent structures when they interact with the boundaries [Menter, 2012]; other boundary conditions such as symmetry (i.e., slip-wall) might impose nonphysical constraints on the resolved turbulent scales. Additionally, the selection of periodic conditions allows for flux convection through the boundary, which is essential for simulating an infinite spanwise domain.

The coupled scheme was utilized for pressure-velocity coupling, and the under-relaxation factors were set to unity. The Least Squares Cell method was chosen for spatial gradient discretization. The pressure and turbulence discretization schemes were selected as standard and second-order upwind, respectively. The case setup then addressed the most critical discretization, particularly for the LES solver, which is the momentum scheme. The second-order upwind scheme was selected for URANS simulations. However, this type of scheme is too dissipative when used with LES solvers. Therefore, differencing schemes are preferred for the LES solver, though they come with some limitations. The regular central differencing scheme can introduce nonphysical wiggles in the flow, so the bounded central differencing scheme for momentum discretization [Menter, 2012] was used instead.

Regarding temporal discretization, the bounded second-order implicit dual-time stepping integration was used with 10 iterations for the inner loop. The optimal time step in DES simulations aims for a Courant–Friedrichs–Lewy (CFL) number of approximately unity $\approx 1 = u\Delta t/\Delta x$ in the LES region [Menter, 2012]. For URANS, an appropriate time step criterion ensures a balance: the time step must be large enough to properly average turbulent structures and small enough for accurate discretization of the motion time constant. The maximum velocity u_{max} in the LES region is estimated to vary from 1.2 to $1.5 \times u_\infty$ [Spalart and Streett, 2001]. Therefore, to meet the CFL criterion, the time step must be smaller than $\Delta t = \Delta_{max}/u_{max}$, where Δ_{max} is the grid size in the LES portion (i.e., focus region) corresponding to the spanwise mesh spacing ΔZ. Consequently, the time step was set to $\Delta t = 0.015\ s$ for all simulations, resulting in 1062 time steps per one pitching cycle. Finally, for the case setup, the URANS simulations were initialized using hybrid initialization, while the DDES and IDDES were initialized with a previously converged URANS solution.

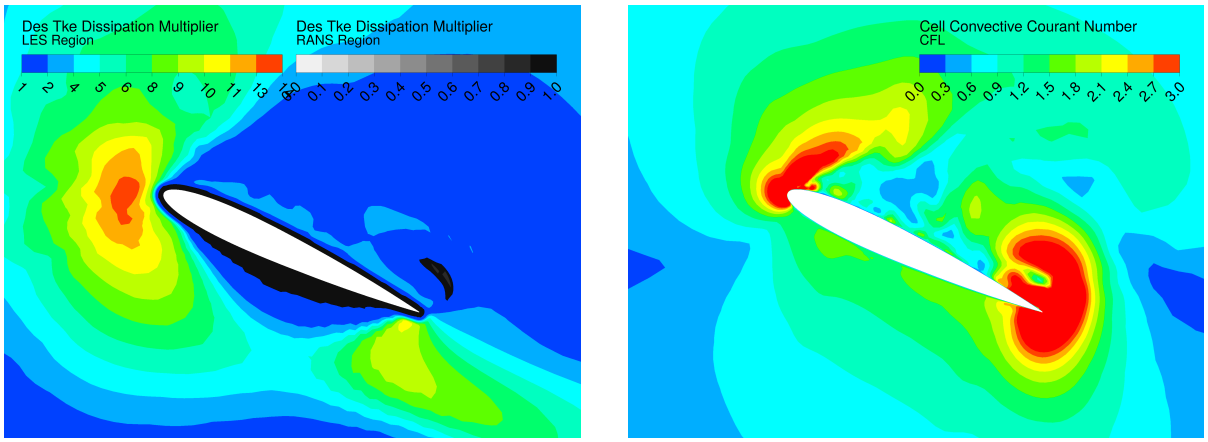

(a) (b)

Figure 2.3: Mid-plane contour plots for the IDDES simulation at $t = T/4$: (a) DES Tke Multiplier contour values, where RANS and LES domains are distinguished by color; (b) various CFL contours.

2.2.3 Solution Assessment

To ensure convergence, residuals were monitored and checked for stable behavior, but they were not used as the primary convergence criterion. Instead, the lift coefficient time history was examined to determine convergence. For instance, while simulating a static airfoil, convergence was assumed when the C_L reached a constant value. Conversely, for oscillating airfoils, convergence was considered achieved when the lift coefficient reached a periodic solution after 15 complete cycles for the URANS simulations and 25 cycles for DES. Another criterion, specifically for proper turbulence modeling, is the non-dimensional wall distance y^+ values. In both URANS and DES simulations, the y^+ values were ensured to be less than unity. The inlet and outlet mass flux difference was checked to be less than 10^{-8} for adequate continuity convergence. As mentioned earlier, the CFL values should be around unity for LES simulations. Thus, the LES portion in the solution was first identified, and then the CFL values were checked within it. To differentiate the LES from the RANS region, one can rely on the "*DES Turbulent Kinetic Energy Dissipation Multiplier*" value; if it is less than unity, it indicates a RANS region and LES otherwise, as shown in fig. 2.3a. Accordingly, the CFL values were found to be in the acceptable range for the LES region, as shown in fig. 2.3b.

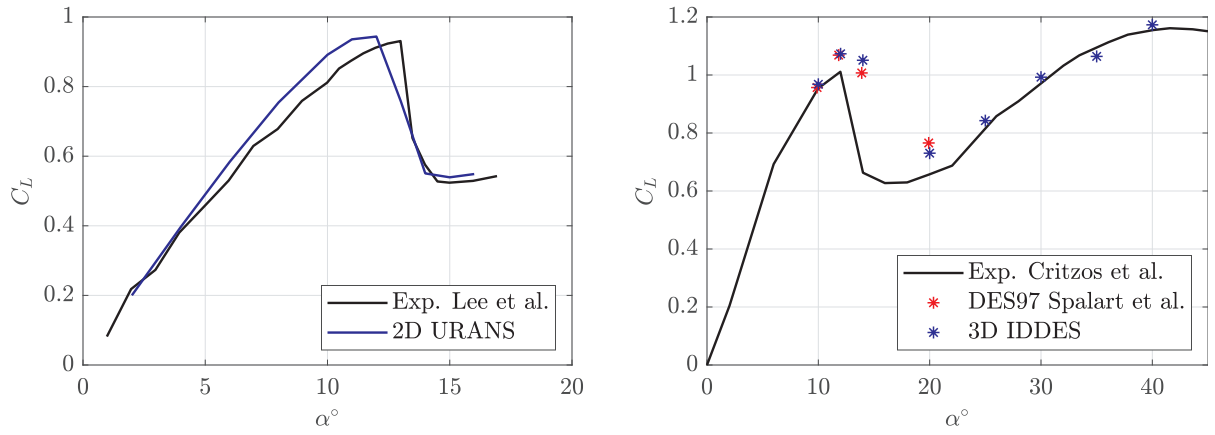

(a) (b)

Figure 2.4: Different plots used for validation: (a) 2D URANS static airfoil results validated against experimental data; (b) 3D IDDES simulation lift coefficient values at selected angles of attack versus experimental data [Critzos et al., 1955] and DES97 [Shur et al., 1999] results.

2.3 Validation

A crucial task in the validation process for URANS simulations is achieving a grid-independent solution, a feature not applicable to IDDES and DDES simulations, as previously mentioned. Two-dimensional URANS simulations were conducted for a static airfoil at 10° and 30° angles of attack. The grid independence study included two-step mesh refinements, with details listed in table 2.1. The relative error in the lift coefficient was computed between each refinement step, and the study showed relative error values of less than 1%. Furthermore, for both simulations, the numerical C_L values matched the experimental data. Therefore, the first coarser mesh was selected for the rest of the simulations. Another series of 2D URANS simulations were performed to construct the 2D static C_L-α curve. The resulting curve was validated against the experimental data of Lee and Gerontakos [2004]. It is evident from fig. 2.4a that the 2D URANS lift coefficient values are in fair agreement with the experimental data. On the other hand, for DES simulations, since the concept of a grid-independent solution is not always viable, validation was conducted only against experimental data. Moreover, the grid and time step sizes were ensured to follow the guidelines presented by Cummings et al. [2008] and implemented for a DDES simulation by Qin et al. [2015].

A series of 3D IDDES simulations for a static airfoil beyond the stall angle (where the lift coefficient does not depend on the Reynolds number) were performed. Results were compared in fig. 2.4b with experimental data from Critzos et al. [1955] and DES97 numerical simulations from Shur et al. [1999], showing excellent agreement.

Table 2.1: Information of grid study and lift coefficient values.

Grid		**Coarse**	**Medium**	**Fine**
No. of Nodes		9600	38080	151680
C_L	10°	0.89	0.9	0.9
	30°	1.205	1.236	1.241

Chapter 3

Simulation Results and Dynamic Stall Development

3.1 Simulation Results

This section presents the results obtained from the performed simulations using different solvers. First, an overview of the capabilities of URANS and hybrid solvers is discussed, highlighting the limitations and strengths in resolving the features of the flow field. Second, the resulting lift coefficient values from URANS and DES (i.e., DDES and IDDES) simulations are compared against each other. The comparison focuses on each solver's ability to capture various stages of dynamic stall. As anticipated, the comparison reveals the superior performance of 3D models over 2D ones.

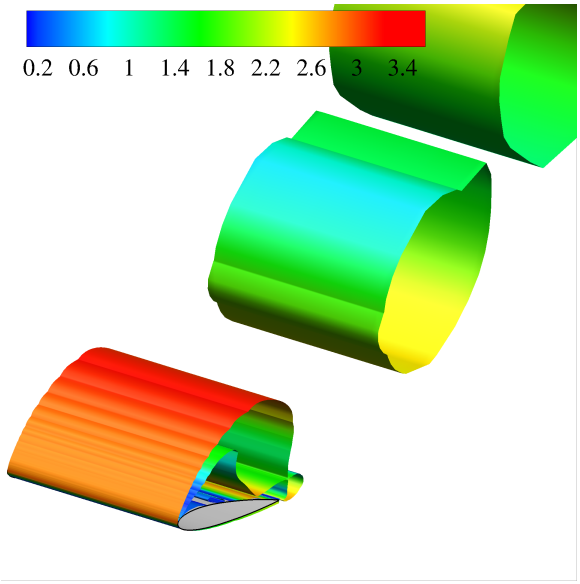

(a) (Multimedia available online)

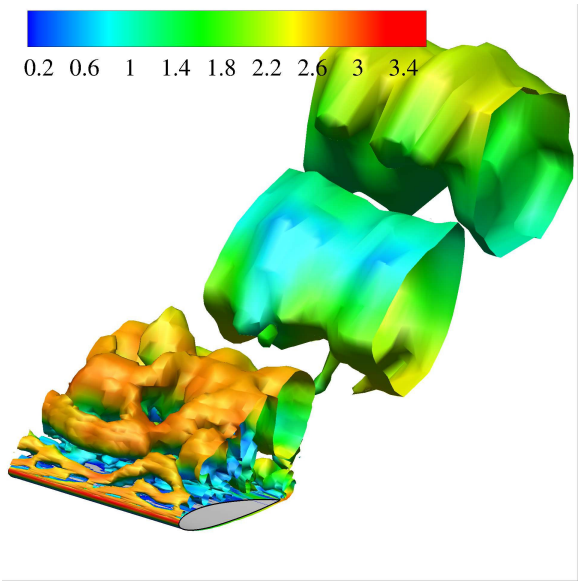

(b) (Multimedia available online)

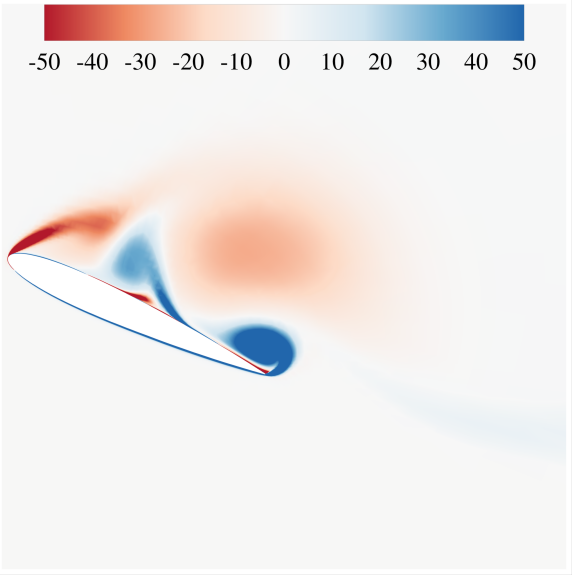

(c)

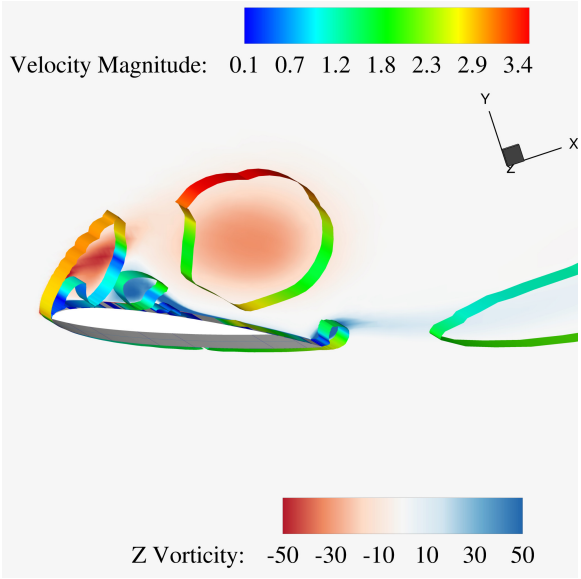

(d)

Figure 3.1: Different CFD visualizations used for comparison: (a) 3D URANS Q-criterion iso-surfaces at $Q = 0.5s^{-2}$ flooded with velocity magnitude at $t/T = 1/3$; (b) 3D IDDES Q-criterion iso-surfaces at $Q = 0.5s^{-2}$ flooded with velocity magnitude at $t/T = 1/3$; (c) 2D URANS vorticity contours at $t/T = 0.21$; (d) 3D URANS mid-plane z vorticity and Q-criterion iso-surface at $Q = 0.5s^{-2}$ flooded with velocity magnitude at $t/T = 0.21$.

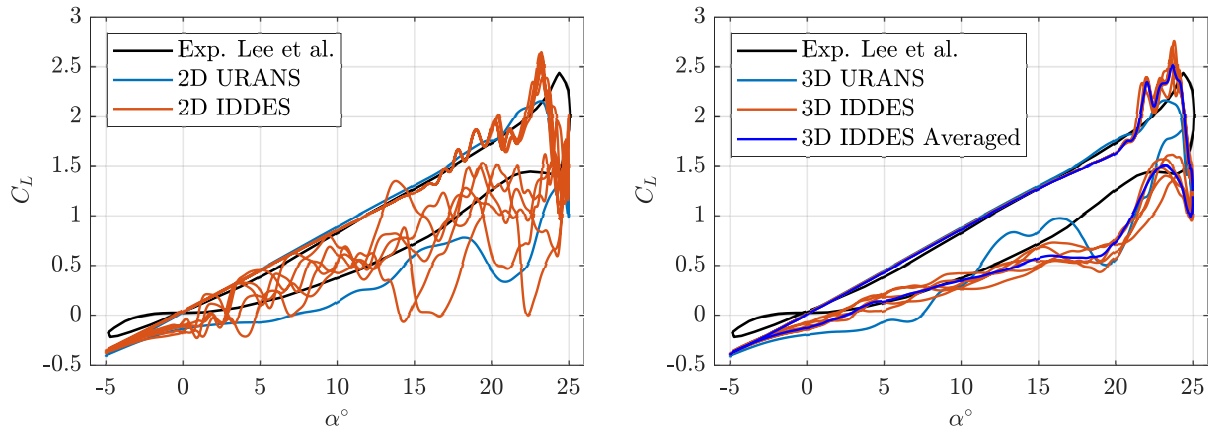

(a) (b)

Figure 3.2: The lift coefficient values for the last five cycles of different solvers compared with experimental data (a) 2D URANS and IDDES; (b) 3D URANS, IDDES and the ensemble average for the IDDES lift coefficient.

3.1.1 Evaluation of Solvers Results

A qualitative evaluation of each solver can be achieved by examining various flow visualizations, as illustrated in fig. 3.1. Q-criterion iso-surfaces [Hunt et al., 1988], which represent the boundaries of vortices, generated from 3D IDDES and URANS simulations at the same time instant are shown in figs. 3.1a and 3.1b (Multimedia available online), respectively. These iso-surfaces are colored by velocity magnitude to depict the underlying flow field. It is evident that the IDDES simulation produces a more complex three-dimensional vortical structure compared to the URANS solution. Indeed, the Q-criterion iso-surfaces for the 3D URANS resemble the 2D URANS planar z-vorticity boundary extended in the spanwise direction, as seen in figs. 3.1c and 3.1d. A closer examination of fig. 3.1a reveals the presence of LE separation, which rolls up to form a LEV; this LE separation is fundamental for predicting the DSV within the URANS framework. Additionally, there is no indication of turbulent separation on any scale over the airfoil's upper surface, limiting the URANS solver's ability to predict the merging of these turbulent eddies into the TSV. Consequently, the interaction between the LEV and TSV is absent in the URANS solver. Conversely, the IDDES simulations exhibit significant turbulent separation over the airfoil's upper surface, as shown in fig. 3.1b. As will be further discussed, these resolved scales and their interactions are crucial for

accurately predicting the lift coefficient throughout the dynamic stall cycle, particularly the lift peak value and its timing.

The time histories of the lift coefficient over the last five simulated cycles from 2D, 3D URANS, and IDDES are shown in fig. 3.2. The results from 2D and 3D URANS are perfectly repeatable to the extent that each cycle plot is indistinguishable from the other. This consistent behavior indicates the inability of URANS to capture chaotic turbulent scales, effectively damping rich turbulence dynamics through averaging. Conversely, the 2D IDDES results are not repeatable or coherent when compared with URANS, as depicted in fig. 3.2a. This comparison demonstrates that 2D IDDES simulations are unreliable in predicting consistent lift coefficient values, leading to erroneous behavior of the lift coefficient. Specifically, the downstroke values exhibit significant fluctuations and deviations from the experimental results. However, there is a reasonable match with the experimental data during the upstroke, as the flow remains attached to the airfoil, where the 2D DES family of solvers can provide reliable results [Shur et al., 1999]. Therefore, the 2D IDDES simulations will be excluded from further discussions. In contrast to 2D IDDES, the lift curve from 2D URANS, presented in fig. 3.2a, shows reasonable agreement with experimental data during the downstroke and perfect matching during the upstroke until 22°, at which point the 2D URANS fails to predict the lift coefficient accurately.

The comparison of 3D simulation results is illustrated in fig. 3.2b. The 3D URANS lift coefficient closely follows the experimental data during the upstroke, except at the peak value, a shortcoming inherited from its 2D counterpart. On the downstroke, 3D URANS significantly improves over the 2D results, matching most of the experimental behavior, particularly after the initial reattachment at around 18° $\downarrow$. However, 3D URANS diverges from the experimental data at the start of the downstroke, showing a noticeable kink in the lift coefficient near 22° angle of attack, as depicted in fig. 3.2b. Conversely, 3D IDDES exhibits a better agreement with the experimental data compared to other methods. While not perfectly repeatable like 3D URANS due to the chaotic turbulence structures resolved by the LES solver, the variations between the five cycles remain within a narrow

range from the ensemble-averaged value, indicating closely correlated cycles. The 3D IDDES results accurately capture the lift coefficient peak value and align well with the experimental data for most of the upstroke. Additionally, they capture the initial kink in the lift coefficient during the downstroke but later deviate from the experimental data, before realigning near the cycle's end. Notably, DDES simulations for this dynamic stall maneuver were also conducted but are not discussed here as their characteristics mirror those of IDDES. These observations underscore that dynamic stall is a highly separated, inherently three-dimensional flow phenomenon that necessitates a high-fidelity, scale-resolving simulation tool for accurate modeling and analysis.

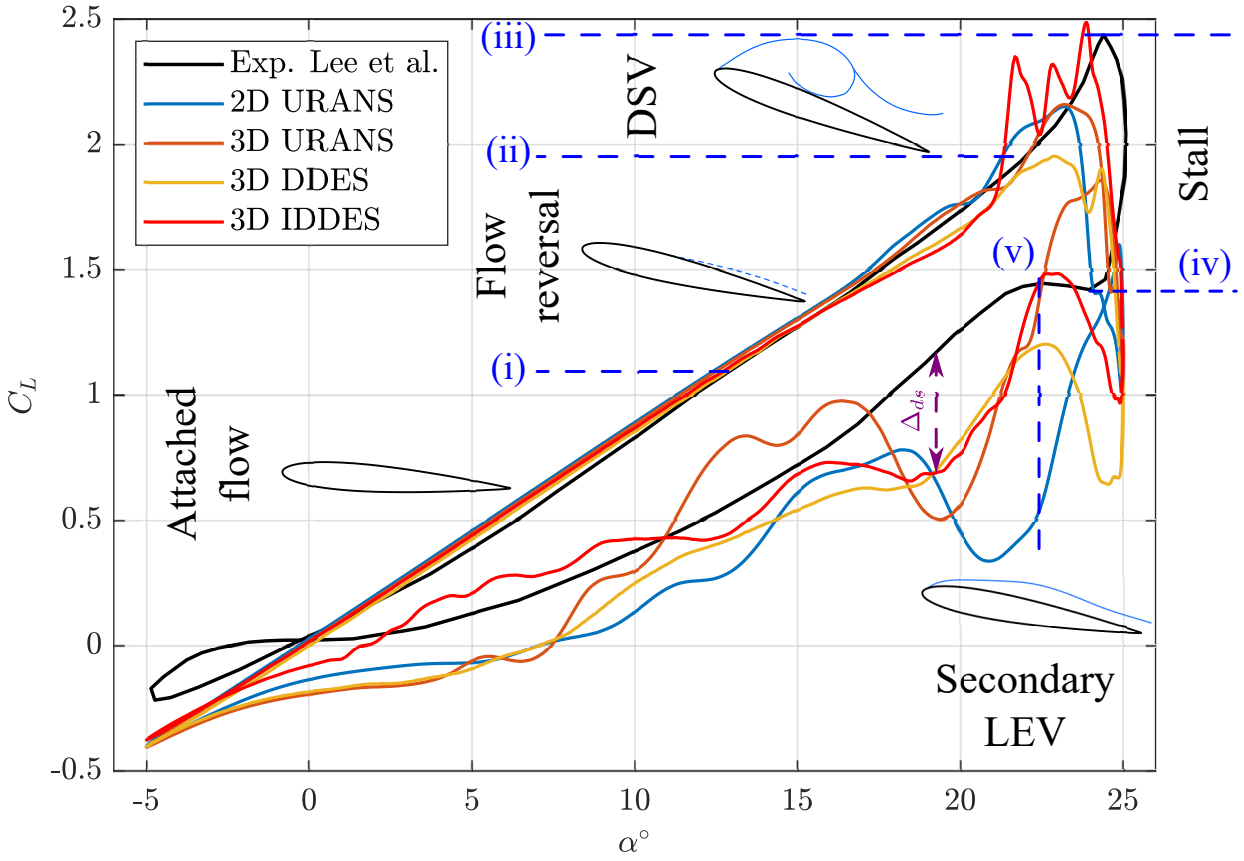

Figure 3.3: A comparison between different solvers lift coefficient values and experimental data.

3.1.2 Comparison of the Lift Dynamics

This section provides a thorough examination of the lift dynamics produced by each solver, comparing them to the experimental data from Lee and Gerontakos [2004] and the flow physics detailed in recent studies [Visbal, 2014, Visbal and Garmann, 2018, Benton and Visbal, 2019]. The focus will be on evaluating how well each solver captures the various stages of the dynamic stall phenomenon. To facilitate this evaluation, we will begin by illustrating the different stages of a dynamic stall cycle based on the experimental findings of Lee and Gerontakos [2004].

At the beginning of a typical dynamic stall cycle, the airfoil pitches up at relatively small angles of attack, resulting in attached flow and a fairly constant lift curve slope, as illustrated in fig. 3.3. Following instant (i), the airfoil continues to pitch up, experiencing a trailing edge (TE) flow reversal on the suction surface. This flow reversal forms an unsteady turbulent boundary layer that moves upstream as the angle of attack increases. Concurrently, a laminar separation bubble (LSB) forms at the leading edge (LE), and a turbulent separated layer develops near the TE. Additionally, a shear layer emanates from the LE, supplying vorticity to both the LSB and the TE turbulent separated layer. Up to this point (ii), there are no severe flow separations, and the lift curve slope C_{L_α} remains approximately equal to the static lift curve slope of the airfoil. As the flow reversal stage concludes, the backward flow moving towards the LE collides with the LSB, causing it to burst and form a leading edge vortex (LEV). Meanwhile, near the TE, the turbulent separated layer has expanded to cover most of the airfoil's upper surface, generating small eddies. These eddies merge into a more coherent structure known as the turbulent separated vortex (TSV). The LEV continues to grow, fed by the LE shear layer, until it becomes strong enough to attract the TSV. Together, they roll up to create the dynamic stall vortex (DSV), which convects over the airfoil's upper surface before shedding away. During the DSV formation and convection stage (ii)-(iii), the lift coefficient reaches its peak value, and its slope increases significantly.

Immediately after the DSV sheds, leading to a sudden decrease in lift, the stall stage (iii)-(iv) begins,

during which the airfoil operates in a highly separated flow and experiences a dramatic drop in lift. Following this stage, the downstroke commences, making the airfoil behave as if it were stationary in a massively separated flow. The LE separated shear layer remains active, and turbulent eddies persist over the airfoil. This dynamic situation facilitates the formation of another vortex. Notably, a smaller LEV, referred to as the "Secondary LEV" by Lee and Gerontakos [2004], emerges at instant (v) in fig. 3.3. It is crucial to note that the Secondary LEV does not always appear in every dynamic stall maneuver. A specific combination of Reynolds number, reduced frequency, and airfoil kinematics is necessary for this phenomenon to occur. For instance, at higher reduced frequencies, there might not be enough time for the Secondary LEV to form. Additionally, the occurrence of the DSV vortex and its shedding depends on the pitch rate, as discussed in the study by Fouda et al. [2022]. After the Secondary LEV stage, the airfoil continues to pitch down, and the flow gradually reattaches, marking the end of the cycle.

The C_L dynamics obtained from each solver are compared against the experimental data in the context of the previously discussed stages of a dynamic stall cycle. To facilitate this comparison, one cycle from each simulation is selected. Figure 3.3 presents five plots: experimental data, 2D URANS, 3D URANS, 3D DDES, and 3D IDDES. Beginning with the URANS simulations, it is evident that both 2D and 3D simulations capture most of the upstroke dynamics up to $\alpha = 22°$, at which point complex dynamics begin to develop. Beyond this angle, both simulations fail to predict the peak lift value, indicating that the predicted DSV strength is inaccurate compared to the experimental case. Although the peak value is incorrect, both simulations manage to reproduce the sudden increase in the lift curve slope, as they both capture the DSV, albeit with incorrect strength. This inaccuracy directly translates to a deviation in the lift curve from the experimental data in the stall region. Furthermore, the 2D URANS fails to predict the Secondary LEV, as there is no indication of it in the lift results. In contrast, the 3D URANS captures the Secondary LEV, but both the timing and strength are incorrect, leading to an overestimation of the C_L values. During the remainder of the downstroke, the 2D URANS results do not match the experimental data, whereas the 3D URANS results show better agreement, reasonably matching the experimental data in the

17° − 12° region. The superior performance of the 3D simulations compared to the 2D ones, even within the inaccurate URANS framework, provides further evidence that dynamic stall is inherently a 3D phenomenon, particularly during the DSV creation and downstroke reattachment process.

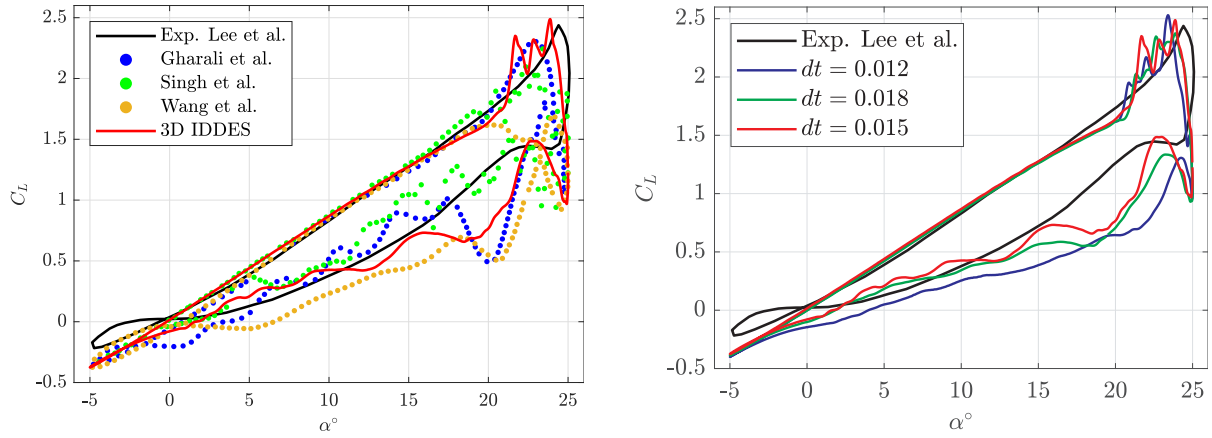

(a) (b)

Figure 3.4: (a) Current numerical IDDES simulation compared against the experimental data [Lee and Gerontakos, 2004] and previous numerical efforts by Gharali and Johnson [2013], Singh and Páscoa [2019] and Wang et al. [2012]; (b) Time step sensitivity results for the IDDES simulations.

It might be expected that DDES simulations would align more closely with experimental data than URANS, given that DDES is a hybrid RANS-LES solver. However, this expectation is not met. The DDES significantly underpredicted the DSV strength compared to both experimental data and URANS results, failing to accurately follow the lift curve during the stall phase. Although the timing of the Secondary LEV is correctly predicted, its estimated strength is inaccurate. Furthermore, the DDES results during the downstroke do not match the experimental data. This underperformance of the DDES solver in predicting the DSV strength and the Secondary LEV can be anticipated. Recall that DDES is essentially DES97 with an additional shielding function to protect the RANS solution; it lacks the WMLES, an inherently three-dimensional solver, necessary to resolve the mixing and buffer layers of turbulent boundary layers. This formulation is the primary reason for its inferior performance: the turbulent structures modeled by the RANS solver and communicated to the LES are insufficient for the LES to generate the TSV because they lack the rich information captured by WMLES, which effectively resolves most of the turbulent boundary layer. Consequently, the LES

solver fails to resolve the three-dimensional rich vortical structures, leading to an underprediction of the DSV strength and the Secondary LEV. This finding further supports the argument that dynamic stall is inherently a three-dimensional phenomenon.

The results from the IDDES simulations stand out as the most accurate among the methods tested. Unlike the other solvers, IDDES successfully predicted both the timing and strength of the DSV and the Secondary LEV, closely matching the experimental lift coefficient at the peak point and during the Secondary LEV. Additionally, the lift curve slope during the DSV stage (ii)-(iii) aligns almost perfectly with the experimental data, despite minor fluctuations in the C_L values. These fluctuations naturally arise from the resolved vortical structures forming on the airfoil's upper surface due to turbulent separation. The exceptional performance of the IDDES is attributed to the WMLES's ability to capture the outer and log layers of the turbulent boundary layer over the airfoil. These turbulent structures merge into the TSV and interact with the LEV to form the DSV. They are also crucial in forming the Secondary LEV, interacting with the LE separated shear layer and evolving into the Secondary LEV. Furthermore, the IDDES demonstrated the best agreement with experimental results throughout the cycle, except for two points: following the Secondary LEV, where the difference is noted as Δ_{ds}, and during the stall. The discrepancies at these points might be due to a coarse mesh in the LES wake region, which encounters the convected vortices and prevents the LES solver from maintaining the DSV and Secondary LEV for longer periods. The superior performance of the IDDES in capturing most features of a dynamic stall cycle reinforces the argument that dynamic stall is inherently a three-dimensional phenomenon. This suggests that accurate predictions require not only three-dimensional simulations but also a solver capable of capturing the complex, three-dimensional turbulent features of the flow.

The nearly perfect C_L values obtained from the IDDES simulations are compared with previously published numerical simulations, and are shown in fig. 3.4a. This comparison underscores the accuracy of the current simulations relative to past efforts and highlights the meticulous approach employed in this study for DES simulations, as detailed in section 2.2. The lift coefficient values

at the peak and during the Secondary LEV instants match the values from the benchmark study by Lee and Gerontakos [2004]. Additionally, the overall lift coefficient time histories closely align with the benchmark study for 85% of the cycle, with discrepancies occurring in the downstroke from the Secondary LEV instant to 15°. Furthermore, a sensitivity study on the time step and its impact on IDDES is presented in fig. 3.4b. This study was conducted using two different time steps, $\Delta t = 0.012\ s$ and $0.018\ s$, differing from the value used throughout the simulations in this thesis ($\Delta t = 0.015\ s$). Interestingly, the resulting lift changes slightly due to variations in the strength and timing of the Secondary LEV. Moreover, the downstroke reattachment process is not identical across all cases, as indicated by the discrepancies in C_L values shown in fig. 3.4b. Despite alterations in the downstroke results, the maximum lift coefficient, which depends on the DSV strength, remains consistent across all simulations, matching the experimental data. This time sensitivity study demonstrates that IDDES simulations are highly sensitive to time step selection, indicating that a time-independent solution is not well-defined in hybrid solvers, similar to the grid dependency issue discussed earlier.

3.2 Dynamic Stall Development for Different Solvers

This section delves into a more detailed discussion of the DSV creation process. Each solver is evaluated based on its ability to accurately capture flow separation, vortex amalgamation, DSV strength, and convection dynamics. Unlike previous sections, where integral quantities such as the lift coefficient were used, this analysis focuses on field quantities. The study utilizes mid-plane z-vorticity contours and flow streamtraces at key instants of the dynamic stall phenomenon. Additionally, the instantaneous lift coefficient values and corresponding pressure coefficients are presented for each vorticity frame (i.e., time snapshot).

First, chronologically ordered frames of mid-plane z-vorticity contours with flow streamtraces are displayed in fig. 3.5, with each column representing a different solver. Negative values indicate

clockwise vorticity, and all figures use the same contour levels. Second, the pressure coefficient corresponding to these frames is shown in fig. 3.6. To enable comparison across different snapshots, the pressure coefficient is adjusted to have a common zero value at the stagnation point (i.e., the point of maximum C_p in the plot). Finally, fig. 3.7 presents a comparison of the lift coefficient time history against experimental data, with markers indicating each instant shown in fig. 3.5. The selected snapshots from each solver highlight key instants corresponding to major flow field features (e.g., vortex creation, roll-up, and shedding) that influence the suction pressure distribution and thus the instantaneous lift coefficient. Due to the differing dynamics captured by each solver, these instants are not synchronized and occur at slightly different times. Additionally, the DDES and IDDES results exhibit variability due to the chaotic nature of resolved turbulent scales, leading to non-synchronized snapshot timings. This setup provides a foundation for further discussion.

3.2.1 URANS

The URANS solver can predict some features of the dynamic stall phenomenon, but it lacks the accuracy and detailed depiction of vigorous turbulence mixing seen in the vorticity frames. Instead, it presents a smooth, averaged, and diffused vorticity distribution of the actual turbulent flow field. The first stage of dynamic stall involves the creation of a laminar separation bubble (LSB), evident in fig. 3.5a, where the separation bubble is marked by rotating streamtraces. Concurrently, flow reversal begins at the trailing edge (TE) and propagates upstream across the airfoil suction surface. This stage determines the amount of vorticity fed by the leading edge (LE) shear layer into the LSB and the TE separated flow. When the reversed flow reaches the LSB, it triggers the LSB's eruption into a leading edge vortex (LEV), as shown in fig. 3.5d. Simultaneously, at the TE, the separated flow rolls up into a vortex structure called the trailing edge separated vortex (TESV). At this moment, the LE separated shear layer is only feeding the LEV and has no role in the dynamics of the TESV. The strength of the TESV depends on the amount of vorticity fed into the trailing separated flow during the first stage. The presented feeding dynamics emphasize the importance

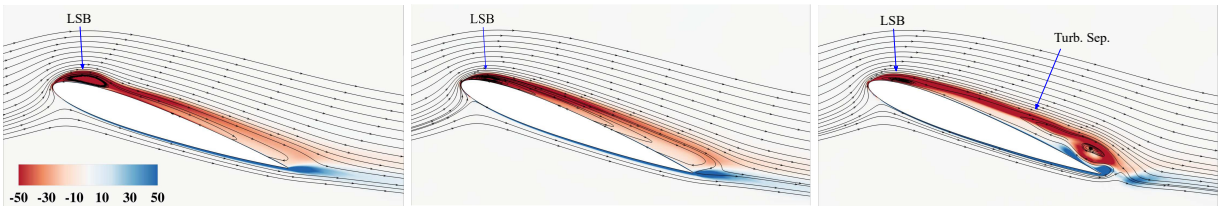

(a) URANS α = 19.18 ↑

(b) DDES α = 20.89 ↑

(c) IDDES α = 21.07 ↑

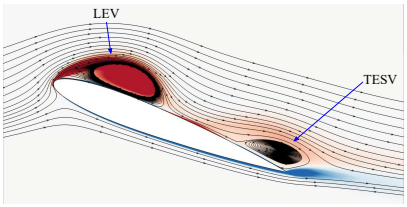

(d) URANS α = 21.01 ↑

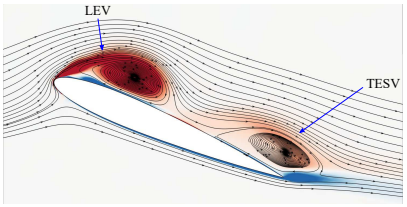

(e) DDES α = 22.82 ↑

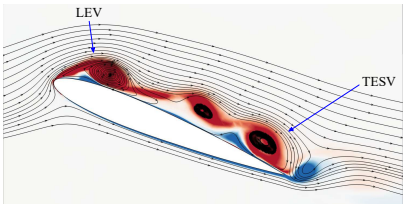

(f) IDDES α = 21.97 ↑

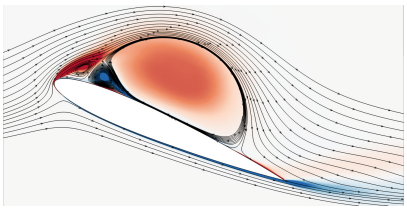

(g) URANS α = 23.09 ↑

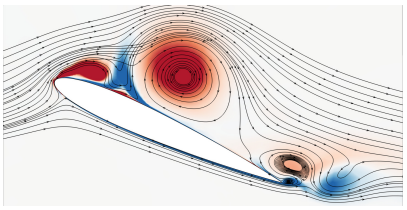

(h) DDES α = 23.93 ↑

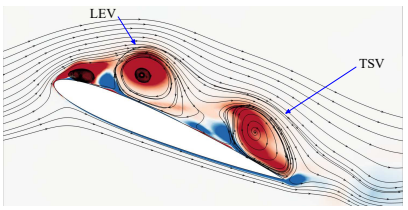

(i) IDDES α = 22.77 ↑

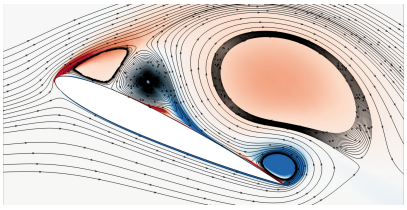

(j) URANS α = 24.69 ↑

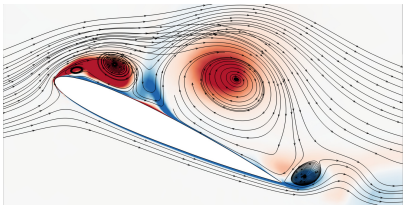

(k) DDES α = 24.29 ↑

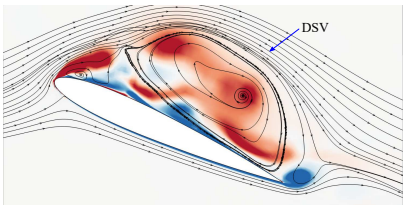

(l) IDDES α = 24.02 ↑

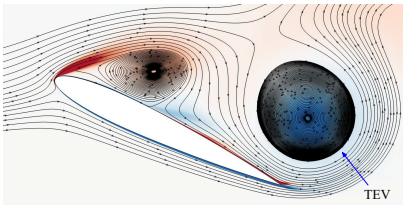

(m) URANS α = 24.97 ↑

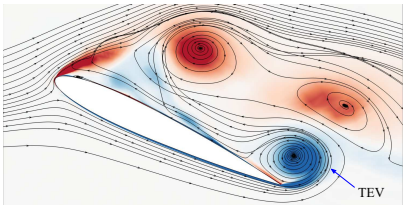

(n) DDES α = 24.96 ↑

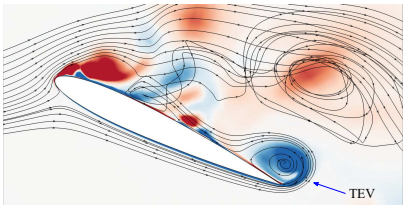

(o) IDDES α = 24.92 ↑

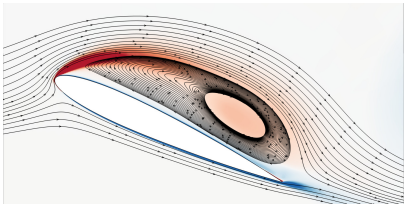

(p) URANS α = 24.35 ↓

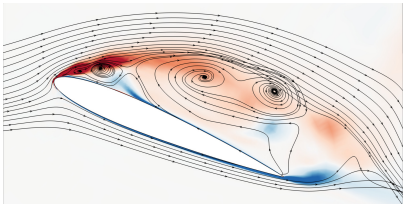

(q) DDES α = 23.94 ↓

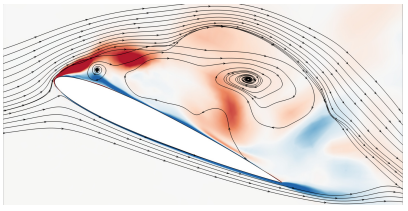

(r) IDDES α = 24.21 ↓

Figure 3.5: Mid-plane z-vorticity contours along with streamtraces for all solvers presented in a chronological order. The left column is URANS; the middle is DDES and the right column is IDDES.

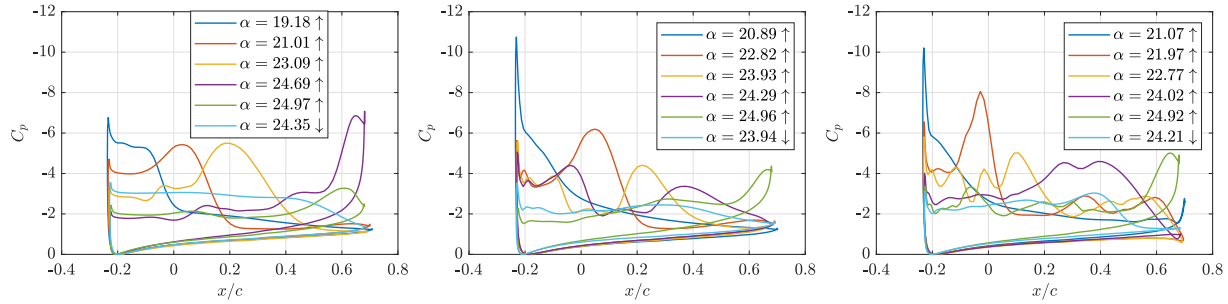

(a) URANS (b) DDES (c) IDDES

Figure 3.6: Mid-plane pressure coefficient for presented frames in fig. 3.5.

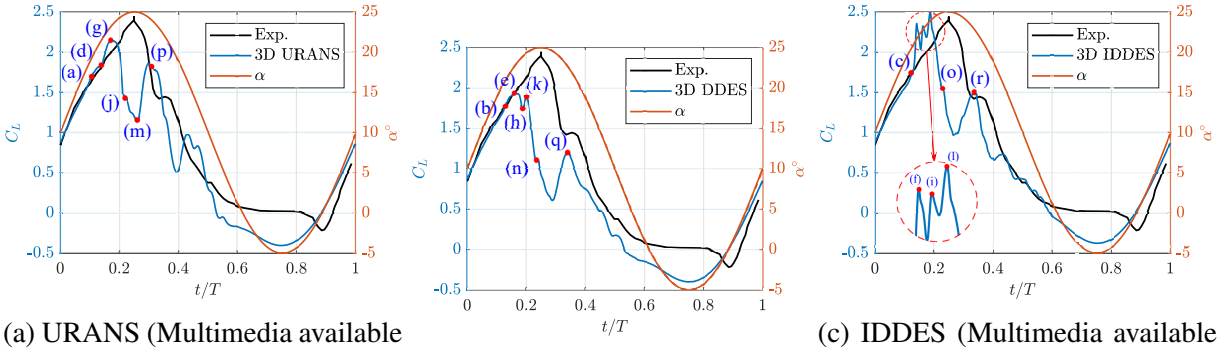

(a) URANS (Multimedia available online) (b) DDES (c) IDDES (Multimedia available online)

Figure 3.7: Lift coefficient time history versus the experimental one along with the instantaneous angle of attack; each snapshot in fig. 3.5 is indicated by a lettered marker.

of this stage, as the strength of the TESV and the LEV are dictated here. Additionally, the LEV and the TESV do not appear to interact with each other. The pressure coefficient of these frames can be found in fig. 3.6a, where clear evidence of the LSB and LEV suction pressure is present. Interestingly, despite the presence of the TESV, it is not strong enough to induce powerful suction near the trailing edge, as shown in fig. 3.6a. The lift coefficient for the frames figs. 3.5a and 3.5d is shown in fig. 3.7a (Multimedia available online), with the second frame indicating a sudden increase in the lift coefficient slope, signaling the creation of the LEV.

As time progresses, the LEV continues to grow, sustained by the LE shear layer, as depicted in fig. 3.5g. The LEV moves downstream while remaining attached to the airfoil's suction surface. In contrast, the TESV does not stay on the upper surface and instead sheds into the wake, reducing its influence on subsequent dynamic stall events. Consequently, the LEV becomes the primary

factor affecting the suction pressure coefficient during this phase, as shown in fig. 3.6a, leading to the maximum lift coefficient observed in the cycle, presented in fig. 3.7a. However, the magnitude and timing of this maximum lift value do not align with experimental findings. The simulated maximum lift coefficient is lower than the experimental value and occurs significantly earlier. Another significant factor in the flow dynamics during this phase is the positive-vorticity shear layer originating from the airfoil's lower surface at the TE. This shear layer forms a strong vortex attached to the airfoil's upper surface, referred to as the Trailing Edge Vortex (TEV), as shown in fig. 3.5j. This counter-clockwise vortex formation, combined with the shedding of the LEV from the upper surface, accounts for the sudden drop in lift depicted in fig. 3.7a. Additionally, the impact of the LEV on the pressure coefficient curve in fig. 3.6a is not apparent at this stage, but a strong suction peak near the TE indicates the presence of the TEV.

The subsequent stage, illustrated in fig. 3.5m, represents the point of maximum angle of attack during the cycle. At this moment, the LEV has fully detached from the frame, and the enlarged TEV is separated from the airfoil surface downstream. This stage coincides with the minimum lift coefficient during the upstroke, and the associated pressure coefficient curve displays minimal suction across the airfoil, as shown in fig. 3.6a. Concurrently, a nascent vortex structure near the LE starts receiving vorticity from the LE shear layer; this vortex will evolve into the Secondary LEV in the following frame. After the TEV sheds into the wake and moves downstream, the Secondary LEV becomes the dominant feature, as seen in fig. 3.5p. The predicted Secondary LEV exhibits a deformed, squeezed shape spanning the airfoil's upper surface with a concentrated vorticity core near the TE. This squeezed vortex shape results in a semi-uniform increase in suction pressure over the airfoil, with slightly higher values near the TE, indicating the core's presence, as shown in fig. 3.6a. However, similar to the main LEV, the URANS solver fails to accurately predict the exact timing of the Secondary LEV and the corresponding lift coefficient.

3.2.2 DDES

The DDES solver is anticipated to capture more detailed mixing scales compared to URANS, as evidenced in fig. 3.5. Unlike the smooth, diffused vorticity contours observed in the URANS frames, DDES reveals more resolved patches of vorticity. Similar to the behavior of URANS, the initial stage of the cycle involves the formation of an LSB and the upstream crawl of the reversed flow near the TE, as shown in fig. 3.5b. Concurrently, both the LSB and the TE separated flow receive vorticity from the LE shear layer. This complex process continues until the reversed flow collides with the LSB, causing it to erupt into a LEV, as illustrated in fig. 3.5e. At this point, similar to URANS predictions, the LEV remains attached to the airfoil's upper surface, while the TE separated layer rolls up into a TESV structure. The pressure coefficient at these consecutive snapshots is depicted in fig. 3.6b, and the corresponding lift coefficients are presented in fig. 3.7b. The effects of the LSB and the LEV are represented as two distinct suction peaks in the pressure coefficient plots. Notably, the lift coefficient reaches its maximum value for the cycle once the LEV is formed, without a significant increase in the lift coefficient slope.

In the subsequent stage, as the airfoil continues to pitch, fig. 3.5h depicts the LEV detaching from the upper surface and moving with the flow field. The LEV's size is smaller than predicted by URANS, resulting in a concentrated peak suction over the airfoil's upper surface, as shown in fig. 3.6b, in contrast to the broader suction distribution predicted by URANS in fig. 3.6a. Additionally, at this moment, there is another peak in the suction curve near the LE, indicating the formation of a smaller auxiliary LEV. These resolved vortex structures were absent in the URANS flow field, suggesting that the DDES solver can capture more scales than URANS. This resolution should have resulted in a better match of the DDES lift coefficient with the experimental data compared to the URANS results. However, the opposite is observed, as the DDES lift coefficient experiences a sudden drop, as shown in fig. 3.7b. At the same snapshot, the TESV is convected downstream without significantly impacting the dynamic stall process. The next frame, fig. 3.5k, shows the LEV moving downstream while the auxiliary LEV grows. This growth induces a significant peak

in the suction pressure coefficient near the LE, while the primary LEV's effect on suction pressure diminishes due to its downstream convection. Consequently, the lift coefficient slightly increases compared to the previous frame values, a result attributed to the auxiliary LEV's growth, although with inaccurate magnitude and peak timing compared to the experimental data. Additionally, this frame shows the initiation of the TEV, which will play a prominent role in the subsequent phase.

As the cycle approaches its end, fig. 3.5n shows that both LEVs have shed and detached from the airfoil's upper surface without interacting. Meanwhile, the previously mentioned TEV has increased in size and strength. These two factors contribute to the suppression of the suction pressure coefficient, resulting in a sudden loss in the lift coefficient. As time progresses, the continuously emanating shear layer from the LE rolls up to form the Secondary LEV, as shown in fig. 3.5q. Notably, the DDES solver accurately predicts the timing of this vortex, though it underestimates its strength. Additionally, the pressure coefficient distribution reveals a distinct peak indicating the presence and location of the Secondary LEV. In conclusion, the DDES solver demonstrates an ability to capture more scales and resolve detailed spatial flow features compared to URANS. However, it fails to predict the precise timing and magnitude of unsteady forces. This behavior may be attributed to the boundary layer dynamics still being resolved by URANS and subsequently fed to the LES solver in the DDES simulation.

3.2.3 IDDES

The IDDES simulation provides the richest flow field among the three solvers. Detailed vorticity structures and vigorous turbulent mixing with various scales are evident in all frames, which contribute significantly to the dynamic stall process. Following a similar chronological description as before, the creation of a LSB and the onset of flow reversal near the TE mark the first stage in dynamic stall, as illustrated in fig. 3.5c. While the IDDES results exhibit LSB structures similar to those of the other solvers, it uniquely predicts a turbulent TE separated shear layer, rather

than a diffused one. This TE separated shear layer is referred to as turbulent separation. The existence of this turbulent separation is primarily due to the WMLES capturing and resolving the turbulent boundary layer, with the adverse pressure causing the turbulent boundary layer to move forward. Moreover, the flow reversal is clearly present, distributing a significant amount of positive vorticity over the airfoil suction surface, which detaches the LE shear layer along with the turbulent separation. Consequently, a larger amount of negative vorticity convects downstream more easily, enhancing the nutrition process of the turbulent separation. Additionally, the turbulent separation near the TE possesses a vortex-like structure, which initiates the TESV, as will be seen in subsequent frames. These extra resolved features are primarily due to WMLES resolving turbulent scales across the boundary layer, unlike URANS and DDES, which average them. The LSB effect on the pressure coefficient, along with the initiating vortex at the TE, is distinguished in fig. 3.6c by two peaks on the suction side. At this stage, the lift coefficient values match the experimental data excellently, as seen in fig. 3.7c (Multimedia available online).

Subsequently, fig. 3.5f illustrates the creation of a LEV when the reversed flow collides with the LSB. Concurrently, the TESV develops near the TE, and the LE shear layer solely feeds the LEV. Interestingly, another vortex emerges between the LEV and the TESV. This intermediate vortex is crucial because it stabilizes the TESV near the TE, preventing it from being washed away. These three vortex-like structures will eventually coalesce to form the TSV, aligning with the mechanism captured by Mulleners and Raffel [2013]. The impact of these three vortices is evident in fig. 3.6c, which shows three distinct peaks in suction pressure values, enhancing suction across the airfoil's upper surface and resulting in a spike in the lift coefficient, as shown in fig. 3.7c. Unlike previous solvers, the TESV is not immediately washed away upon formation. Instead, it merges with the middle vortex (situated between the LEV and TESV) to form the TSV, as depicted in fig. 3.5i. Meanwhile, the LEV expands while convecting over the airfoil's upper surface, contributing to the TSV's stability by attracting it. Simultaneously, another small LEV forms, which will become part of the DSV in subsequent instants. At this point, most of the vorticity fed by the LE shear layer into the LEV or the turbulent separation is present over the airfoil's suction surface as the LEV and

the TSV. Without the intermediate vortex and the TESV, the TSV would not exist. The presence of the TSV alongside the LEV is clearly reflected in the pressure coefficient results, explaining the second spike in the lift coefficient. The next frame, fig. 3.5l, highlights the critical stage of the dynamic stall process: the merging of the LEV and the TSV to generate the DSV. This process is too complex to be fully captured in just two snapshots, so a detailed sequence is provided in fig. 3.8.

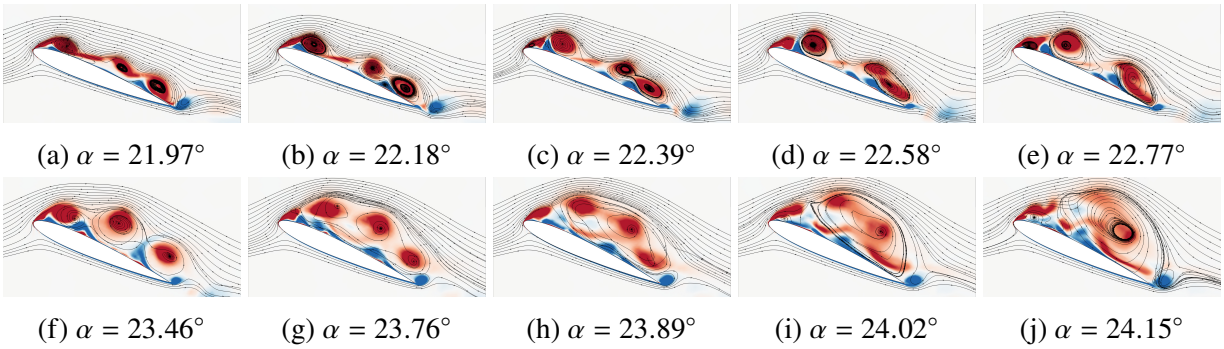

(a) $\alpha = 21.97°$ (b) $\alpha = 22.18°$ (c) $\alpha = 22.39°$ (d) $\alpha = 22.58°$ (e) $\alpha = 22.77°$

(f) $\alpha = 23.46°$ (g) $\alpha = 23.76°$ (h) $\alpha = 23.89°$ (i) $\alpha = 24.02°$ (j) $\alpha = 24.15°$

Figure 3.8: LEV and TSV merging process to form the DSV in IDDES simulation.

Figures 3.8a to 3.8e provide a detailed view of the dynamics involved in the formation of the TSV and the shedding of the LEV. Additionally, figs. 3.8f to 3.8j illustrate the merging process of various LE vortices with the TSV to create the DSV. In fig. 3.8f, we observe the complete formation of the TSV and the LEV, while the secondary auxiliary LEV grows as it is nourished by the LE shear layer. The subsequent frame, fig. 3.8g, depicts the maturation of the secondary LEV as it detaches from the airfoil's suction surface and begins its preliminary interaction with the TSV. This interaction occurs in two stages: initially, the primary LEV, being close enough, pulls the TSV beneath it, as shown in fig. 3.8h; subsequently, fig. 3.8i shows the amalgamation of the primary LEV and the TSV into a larger vortex—the DSV. Throughout these stages, the auxiliary LEV remains present and eventually interacts with the DSV. Once the DSV gains sufficient strength, it draws the secondary LEV towards itself, resulting in the formation of an even larger DSV, visible in fig. 3.8j. This progression underscores the significance of the earlier stages in determining the amount of vorticity that ultimately forms the DSV. The continuous merging of the TSV, middle vortex, and LEV is essential for maintaining the vorticity generated by the LE shear layer over the suction surface for an extended duration of the cycle. The interaction between the TSV, middle

vortex, and LEV is pivotal in determining the position and strength of the DSV at its inception before it convects downstream, which is crucial for accurately predicting the lift coefficient histories during unsteady motion. The size and strength of the DSV translate into widespread suction in the pressure coefficient values, with the highest suction compared to other solvers, as shown in fig. 3.6c. Consequently, the maximum lift coefficient over the cycle is achieved at this frame, as presented in fig. 3.7c. Notably, the IDDES simulation is the only solver that nearly perfectly predicts the lift coefficient history with an accurate maximum value over the cycle.

Examining fig. 3.5l where the DSV is formed, one can observe a positive vorticity eddy near the TE, which evolves into the TEV in the subsequent frame, fig. 3.5o. At this point, the DSV dissipates and is fully convected downstream of the airfoil. This shedding process results in a sudden decrease in lift, as shown in fig. 3.7c, accompanied by a significant reduction in the suction pressure coefficient over the airfoil. Figure 3.5r illustrates the final phase of dynamic stall, marked by the formation of the Secondary LEV. Notably, the IDDES solver accurately predicts both the timing and intensity of the Secondary LEV, resulting in a lift coefficient that closely aligns with the experimental data for this stage. Overall, the IDDES results show the best agreement with experimental data in terms of lift when compared to the other two solvers. Specifically, the maximum lift coefficient and its timing are precisely predicted. Additionally, the lift values associated with the Secondary LEV and much of the downstroke nearly coincide with the experimental data. Furthermore, the IDDES simulation presents the most detailed flow field features compared to the other solvers. It is note worthy to state that the current situation of having the numerical simulation matching the experimental results for the IDDES simulation is noticed in Patel and Zha [2020] for highly separated flows, a result that indicates the profound behavior of the IDDES solvers in capturing 3D complex flows.

3.3 Discussion

The previous discussion makes it evident that all three solvers share some common features of the dynamic stall phenomenon, such as the LSB, flow reversal, LEV creation and convection, presence of the TESV, and the Secondary LEV. However, the IDDES results are uniquely characterized by the presence of the TSV. This vortex is primarily captured due to the WMLES capability to resolve the turbulent boundary layer, which allows various small eddies to form the TSV. This particular vortex interacts with the LEV to create the DSV. In fact, the DSV formation process involves a series of cascading amalgamation events between the TSV and multiple LEVs, which is essential for accurate prediction of the DSV and, consequently, the aerodynamic loads. This feature was not captured by the DDES, where two consecutive LEVs are created and shed without interaction. These promising results from the IDDES indicate that additional flow features captured by inherently three-dimensional solvers, such as LES and WMLES for the turbulent boundary layer, are crucial for accurate prediction of dynamic stall and the associated lift dynamics.

The preceding discussion provided multiple pieces of evidence supporting the argument that dynamic stall is inherently a three-dimensional phenomenon. Firstly, it was evident that 3D simulations of dynamic stall maneuvers produce more accurate loads and flow features compared to 2D simulations, even within the relatively limited URANS framework. Secondly, the additional resolved scales by LES in the free shear layer region resulted in richer flow field features compared to the global averaging of turbulent scales—a characteristic possessed only by DDES and IDDES. Thirdly, the WMLES within the IDDES simulation, which is an inherently 3D modeling method, captured the complex turbulent dynamics present over the airfoil suction surface. This resulted in the most accurate flow features and aerodynamic loads compared to other simulations. In conclusion, dynamic stall should be studied using a three-dimensional formulation, considering the three-dimensional nature of the flow field, even if the problem geometry is purely two-dimensional.

Chapter 4

Variational Approach and the Principle of Least Action

4.1 Background

Perhaps it is worth mentioning the classical work of Gröbli [1877] on the three- and four-point vortices problem. Interestingly, using the kinematic formulation of the motion of point vortices enabled by the Biot-Savart law, resulting in first-order ODEs in position, he showed that the three-vortex problem is integrable. This problem was studied further by several authors such as Synge [1949], Rott [1989, 1990], Aref [1979, 1989]. Moreover, Gröbli [1877] was able to solve the integrable case of four vortices equal in magnitude and arranged as a cross-section of two coaxial vortex rings, in which he was able to predict the leapfrogging phenomenon. However, the four-vortex case is not always integrable and nonlinearities may complicate the dynamics, introducing chaotic behavior, as studied extensively by Aref [1984, 1983], Aref and Pomphrey [1980, 1982], Eckhardt and Aref [1988], Aref and Stremler [1999]. This discussion presents the importance of the three-vortex problem as a classical problem, especially since Newton [2013] showed that the

behavior of any N-vortices could be studied as a multiple of vortex triads, as shown in his detailed monograph describing most of the analytical studies of point vortices [Newton, 2013]. Despite the numerous contribution to the three- and four- point vortices problem described previously, the work of Gröbli still remains a classic contribution [Aref et al., 1992].

The kinematic formulation based on the Biot-Savart law has been extensively used in the literature for numerical simulation of vortex patches by discretizing them into many point vortices [Cottet et al., 2000, Alekseenko et al., 2007]. However, this approach has its drawbacks because the resulting kernel for integration is singular, which requires regularization. The *Vortex Blob* [Leonard, 1980] method was introduced to relax the highly singular nature of point vortices and define smoother velocity fields. The method relied on defining a vortex core shape with a vorticity distribution inside it. This method discretize the vorticity field into finite-sized "blobs" or particles, each carrying a fraction of the total vorticity. The vortex blob methods offer significant advantages in capturing the intricate details of unsteady, turbulent flows, particularly in regions where vorticity is highly concentrated. By tracking the motion and interaction of these blobs, the methods can efficiently resolve the dynamics of vortex interactions and turbulence with high accuracy and low numerical dissipation [Cottet et al., 2000]. Moreover, the vortex blob geometry could be held constant throughout the motion — an assumption that could introduce spatial errors. However, Leonard [1980] obtained an estimate of such an error while Hald and Del Prete [1978] and Hald [1979] showed that the resulting motion converges to Euler's solution. A notable benefit of vortex blob methods is their ability to handle complex boundary conditions and free or moving boundaries more flexibly than traditional grid-based methods. For example, they can model fluid-structure interactions where the boundaries are not fixed, such as the interaction between a vortex and a moving airfoil [Leonard, 1980]. Additionally, these methods are inherently adaptive, allowing for refined resolution in regions with high vorticity and coarser resolution elsewhere, thereby optimizing computational resources [Winckelmans and Leonard, 1993]. Vortex blob methods also exhibit reduced computational costs compared to conventional Eulerian grid-based methods because they do not require solving the flow field over an entire grid. Instead, the focus is on the regions of interest

where vortices are present, which leads to a more efficient use of computational power [Sethian et al., 1999]. This efficiency, coupled with their accuracy in simulating vortex-dominated flows, makes vortex blob methods a powerful tool in various applications, from aerodynamic simulations to environmental modeling of pollutant dispersion. The approach of *Contour Dynamics* was proposed as an alternative that does not suffer from singularity issues and spatial errors. It relies on the fact that vortex patches are solutions of Euler's equations. Hence, the boundary of the vortex patch is considered to be a material quantity. As a consequence, one needs only to track the velocity induced by the other vortices over this boundary and, hence, update the vortex position accordingly. The contour dynamics technique was first introduced by Zabusky et al. [1979], and multiple efforts were subsequently exerted by Saffman and Szeto [1980], Pullin [1992] and Saffman [1992].

The study of point vortices interacting with a body has enjoyed significant interest due to its relevance to many applications, e.g., the unsteady evolution of lift over an airfoil due to the interaction of the *starting vortex* with the body [Tchieu and Leonard, 2011, Taha and Rezaei, 2020]. Ramodanov [2001] studied the interaction of a point vortex with a cylinder (the Föppl problem), then Borisov and Mamaev [2004] inspected the integrability of this problem. Moreover, Borisov et al. [2005,, 2007] and Ramodanov and Sokolov [2021] extended this setup to allow for multiple point vortices to interact with a cylinder. In another classic article by Shashikanth et al. [2002], the authors investigated the Hamiltonian dynamics of a cylinder interacting with a number of point vortices. In all of these efforts, the W function was considered as the main underlying foundation — the Hamiltonian function for the motion of constant-strength point vortices. If time-varying point vortices are considered instead of constant strength ones, then the W function will not be applicable, because a point vortex of constant-strength moves with the local flow velocity (the Kirchhoff velocity) according to Helmholtz laws of vortex dynamics [Helmholtz, 1858], while a vortex with time-varying strength does not, as it is well known in the unsteady aerodynamics literature [Eldredge, 2019, Wang and Eldredge, 2013, Michelin and Llewellyn Smith, 2009, Tchieu and Leonard, 2011, Tallapragada and Kelly, 2013, Hussein et al., 2018]. Though peripheral to the current study, it is important to mention some of the reduced-order modeling efforts in unsteady

aerodynamics. Several efforts have made significant contributions in this field. The study by Taha and Rezaei [2019] explores the extension of potential flow theories to account for viscous effects in lift response. [Yan et al., 2014] provides insights into airfoil dynamics during large maneuvers. The unsteady nonlinear aerodynamics of hovering MAVs/insects is addressed in [Taha and Hajj, 2013] while [Taha and Rezaei, 2020] offers a dynamical systems viewpoint on lift response. State-space approaches for unsteady aerodynamic models are utilized in [Taha and Rezaei, 2022] and the nonlinear dynamics of viscous lift response for pitching airfoils are examined in [Selim et al., 2023]. Moreover, Hussein et al. [2019] study investigates the transition dynamics in micro-air vehicles, providing key insights into the mechanisms involved in transitioning from hovering to forward flight. These studies collectively enhance the understanding and modeling of unsteady aerodynamic phenomena, aiding in the development of efficient aerodynamic designs, and the current proposed model could be utilized towards most of these studies.

Consider a vortex that is created at the TE of an airfoil and it is of continuous vorticity feed by the separated shear layer at the TE as shown in fig. 4.1, the vortex will be covecting while growing at the same time, however, it will not be moving (covecting) with the induced velocity due to other vortices and airfoil motion. In fact, it has to be moving with another velocity, this is due to that fact that if that vortex where to move with the local induced velocity then a fictitious barrier between this vortex and the TE drawn in the flow field would not have a balanced pressure on its sides (i.e., $P_u \neq P_l$). In other words, this fictitious barrier would hold force, a situation that violates the nature of fluid having continuous pressure. As a remedy, Brown and Michael [1954] developed a convection model (a first-order ODE in the vortex position) to describe the motion of time-varying point vortices, solely to overcome this dilemma of having a pressure discontinuity in the flow field. Their resulting ODEs was derived to cancel out the pressure discontinuity in the flow field, and made sure that the new convection velocity of the variable strength vortex satisfies that, it turns out, that the time varying strength vortices can not and must not convect with the local induced velocity. An alternative model, named the *Impulse Matching* model, was proposed by Tchieu and Leonard [2011] and Wang and Eldredge [2013]. Nevertheless, the resulting ODEs from Brown and Michael

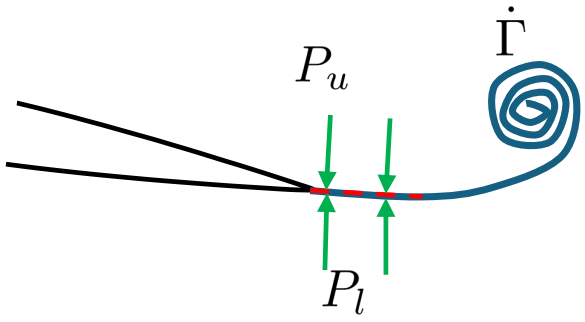

Figure 4.1: Schematic drawing for a time varying strength that is shed from the TE. The fictitious barrier along the shear layer feeding the vortex should not have a pressure discontinuity.

[1954], Tchieu and Leonard [2011] and Wang and Eldredge [2013] do not have a Hamiltonian structure; they can not be described by the KR function. An intuitive reasoning for the failure of the KR function in predicting the motion of unsteady point vortices, is that, formally, it does not contain any information beyond the Biot-Savart law, and when considered as a Hamiltonian, it is not derived from basic definitions. This argument reveals one of the needs for a variational dynamical framework that is constructed from first principles and capable of describing vortex dynamics, which is the main goal of this dissertation.

While there have been numerous efforts on the Hamiltonian formulation of point vortices, little have been done to develop a Lagrangian framework. This fact may be intuitive given the lack of veritable dynamics in these Hamiltonian formulations. A true mechanical system will possess both Lagrangian and Hamiltonian formulations, mutually related through the Legendre transformation [Goldstein et al., 2002]. However, having an arbitrary Hamiltonian function that happens to reproduce a given set of ODEs does not necessarily represent a mechanical system. As Salmon [1988] put it, "*the existence of a Hamiltonian structure is, by itself, meaningless because any set of evolution equations can be written in canonical form*". These non-standard Hamiltonians may not be associated with Lagrangian functions. However, there are a few exceptions. For example, Chapman [1978] devised a Lagrangian function that reproduces the set of ODEs dictated by the KR Hamiltonian. However, this Lagrangian was not derived from basic definitions or first principles in mechanics (i.e., it is not defined based on the kinetic and potential energies of the system), so

it had to be in a non-standard form (e.g., bi-linear in velocity, not quadratic) to result in first-order ODEs, in contrast to the second-order ODEs that typically result from a standard Lagrangian. In a similar spirit, Hussein et al. [2018] introduced a Lagrangian that reproduces the first-order ODEs of the Brown and Michael [1954] model, describing the motion of point vortices with time-varying strength. They used it to study the motion of the starting vortex behind an airfoil and its effect on the lift evolution similar to Wang and Eldredge [2013] and Tchieu and Leonard [2011].

In contrast to the previously mentioned efforts, there are a few studies that represented a mechanical structure (i.e., second-order ODEs in position) for the vortex motion. Ragazzo et al. [1994], considered point vortices with finite masses (i.e., massive-point vortices). Using an analogy with electromagnetism, they constructed a Hamiltonian of the massive-point vortices based on that of point charges in a magnetic field. Interestingly, the non-zero inertia of the point vortices (similar to the non-zero charge) resulted in second-order ODEs in position, leading to a richer behavior than that obtained using the KR function. However, the fact that the authors relied completely on analogy between hydrodynamics and electrodynamics to develop their dynamical model, perhaps sets no greater advantage over the devised KR Hamiltonian as far as first principles are concerned. Interestingly, Olva [1996] was able to show that their resulting ODEs reduce to those described by the KR function in the limit to a vanishing vortex mass, which, in turns, shows that the KR first-order ODEs is a singularly-perturbed representation of Ragazzo et al. [1994] second-order dynamics. More recently, Richaud et al. [2020] also considered massive-point vortices but in a super-fluid medium (i.e., Bose-Einstein condensate) using direct numerical simulation of the Gross-Pitaevskii (GP) equation. In addition, they modeled the motion of such vortices using variational principles where the Lagrangian is constructed based on analogy with charged particles subject to magnetic field. They compared the resulting dynamics from both approaches [Richaud et al., 2021, 2022], which resulted in an almost identical match. Moreover, similar to the results of Ragazzo et al. [1994], both approaches showed richer dynamics than that obtained by the KR function.

While we did our best to present the relevant literature to the reader, it is certain that we are far from

providing a complete account of the perhaps unfathomable literature on the topic. Nor is it our goal here to provide a comprehensive review of such a rich topic. For a thorough review and more information about point vortex dynamics, the reader is referred to multiple sources [Meleshko and Aref, 2007, Aref, 2007, Smith, 2011, Newton, 2014, Lamb, 1924, Batchelor, 1967, Saffman, 1992, Milne-Thomson, 1996, 1973, Eldredge, 2019, Wu et al., 2007, Alekseenko et al., 2007, Cottet et al., 2000, Truesdell, 1954].

In conclusion, although the previously discussed efforts were quite legitimate and spawned very interesting results [see Aref, 2007], they suffer from the following drawbacks: (1) the defined Hamiltonian and Lagrangian functions were neither derived from basic definitions in mechanics nor from the available rich literature on variational principles in fluid mechanics [Seliger and Whitham, 1968, Bateman, 1929, Salmon, 1988, Herivel, 1955, Bretherton, 1970, Penfield, 1966, Hargreaves, 1908, Serrin, 1959, Luke, 1967, Loffredo, 1989, Morrison, 1998, Berdichevsky, 2009]; (2) they were either devised to reproduce the already known ODEs or developed based on an analogy with another discipline; (3) as such, the resulting ODEs have no more content beyond the Biot-Savart law; (4) the fact that these functions were not derived from first principles does not allow extension to cases beyond free, constant-strength, point vortices. Indeed, one would hope to see a straightforward derivation of the Hamiltonian (or Lagrangian) of point vortices from basic definitions of mechanics (i.e., from kinetic and potential energies) or from the rich legacy of variational principles of continuum fluid mechanics [Seliger and Whitham, 1968, Bateman, 1929, Salmon, 1988, Herivel, 1955, Bretherton, 1970, Penfield, 1966, Hargreaves, 1908, Serrin, 1959, Luke, 1967, Loffredo, 1989, Morrison, 1998, Berdichevsky, 2009], which is the main goal of this work. Such a model will resolve the drawbacks listed above, resulting in second-order dynamics, allowing extension to unsteady vortices, and admitting arbitrary forces (e.g., gravity, electromagnetic, etc).

4.2 Hamiltonian of Point Vortices: the Kirchhoff-Routh Function

In this section, the KR function for free, constant-strength point vortices in an unbounded flow is presented, demonstrating its Hamiltonian role for constant-strength point vortices. The specified KR function is given by [Batchelor, 1967]

$$W = \frac{-1}{4\pi} \sum_{i} \sum_{\substack{j \\ i \neq j}} \Gamma_i \Gamma_j \ln r_{ij}, \tag{4.1}$$

where Γ's represent the strengths of the vortices, and r_{ij} is the relative distance between the i^{th} and j^{th} vortices. To show how this function serves as the Hamiltonian of free, constant-strength point vortices, let us recall the stream function describing the flow field at any particular point (x, y) in the domain

$$\Psi(x, y) = -\frac{1}{2\pi} \sum_{i} \Gamma_i \ln r_i, \tag{4.2}$$

where r_i is the distance between the point (x, y) and the i^{th} vortex. As such, the total induced velocity at the j^{th} vortex (ignoring the vortex self-induction) is given by

$$u_j = \frac{dx_j}{dt} = \frac{-1}{2\pi} \sum_{(i \neq j)} \Gamma_i \frac{(y_j - y_i)}{r_{ij}^2}, \qquad v_j = \frac{dy_j}{dt} = \frac{1}{2\pi} \sum_{(i \neq j)} \Gamma_i \frac{(x_j - x_i)}{r_{ij}^2}. \tag{4.3}$$

Then, multiplying eq. (4.3) by Γ_j allows writing its right-hand side in terms of the scalar function W as

$$\Gamma_j \frac{dx_j}{dt} = \frac{\partial W}{\partial y_j}, \qquad \Gamma_j \frac{dy_j}{dt} = \frac{-\partial W}{\partial x_j}. \tag{4.4}$$

Defining $q_j = \sqrt{\Gamma_j} x_j$ and $p_j = \sqrt{\Gamma_j} y_j$, it is clearly seen that if Γ_j is constant, then the ODEs eq. (4.4) is in the Hamiltonian form

$$\dot{q}_j = \frac{\partial W}{\partial p_j}, \qquad \dot{p}_j = \frac{-\partial W}{\partial q_j}, \tag{4.5}$$

with W serving as the Hamiltonian.

As demonstrated above, the KR Hamiltonian is not derived from basic definitions of mechanics in terms of kinetic and potential energies. This non-standard Hamiltonian reproduces the Biot-Savart equations in the Hamiltonian form eq. (4.5). However, one can relate this function W to the regularized Kinetic Energy (KE) as shown in [Batchelor, 1967, Saffman, 1992, Lamb, 1924, Milne-Thomson, 1996]. The KE (T) of the flow field is given by

$$T = -\frac{\rho}{4\pi} \sum_{\substack{i \\ i \neq j}} \sum_{j} \Gamma_i \Gamma_j \ln r_{ij} - \frac{\rho}{4\pi} \left(\sum \Gamma_i^2 \right) \ln \epsilon + \frac{\rho}{4\pi} \left(\sum \Gamma_i \right)^2 \ln r_\infty, \qquad r_\infty \to \infty, \epsilon \to 0, \tag{4.6}$$

where ϵ is a radius of an infinitesimal circle centered at every point vortex and r_∞ is the radius of the external boundary, which extends to infinity. It is clearly seen that the first term is exactly the W function scaled by the density ρ and the last two terms are unbounded as $r_\infty \to \infty$ and $\epsilon \to 0$. However, these two unbounded terms are constants and do not depend on the co-ordinates (i.e., positions of the vortices). As a result, the first term (the *regularized* KE) represents the only variable portion of the infinite KE and was satisfactorily considered as the Hamiltonian of point vortices, while the last two terms are dropped. The previous analysis is notably valid only for constant-strength point vortices and suffers from the several drawbacks discussed in the previous section. Alternatively, we rigorously develop a model for vortex dynamics from formal variational principles of continuum fluid mechanics, developed by Seliger and Whitham [1968].

4.3 The Principle of Least Action

Variational principles have not been popular for the past decades in the fluid mechanics literature. Penfield [1966] and Salmon [1988] asked "*Why Hamilton's principle is not more widely used in the field of fluid mechanics*?" The main reason—from our perspective—is that most of these principles are based on the principle of least action, which is essentially applicable to particle mechanics. Although it can be extended to continuum fluid mechanics in the Lagrangian formulation, the extension to the convenient Eulerian formulation invokes the introduction of artificial variables (e.g., Clebsch representation of the velocity field, [Clebsch, 1859]) and imposing additional constraints (e.g., Lin's constraints, [Lin, 1961]). As a result, these variational formulations are imbued with a sense of ad-hoc and contrived treatments in the literature. Nevertheless, several other studies have significantly advanced the theoretical understanding of aerodynamic principles through variational and minimization approaches. Gonzalez and Taha [2022] and Taha et al. [2023] delve into the fundamental principles governing lift and fluid mechanics. The intriguing question of "What does nature minimize in every incompressible flow?" by Taha and Gonzalez [2021] explores the natural minimization tendencies in fluid dynamics and is answered by revealing the Lagrangian that could be minimized in such flows. Also, the variational principles were utilized by Taha and Gonzalez [2023] to provide necessary conditions for lift production over flat plate, and Shorbagy and Taha [2024] apply Gauss's principles to estimate the Magnus forces over a rotating cylinder. These studies contribute to the deeper theoretical foundations necessary for advanced aerodynamic modeling and analysis through applying variational principles in fluid mechanics.

There are numerous efforts that developed variational principles of Euler's inviscid dynamics [Seliger and Whitham, 1968, Bateman, 1929, Salmon, 1988, Herivel, 1955, Bretherton, 1970, Penfield, 1966, Hargreaves, 1908, Serrin, 1959, Luke, 1967, Loffredo, 1989, Morrison, 1998, Berdichevsky, 2009]. The reader is referred to the thorough review articles of Salmon [1988] and Morrison [1998]. Also, there are many efforts that aimed at extending these variational formulations to account for dissipative/viscous forces [Yasue, 1983, Kerswell, 1999, Gomes, 2005, Eyink, 2010,

Fukagawa and Fujitani, 2012, Galley et al., 2014, Gay-Balmaz and Yoshimura, 2017]. In the current study, we mainly rely on the variational formulation of Euler's equation developed by Seliger and Whitham [1968] using the principle of least action.

The principle of least action is typically stated as *"The motion of the system from time t_1 to time t_2 is such that the action integral J is stationary"*, [Goldstein et al., 2002]

$$J = \int_{t_1}^{t_2} \mathcal{L}(q_i, \dot{q}_i, t)\ dt, \tag{4.7}$$

where $\mathcal{L}$ is the Lagrangian function, defined as $\mathcal{L} = T - V$ where T and V are the kinetic and potential energies, respectively, and q_i's are the system generalized co-ordinates. A necessary condition for the functional J to be stationary is that its first variation must vanish:

$$\delta\ J = \delta\ \int_{t_1}^{t_2} \mathcal{L}(q_i, \dot{q}_i, t)\ dt = 0, \tag{4.8}$$

which, after applying calculus of variation techniques [Burns, 2013], yields to the well-known Euler-Lagrange equation

$$\frac{d}{dt}\left(\frac{\partial \mathcal{L}}{\partial \dot{q}_i}\right) - \frac{\partial \mathcal{L}}{\partial q_i} = 0, \qquad i = 1, 2, ...n. \tag{4.9}$$

Noticeably, the representation in eq. (4.9) describes the dynamics of discrete particles only. However, if a continuum of particles is considered instead, the action integral J is written in terms of a *Lagrangian Density* $\mathcal{L}_d$ as

$$J = \int_{t_1}^{t_2} \int_{\Omega} \mathcal{L}_d\ (\boldsymbol{q}, \dot{\boldsymbol{q}}, \boldsymbol{q}_{\boldsymbol{x}}, \boldsymbol{x}, t)\ \ d\Omega dt, \tag{4.10}$$

where $\boldsymbol{x}$ are the spatial coordinate variables and Ω is the spatial domain. In this case, the generalized coordinates $\boldsymbol{q}$ are field variables (i.e., $\boldsymbol{q} = \boldsymbol{q}(\boldsymbol{x}, t)$) and eq. (4.9) should be generalized to the

continuous system representation [Goldstein et al., 2002]

$$\frac{d}{dt}\left(\frac{\partial \mathcal{L}_d}{\partial \dot{\boldsymbol{q}}_i}\right) + \frac{d}{dx}\left(\frac{\partial \mathcal{L}_d}{\partial \frac{d\boldsymbol{q}}{d\boldsymbol{x}}}\right) - \frac{\partial \mathcal{L}_d}{\partial \boldsymbol{q}_i} = 0. \tag{4.11}$$

Another point to consider is that tackling the variational formulation in an Eulerian frame of reference - which happens to be the adequate frame for studying fluids - needs special treatment. For example, the usual problem formulation of fixing the body and having an infinite flow over it, will result in a flow with infinite KE. So, the physical problem of having bodies translating in stationary liquids will be the candidate of our study. However, the main goal for mentioning these information, is to show that, once the Lagrangian for the specific problem being studied is found, then the process is straight forward, either for rigid body or continuum one. Based on all of the above, the variational formulation will be presented below to show exactly how the PLA will be utilized to study vortex dynamics; and for more information about the PLA, its limitations and modification, please refer to Goldstein et al. [2002].

4.4 Variational Formulation of Euler's Inviscid Dynamics: The Lagrangian Density is the Pressure

It is already known that Euler's equations governs the inviscid flow dynamics. This means, a proposed variational principle should reconstruct Euler's equations; and this was the main underlying motivation in Seliger and Whitham [1968] artifact. The Euler's equations along with the energy equation (i.e., continuity, momentum and energy conservation laws) read as

$$\frac{\partial \rho}{\partial t} + \nabla \cdot (\rho \boldsymbol{u}) = 0, \tag{4.12a}$$

$$\rho \frac{D\boldsymbol{u}}{Dt} = -\nabla P, \tag{4.12b}$$

$$\frac{DS}{Dt} = 0. \tag{4.12c}$$

The variational approach should reconstruct these equations using the PLA in an Eulerian frame of reference (the original article, described the same formulation in a Lagrangian frame as well, however, it is of no use for the current study and it will not be discussed for brevity). Consider the PLA for a continuous field defined in eq. (4.10) and letting $\mathcal{L} = T - V$, one could simply write the variation to be

$$\delta\, J = \delta \int_{t_1}^{t_2} \int_{\Omega} \left[\frac{1}{2} \rho \boldsymbol{u}^2 - \rho E(\rho, S) \right] d\Omega dt = 0, \tag{4.13}$$

where the first term in the integrand represents the KE, E is the internal energy per unit mass, which represents the potential energy of the fluid continuum, and S is the entropy whose changes are related to those of E as

$$dE = \Theta dS - p d(1/\rho), \tag{4.14}$$

where p is the pressure, and Θ is the temperature. Applying the variation with respect to $\boldsymbol{u}$, then substitute the result in eq. (4.11), a trivial answer of $\boldsymbol{u} = 0$ will be found. This result is due to the fact that there is no forcing constraint over the prescribed Lagrangian to ensure the particle will behave in a continuum manner. As a remedy, eqs. (4.12a) and (4.12c) need to be introduced as constraints. So, two Lagrange multipliers are adopted, ϕ and η for the continuity and energy equation respectively, where the energy equation is written in the conservative form. Then, the new

first variation read as

$$\delta\ J = \delta \int_{t_1}^{t_2} \int_{\Omega} \frac{1}{2}\rho \boldsymbol{u}^2 - \rho E(\rho, S) + \phi\ [\partial_t \rho + \nabla \cdot (\rho \boldsymbol{u})] + \eta\ [\partial_t (\rho S) + \nabla \cdot (\rho \boldsymbol{u} S)]\ \ d\Omega dt = 0, \quad (4.15)$$

which defines a new Lagrangian, that if substituted into eq. (4.11), while considering the variation with velocity -$\delta \boldsymbol{u}$ - as before, will result in

$$\boldsymbol{u} = \nabla \phi + S \nabla \eta. \quad (4.16)$$

Interestingly, the velocity representation is not trivial as before, and the Lagrangian present in eq. (4.15) can describe flow fields velocity possessing the form in eq. (4.16). However, this velocity form is restricted to certain types of flows. For instance, if the entropy is considered constant while having an incompressible flow, then the proposed Lagrangian can only represent irrotational flows, which is limiting in its nature. The drawback of being only capable of describing limiting types of flow fields is resolved after Lin [1961] efforts, where he introduced another constraint over the formulation. The constraint is that, even in the Eulerian formulation where the Lagrangian co-ordinates (i.e., markers) $\boldsymbol{\alpha}$ are not needed, the velocity fields considered should be the ones where the Lagrangian markers $\boldsymbol{\alpha}$ could be found from the Eulerian variables at any instant. This would translate in Eulerian description such that, the initial Lagrangian markers $\boldsymbol{\alpha}(\boldsymbol{x}, t)$ are traceable at any instance and they do not change along the particle path. Hence,

$$\frac{D\boldsymbol{\alpha}}{Dt} = 0. \quad (4.17)$$

This constraint was introduced without proper justification other than what is mentioned, and was adopted in previous studies [Bretherton, 1970]. However an elegant representation for this constraint was shown by Salmon [1988], where Lin's constraint appeared naturally while transforming the action integral from the Lagrangian formulation to the Eulerian one knowing that the flow map

which transforms the $\boldsymbol{\alpha}$ markers to $\boldsymbol{x}$ co-ordinate should be a one-to-one invertable map. This fact is closely tied to the geometrical representation of the Euler equation, where it could be considered as " *the geodesic on the group of volume preserving diffeomorphisms*" [Khalifa, 2019]. Using the Lagrangian introduced in eq. (4.15) and eq. (4.17) in the conservative form with the Lagrange multiplier β, one can reach a new variation written as

$$\delta\, J = \delta \int_{t_1}^{t_2} \int_{\Omega} \frac{1}{2}\rho \boldsymbol{u}^2 - \rho E(\rho, S) + \phi\left[\partial_t \rho + \nabla \cdot (\rho \boldsymbol{u})\right] + \eta\left[\partial_t(\rho S) + \nabla \cdot (\rho \boldsymbol{u} S)\right] + \beta\left[\partial_t(\rho\alpha) + \nabla \cdot (\rho \boldsymbol{u}\alpha)\right]\; d\Omega dt = 0. \quad (4.18)$$

Finally, after varying it with respect to velocity, the resulting velocity field described by this Lagrangian will be

$$\boldsymbol{u} = \nabla\phi + S\nabla\eta + \alpha\nabla\beta. \quad (4.19)$$

The new velocity representation is more enabling, in the sense that it allows for vorticity to be introduced initially and to be separated from the vorticity generated by entropy change. Knowing that vorticity is $\omega = \nabla S \times \nabla\eta + \nabla\alpha \times \nabla\beta$. So, for isentropic flows the velocity field will posses the form

$$\boldsymbol{u} = \nabla\phi + \alpha\nabla\beta, \quad (4.20)$$

where ϕ is responsible for the irrotational flows and β for rotational ones. However, from regular vector calculus it is known that any velocity field could be decomposed into to separate components, one has the irrotational information $\boldsymbol{v}_\phi$ and the other has the rotational one $\boldsymbol{v}_\omega$; and the velocity field is the gradient of the former and curl of the latter

$$\boldsymbol{v} = \boldsymbol{v}_\phi + \boldsymbol{v}_\omega = \nabla\phi + \nabla \times \psi, \quad (4.21)$$

which contradicts eq. (4.20). In other words, the question which possess itself is, could one decompose any flow filed based on eq. (4.20)? The answer lies in what is called the *"Clebsch"* representation. Clebsch [1859] showed that any isentropic flow field could be represented as

$$\boldsymbol{v} = \nabla\chi + \lambda\nabla\mu, \tag{4.22}$$

which conforms with the representation in eq. (4.20) and the Lagrangian represented in eq. (4.18) is complete. However, this Lagrangian - in this form - is not of practical use while tackling problems. So, an extra simplification is carried over eq. (4.18) through integration by parts and neglecting boundary terms [Seliger and Whitham, 1968], which will yield

$$\mathcal{L}_d = \frac{1}{2}\rho\boldsymbol{u}^2 - \rho E - \rho\frac{D\phi}{Dt} - \rho S\frac{D\eta}{Dt} - \rho\alpha\frac{D\beta}{Dt}, \tag{4.23}$$

and simplifies the Lagrangian for practicality.

The form in eq. (4.23) is the one that could be implemented towards a practical application. However, as mentioned before, the Lagrangian should be related to physical quantities such as KE or PE. It is clear, that the first term in eq. (4.23) is the flow KE, but what about the rest? Based on that, and in attempt to answer this question, Seliger and Whitham [1968] took the variation of eq. (4.18) with respect to ρ instead of $\boldsymbol{u}$ and combined the result with eq. (4.14) which in turns resulted in

$$H = \frac{1}{2}\boldsymbol{u}^2 - \frac{D\phi}{Dt} - S\frac{D\eta}{Dt} - \alpha\frac{D\beta}{Dt}, \tag{4.24}$$

where H is the enthalpy. The previous form, allowed eq. (4.23) to be written as

$$\mathcal{L}_d = \rho H - \rho E = -p, \tag{4.25}$$

showing that the Lagrangian density is no more than the pressure.

As a recap, the straightforward definition of the action integral for a fluid continuum is

$$J = \int_{t_1}^{t_2} \int_{\Omega} \left[\frac{1}{2} \rho \boldsymbol{u}^2 - \rho E(\rho, S) \right] \, d\Omega dt, \tag{4.26}$$

Starting with the action eq. (4.26), making use of Clebsch's representation and Lin's constraints, Seliger and Whitham [1968] managed to show that the functional J can be written in the Eulerian formulation as

$$J = - \int_{t_1}^{t_2} \int_{\Omega} p \, \, d\Omega dt. \tag{4.27}$$

That is the vanishing of first variation of J yields the conservation equations of an inviscid fluid eq. (4.12).

Since the flow outside vortex patches is irrotational by definition, one can use the unsteady Bernoulli equation to write the pressure in terms of the velocity potential ϕ. As such, the principle of least action will then imply that the first variation of the functional

$$J = - \int_{t_1}^{t_2} \int_{\Omega} \rho \left\{ \partial_t \phi + \frac{1}{2} \left(\nabla \phi \right)^2 \right\} \, d\Omega dt, \tag{4.28}$$

must vanish [Seliger and Whitham, 1968]. This statement is the cornerstone in our analysis for vortex dynamics.

Chapter 5

Variational Dynamics of Massive Vortices

We apply the proposed variational formulation to develop a model for the dynamics of massive vortices with small core sizes. In particular, we consider N Rankine vortices; a Rankine vortex is a vortex patch in the two-dimensional plane with a non-zero core size which has a circular boundary; and the fluid inside the core undergoes a rigid-body rotation (i.e., it has constant vorticity over the core). As such, the vortex possesses a non-zero mass (i.e., a massive vortex), in contrast to point vortices which have no mass. The induced flow field outside the vortex core is irrotational [Saffman, 1992]. In our formulation, each vortex must have a core (of radius a_i) to ensure a finite KE and allow the vortex inertial effects to appear. It is important to mention that constant-strengths and radii sizes are considered for simplicity and facilitating comparison with available models in literature.

The domain consists of an irrotational flow in region A outside the vortex core and fluid under rigid-body motion inside the core, as shown in fig. 5.1. Knowing the vortex strengths a priori, the flow velocity $\boldsymbol{u}$ at any point (x, y) in the domain can be written in terms of the locations (x_i, y_i) of the vortices and their derivatives

$$\boldsymbol{u}(x, y) = \boldsymbol{u}(x_i, y_i, \dot{x}_i, \dot{y}_i; \Gamma_i). \tag{5.1}$$

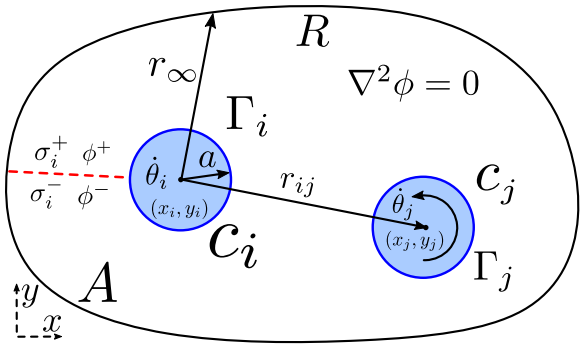

Figure 5.1: Schematic drawing for the problem formulation; c_i is the boundary of the i^{th} vortex in solid blue, σ_i is the corresponding branch cut (barrier) in dashed red and R is the boundary of flow domain in black.

This representation is the foundation of the current analysis; the flow velocity in the entire domain depends only on a finite number of variables (x_i, y_i). That is, eq. (5.1) represents a model reduction from infinite number of degrees of freedom down to only 2N. As such, the principle of least action, and analytical mechanics formulation in general, are especially well suited for this problem because it allows one to accept the given kinematical constraints (5.1) and focus on the dynamics of the reduced system (2N degrees of freedom), in contrast to the Newtonian-mechanics formulation where such a reduction is not possible. Rather, the large system must be retained (i.e., a PDE for the infinite system at hand) and the kinematic constraint (5.1) will be associated with an unknown constraint force in the equations of motion of the large system (in the PDE).

The above description implies that the Lagrangian has two contributions

$$\mathcal{L} = \mathcal{L}_\phi + \mathcal{L}_C, \tag{5.2}$$

where $\mathcal{L}_\phi$ is the Lagrangian of the irrotational flow outside the cores and $\mathcal{L}_C$ is the core Lagrangian. The action integral is then given by

$$J = \int_{t_1}^{t_2} \left(\int_A \mathcal{L}_{d_\phi}\, dA + \mathcal{L}_C \right) (x_i(t), y_i(t), \dot{x}_i(t), \dot{y}_i(t); \Gamma_i)\, dt, \tag{5.3}$$

where $\mathcal{L}_{d_\phi}$ is the Lagrangian density of the continuum field, which is $-p$, as shown by Seliger

and Whitham [1968] and presented in the previous section. After integrating the fluid Lagrangian density $\mathcal{L}_{d_\phi}$ over space, the problem could be treated as one with finite degrees of freedom (x_i, y_i)—akin to particle mechanics.

The Lagrangian of the core flow under rigid-body motion in the horizontal plane (i.e., no active gravitational forces) is

$$\mathcal{L}_C = \sum \frac{m_i}{2} \boldsymbol{u}_i \cdot \boldsymbol{u}_i + \sum \frac{I_i}{2} \dot{\theta}_i^{\,2}, \tag{5.4}$$

where m_i is the fluid mass inside the i^{th} vortex core and I_i is its moment of inertia. As mentioned before, constant-strength vortices are considered. Hence, the angular velocity $\dot{\theta}_i$ of each rigid core (which is proportional to Γ_i) is constant. This immediately forces the θ co-ordinate to be an ignorable/cyclic coordinate [Lanczos, 2020]. In other words, the corresponding momentum $\partial \mathcal{L}_C / \partial \dot{\theta}$ is constant. It now remains to compute the Lagrangian of the continuum fluid outside the cores in terms of the generalized coordinates $\boldsymbol{q} = (x_1, y_1, ..., x_N, y_N)$.

5.1 Irrotational Flow Lagrangian Computation

The Lagrangian density of the inviscid fluid, as discussed in section 4.4, is the pressure. It is given by eq. (4.28), where the second term is the flow KE and the first term is due to the $\partial_t \phi$ term.

5.1.1 Flow KE

Calculating the KE for vortex flows is not a trivial task. In fact, Saffman [1992] wrote *"The use of variational methods for the calculation of equilibrium configurations is rendered difficult by the absence of simple and accurate formulae for the calculation of the kinetic energy"*. Overcoming this obstacle is one of the goals of this study, by deriving an accurate formula for a finite KE for

vortex flows from basic definitions of mechanics.

Consider the flow KE of the irrotational flow field in fig. 5.1

$$T = \frac{\rho}{2}\int_A \boldsymbol{u}\cdot\boldsymbol{u}\ dA = \frac{\rho}{2}\int_A (\nabla\phi)^2\ dA, \tag{5.5}$$

where A is the irrotational flow field domain. After following the analysis in appendix A, the KE can be written as:

$$T = -\frac{\rho}{2}\left[\sum_{i\neq j}\sum \Gamma_i\psi_j|_i + \sum \Gamma_i\psi_i|_{c_i} + \Psi|_R\Gamma_R + \sum \Gamma_i\Psi|_R\right], \tag{5.6}$$

where $\psi_j|_i$ is the stream function of the irrotational flow induced by the j^{th} vortex evaluated at the center of the i^{th} one (this is applicable as long as $r_{ij} >> a$), $\psi_i|_{c_i}$ is the i^{th} vortex stream function evaluated over its boundary c_i, $\Psi|_R$ is the total stream function (due to all vortices; i.e., $\Psi = \sum_j \psi_j$) evaluated at the boundary R and Γ_R is the circulation over the same boundary. For an irrotational flow, Γ_R is the sum of all circulations inside the domain (i.e., $\Gamma_R = \sum_i \Gamma_i$). The fourth term results from the multi-valued nature of the potential function ϕ when evaluated over the fictitious barrier σ_i for the i^{th} vortex. Equation (5.6) is then written as

$$T = -\frac{\rho}{4\pi}\sum_{i\neq j}\sum \Gamma_i\Gamma_j \ln r_{ij} - \frac{\rho}{4\pi}\left(\sum \Gamma_i^2\right)\ln a + \frac{\rho}{4\pi}\left(\sum \Gamma_i\right)^2 \ln r_\infty - \frac{\rho}{2}\Psi|_R\Gamma_R, \tag{5.7}$$

where a is the core radius. The terms in eq. (5.6) can be compared to the regularized KE presented in eq. (4.6). The first term is exactly the KR function for free N point vortices, while the second terms in both match with the core radius a taking place of the limit circle radius ϵ. The second term, in eq. (5.7) will be retained, unlike the traditional analysis, which ignores it on the account that it is a constant term that should not affect the variational analysis. In fact, this term will be of paramount importance if Γ_i is a degree of freedom, so its dynamics will be determined simultaneously from the same variational formulation. Also, the third terms match, which will blow up for unbounded

flows except if the total circulation is zero. The fourth term in eq. (5.6) is an additional term that is not captured in eq. (4.6). However, similar to the third term, it is infinite for unbounded flows unless $\Gamma_R = 0$. In fact, the main reason behind the boundedness of the last two terms in the case of zero total circulation is that, the velocity will be of order $\sim O(1/r^2)$ in contrast to $\sim O(1/r)$ for a non-zero total circulation [Cottet et al., 2000]. In summary, to obtain a finite KE, we must have: (1) vortex patches of finite sizes instead of infinitesimal ones (i.e., point vortices), and (2) zero total circulation. This last condition is interesting and thought provoking. Aside from the mathematical reason mentioned above ($O(1/r^2)$ Vs $O(1/r)$), we may think of the following physical reason. In reality, there should not be an unbounded irrotational flow with a non-zero total circulation. If we always start from a stationary state (i.e., $\Gamma_R = 0$), Kelvin's conservation of circulation dictates that the total circulation must remain unchanged; if there is a circulation created somewhere in the flow (e.g., around a body), there must be a vortex of equal strength and opposite direction somewhere else in the flow field (e.g., a starting vortex over an airfoil [Glauert, 1926]). It is interesting that such a behavior is encoded into the KE.

It is important to mention that if the vortex boundary deforms, it will result in a time-varying moment of inertia $I(t)$, precluding the cyclic nature of the angular motion θ even for constant-strength vortices. In this study, however, we ignore such changes in the vortex boundary shape. This is a reasonable assumption as long as the distance between the vortices is considerably larger than the vortex core size [Lamb, 1924]. In other words, vortex patches could interact and deform when they are close to each other; this behavior is studied as a *Contour Dynamics* problem [Zabusky et al., 1979, Pullin, 1992, Saffman, 1992], where Melander et al. [1986] provided a Hamiltonian representation for it. However, in this first-order study, we are concerned with vortex patches concentrated in tiny cores and hence ignore the effect of shape deformation, which is one step beyond the point-vortex model. Luckily, it was shown by Deem and Zabusky [1978], Pierrehumbert [1980] and Saffman and Szeto [1980] that any vortex pairs distantly apart from each other, as long as $a/b << 1$ where b is half the distance between the two vortices center, will behave as if they were point vortices and not deform the boundary of each other.

5.1.2 $\partial_t \phi$ Contribution to the Lagrangian

The total flow potential function is defined as

$$\phi = \sum_i \phi_i, \tag{5.8}$$

where ϕ_i is the potential function of the flow associated with the i^{th} vortex, which depends on $(x, y, ; x_i(t); y_i(t); \Gamma_i)$. That is, it does not have an explicit time-dependence. Rather, its time-derivative will be a convective-like term with respect to the Lagrangian co-ordinates (x_i, y_i)

$$\partial_t \phi = \sum_i \boldsymbol{u}_i \cdot \nabla_i \phi_i. \tag{5.9}$$

As such, the $\partial_t \phi$ contribution to the Lagrangian can be written as

$$\mathcal{L}_{\phi_t} = \rho \int_A \partial_t \phi dA = \rho \int_A \sum_i \boldsymbol{u}_i \cdot \nabla_i \phi_i \, dA, \tag{5.10}$$

whose direct computation is cumbersome. Instead, we will apply eq. (4.9) first. For example, consider the term $\partial \mathcal{L}_{\phi_t} / \partial \dot{x}_i$, which is needed for the x_i equation of motion. By definition, we have

$$\frac{\partial \mathcal{L}_{\phi_t}}{\partial \dot{x}_i} = \rho \partial_{\dot{x}_i} \int_A \sum_i \boldsymbol{u}_i \cdot \nabla_i \phi_i \, dA, \tag{5.11}$$

where the differentiation can be pushed forward within the integral because the integral bounds are independent of the vortex velocity $\dot{x}_i$. As such, all terms will vanish except

$$\frac{\partial \mathcal{L}_{\phi_t}}{\partial \dot{x}_i} = \rho \int_A \partial_{x_i} \phi_i \, dA. \tag{5.12}$$

Moreover, since there is no explicit time-dependence and assuming constant-strength vortices, the time-derivative of eq. (5.12) is

$$\frac{d}{dt}\left(\frac{\partial \mathcal{L}_{\phi_t}}{\partial \dot{x}_i}\right) = \rho \boldsymbol{u}_i \cdot \nabla_i \left(\int_A \partial_{x_i}\phi_i \; dA\right) = \rho \left\{\dot{x}_i \partial_{x_i} \int_A \partial_{x_i}\phi_i \; dA + \dot{y}_i \partial_{y_i} \int_A \partial_{x_i}\phi_i \; dA\right\}. \tag{5.13}$$

Similarly, the other derivative $\partial \mathcal{L}_{\phi_t}/\partial x_i$ needed for the x_i equation is written as

$$\frac{\partial \mathcal{L}_{\phi_t}}{\partial x_i} = \rho \partial_{x_i} \int \sum_j \boldsymbol{u}_j \cdot \nabla_j \phi_j \; dA = \rho \left\{\dot{x}_i \partial_{x_i} \int_A \partial_{x_i}\phi_i \; dA + \dot{y}_i \partial_{x_i} \int_A \partial_{y_i}\phi_i \; dA\right\}. \tag{5.14}$$

Consequently, subtracting eq. (5.14) from eq. (5.13) will result in the cancellation of the first term in the x_i equation of motion. As such, we have

$$\frac{d}{dt}\left(\frac{\partial \mathcal{L}_{\phi_t}}{\partial \dot{x}_i}\right) - \frac{\partial \mathcal{L}_{\phi_t}}{\partial x_i} = \rho \dot{y}_i \left[\partial_{y_i} \int_A \partial_{x_i}\phi_i \; dA - \partial_{x_i} \int_A \partial_{y_i}\phi_i \; dA\right], \tag{5.15}$$

which, after the detailed computation presented in appendix B, yields

$$\frac{d}{dt}\left(\frac{\partial \mathcal{L}_{\phi_t}}{\partial \dot{x}_i}\right) - \frac{\partial \mathcal{L}_{\phi_t}}{\partial x_i} = \rho \dot{y}_i \left[\sum_{\substack{j \\ i \neq j}} \left(\int_{c_j} \partial_{x_i}\phi_i \; dx - \int_{c_j} \partial_{y_i}\phi_i \; dy\right) - \Gamma_i\right], \tag{5.16}$$

where the final integrals are evaluated numerically over the j^{th} vortex boundary c_j. Also, for clarity and brevity, the numerical integrals are denoted as

$$I_{x_{ij}} = \int_{c_j} \partial_{x_i}\phi_i \; dx, \qquad I_{y_{ij}} = \int_{c_j} \partial_{y_i}\phi_i \; dy, \tag{5.17}$$

resulting in the final form

$$\frac{d}{dt}\left(\frac{\partial \mathcal{L}_{\phi_t}}{\partial \dot{x}_i}\right) - \frac{\partial \mathcal{L}_{\phi_t}}{\partial x_i} = \rho \dot{y}_i \left[\sum_{\substack{j \\ i \neq j}} \left(I_{x_{ij}} - I_{y_{ij}}\right) - \Gamma_i\right]. \tag{5.18}$$

Similarly, the y_i equation is

$$\frac{d}{dt}\left(\frac{\partial \mathcal{L}_{\phi_t}}{\partial \dot{y}_i}\right) - \frac{\partial \mathcal{L}_{\phi_t}}{\partial y_i} = \rho \dot{x}_i \left[\sum_{\substack{j \\ i \neq j}} \left(I_{y_{ij}} - I_{x_{ij}}\right) + \Gamma_i\right]. \tag{5.19}$$

5.2 Equations of Motion

We are now ready to write the final form of the equations of motion from the Euler-Lagrange eq. (4.9), where $\boldsymbol{q} = (x_1, y_1, ..., x_N, y_N)$, the Lagrangian $\mathcal{L} = \mathcal{L}_\phi + \mathcal{L}_C$, the contributions of different terms are given in eqs. (5.4), (5.7), (5.18) and (5.19).

Substituting eqs. (5.4), (5.7), (5.18) and (5.19) into the Euler-Lagrange eq. (4.9), while assuming the motion taking place in a horizontal plan; we obtain

$$m_i \ddot{x}_i + \frac{\rho \Gamma_i}{2\pi} \sum_{\substack{j \\ i \neq j}} \Gamma_j \frac{(x_i - x_j)}{r_{ij}^2} + \rho \dot{y}_i \left[\sum_{\substack{j \\ i \neq j}} \left(I_{x_{ij}} - I_{y_{ij}}\right) - \Gamma_i\right] = 0, \tag{5.20}$$

$$m_i \ddot{y}_i + \frac{\rho \Gamma_i}{2\pi} \sum_{\substack{j \\ i \neq j}} \Gamma_j \frac{(y_i - y_j)}{r_{ij}^2} + \rho \dot{x}_i \left[\sum_{\substack{j \\ i \neq j}} \left(I_{y_{ij}} - I_{x_{ij}}\right) + \Gamma_i\right] = 0, \tag{5.21}$$

with noting $m_i = \rho \pi a^2$, results in

$$\ddot{x}_i = -\frac{\Gamma_i}{2\pi^2 a^2} \sum_{\substack{j \\ i \neq j}} \Gamma_j \frac{(x_i - x_j)}{r_{ij}^2} - \frac{\dot{y}_i}{\pi a^2} \left[\sum_{\substack{j \\ i \neq j}} \left(I_{x_{ij}} - I_{y_{ij}}\right) - \Gamma_i\right], \tag{5.22}$$

$$\ddot{y}_i = -\frac{\Gamma_i}{2\pi^2 a^2} \sum_{\substack{j \\ i \neq j}} \Gamma_j \frac{(y_i - y_j)}{r_{ij}^2} - \frac{\dot{x}_i}{\pi a^2} \left[\sum_{\substack{j \\ i \neq j}} \left(I_{y_{ij}} - I_{x_{ij}}\right) + \Gamma_i\right]. \tag{5.23}$$

These equations represent the sought dynamical equations that describe the dynamics of free

massive vortices from first principles: the Principle of Least Action. They are second-order in nature and capture inertial effects of the core. In particular, they allow enforcing an initial condition on velocity, similar to any typical problem in dynamics. Moreover, the analysis allows for extension to time-varying vortices where $\dot{\Gamma}$-terms appear. Also, arbitrary conservative forces (e.g., gravitational, electric) can be incorporated in this framework, in contrast to the standard analysis based on the KR function. Interestingly, in the limit of a vanishing core size ($a \to 0$), m_i, $I_{x_{ij}}$ and $I_{y_{ij}}$ go to zero, and the resulting dynamics (5.22) and (5.23) reduce to the first-order equations given by the KR Hamiltonian. However, for finite-size cores, the new dynamics given by eqs. (5.22) and (5.23) are richer than the first-order equations of the KR Hamiltonian, which recover the Biot-Savart law. To show the value of the proposed new formulation, some case studies are presented below.

5.3 Case Studies

Different case studies are presented to highlight the similarity and differences between the motions resulting from the proposed model and the standard KR model (i.e., Biot-Savart law). As pointed above, the proposed variational dynamics result in the KR solution for small vortex radii. One of the major differences between the two formulations is that the KR equations are first-order allowing only initial conditions of vortex position to be assigned whereas the proposed equations are second-order, admitting arbitrary initial velocities in addition. Therefore, the similarity between the resulting two motions does not necessarily happen when the initial velocities do not match the induced velocities by the Biot-Savart law.

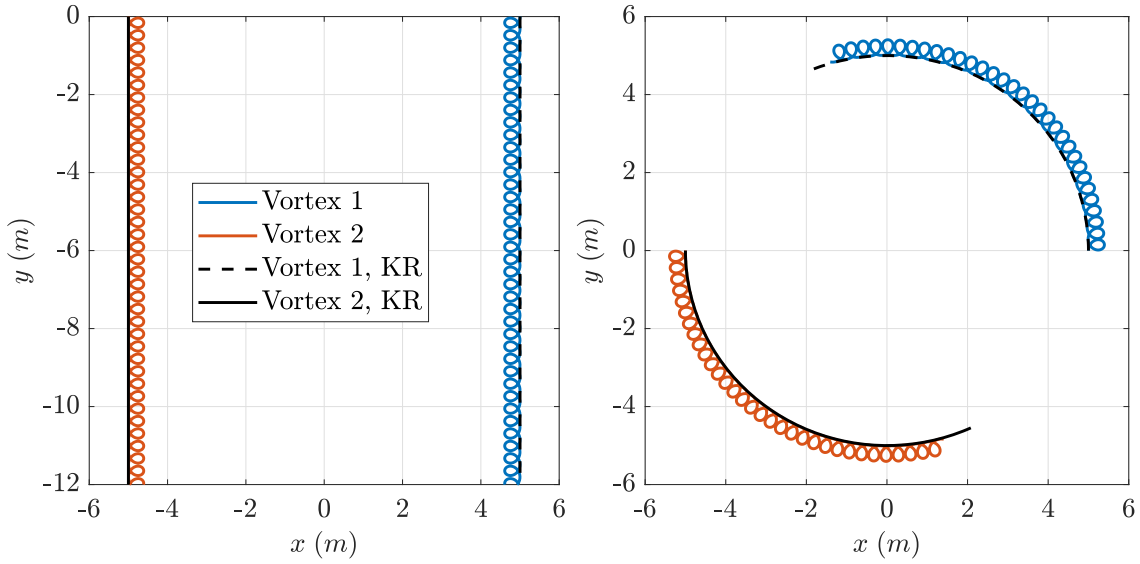

(a) counter-rotating pair

(b) co-rotating pair

Figure 5.2: Simulation of proposed variational vortex dynamics model against the KR model for a pair of vortices. The initial velocities are set to five multiples of the Biot-Savart induced velocity in the same direction.

5.3.1 Vortex Pairs Initialized With Arbitrary Velocities

Equal strength vortex pairs are considered in fig. 5.2 with radius $a = 1$ and $\Gamma = 10\pi$. The trajectories of the vortex pairs are presented in comparison to the KR motion. The trajectory of a counter-rotating vortex pair is shown in fig. 5.2a while fig. 5.2b shows the trajectory of a co-rotating pair. For this case of small vortex cores (in comparison to the relative distance), when the model is initialized with the Biot-Savart induced velocity, almost-exact matching with the KR motion (black trajectory in fig. 5.2) is obtained. However, when the proposed model is initialized with a different value in the same direction, the resulting dynamics (red and blue trajectories in fig. 5.2) are richer. The resulting motion is composed of fast and slow time scales. The slow dynamics (average solution) possesses a similar behavior to the KR one (in many but not all cases, as shown below), around this averaged response, there are oscillations in the fast time scale.

The behavior of the slow dynamics is not always similar to that of the KR model. In fig. 5.3, a pair of counter-rotating vortices are simulated, and the system is initialized with the Biot-Savart induced

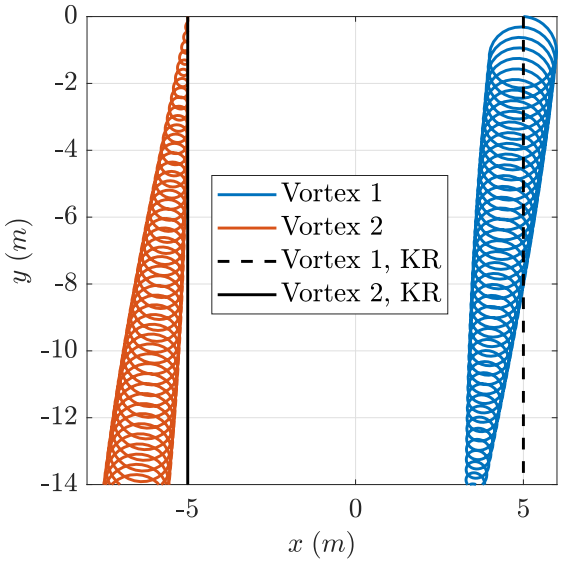

Figure 5.3: Simulation of the variational vortex dynamics model presenting the deviation of a counter-rotating vortex pair from the KR trajectory. Initial velocities for the vortices are $u_{1_0} = (10i, -0.5j)$ and $u_{2_0} = (0i, -0.5j)$, respectively.

velocity (i.e., down), however, the vortex on the right is given an additional initial velocity to the right. These initial conditions resulted in quite different averaged behaviors of the two vortices, as shown in fig. 5.3. The effect of the initial velocity on the averaged motion of interacting vortices, as demonstrated above, points to some interesting applications of vortex motion control. Imagine a large vortex that we like to deviate its motion from an anticipated trajectory. One can then pose the interesting question: Can we set a group of vortices in motion with specified initial velocities in the neighborhood of the large vortex so that its net motion deviates from the anticipated trajectory in the absence of these vortices? Using a similar approach to the one presented above, one can answer such a question.

A non-dimensional parameter is introduced to further quantify the fast dynamic oscillations that are captured in previous results. The non-dimensional parameter is defined as

$$\beta = \frac{\omega a^2}{\Gamma b}, \tag{5.24}$$

where ω is the fast dynamics oscillation frequency computed using the Fourier transform. The β

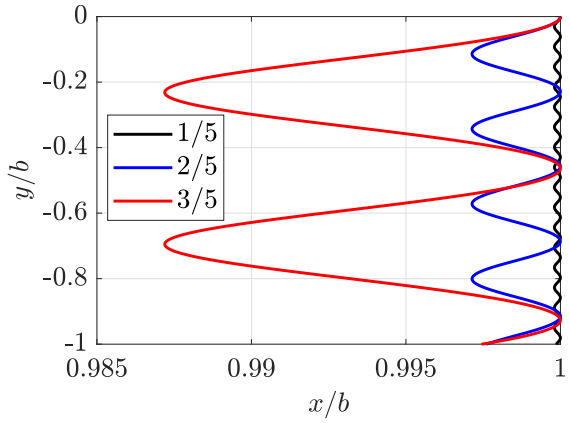

Figure 5.4: Sensitivity study for different a/b ratios. Trajectories for the right hand side vortex is presented. Scale is adjusted to emphasize the differences between each case.

value for all the cases studied is 0.064. It is notable to mention that changing the a/b ratio or the vortex strength Γ might change the fast oscillation dynamics frequency ω, and further study for the effect of the β parameter on the dynamics is needed.

A sensitivity study is carried out in an attempt to quantify the fast oscillation dynamics that is superimposed over the regular KR solution. The amplitude and frequency of oscillation are characterized against different a/b ratios. This study is performed on the example of counter-rotating pair initialized with the Biot-Savart induced velocity. The resulting trajectories of the right-hand side vortex, scaled with respect to the half-separating distance b, are shown in fig. 5.4. The plots demonstrate the oscillation dynamics for different values of a/b. It is evident that the amplitude of oscillation is directly proportional to a/b, however, the oscillation frequency is inversely proportional to this ratio. A qualitative description of the underlying phenomenon could be deduced from the (introduced) acceleration terms, which account for inertial effects in the equations of motions by considering the vortex mass. Hence, larger vortices tend to oscillate slower with large amplitudes and vice versa. It is not easy to quantify these effects analytically due to the strong nonlinearities in the equations of motion. However, approximate analytical expressions could be obtained using perturbation techniques (e.g., the method of multiple scales [Nayfeh and Mook, 2008, Nayfeh, 2011]).

5.3.2 Hydrodynamic and Electrodynamic Forces Interaction

To further demonstrate the capability of the developed vortex model to capture dynamical features that cannot be directly captured by the usual KR formulation, we consider a charged particle inside the core of each vortex and that the motion takes place in the presence of a constant-strength electric field. In this case, each vortex will experience a *Lorentz* force $\boldsymbol{F} = q\boldsymbol{E}$, where q is the particle's charge and $\boldsymbol{E}$ is the electric field vector. The effect of this electric field on the motion of the vortex system cannot be directly obtained from the standard formulation using the KR function. A true dynamical formulation is invoked instead. It is straightforward to account for this effect using the developed dynamical formulation where forces can be considered. Simply, the right hand sides of eqs. (5.22) and (5.23) will be modified by adding $q_i E_x/m_i$ and $q_i E_y/m_i$, respectively, where E_x and E_y are the components of the electric field in the x and y directions, respectively, and q_i is the charge of the i^{th} vortex. Alternatively, one can add $-\sum_i q_i \Phi(x_i, y_i)$ to the Lagrangian function, where Φ is the scalar electrostatic potential ($\boldsymbol{E} = -\boldsymbol{\nabla}\Phi$). For simplicity, we considered a large electric field and small charges so that the *Coulomb* force is negligible with respect to the Lorentz force. In the following simulations, we considered $|q\boldsymbol{E}|/m = g$, where g is the gravitational acceleration, and all motions are initialized with the KR velocities. Also, the main outcome of the new proposed variational model is to account for any conservative or non-conservative forces in a straight forward manner without having to resort to proposing a simplified model that satisfies the full Navier-Stokes and Maxwell's equations. Kennedy and Van Gorder [2018] were able to couple the electro-dynamic and hydrodynamic forces by proposing a model based an order of magnitude analysis for a 3D filament. However, the result is not a direct ordinary-differential equation of motions for the vortex filament dynamics opposing to the straight forward and direct account for the electrodynamics forces in our model.

Figure 5.5 shows a pair of counter-rotating vortices of the same strength and the same charge placed in an electric field of constant strength. Figure 5.5a shows the resulting motion when the electric field is pointing downward (negative y). This implies that the vortices will accelerate downward

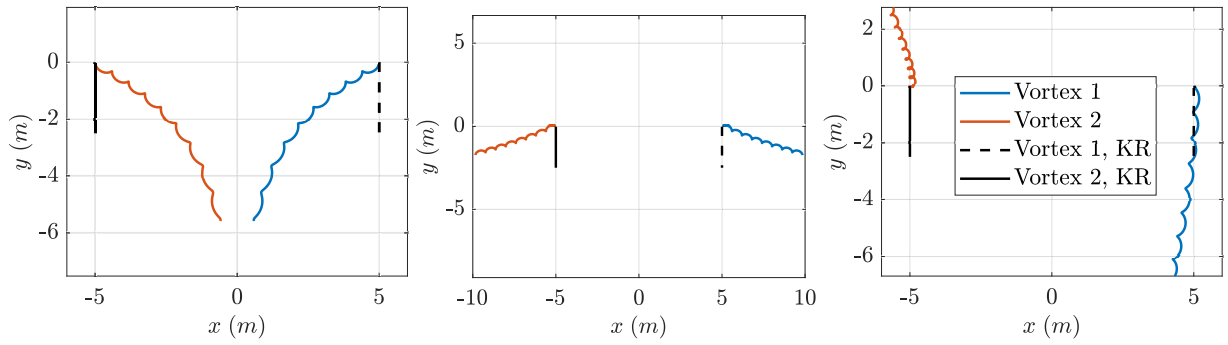

(a) (b) (c)

Figure 5.5: Different simulations for counter-rotating pair of vortices with same charge placed in a constant-strength electric field. Simulations are initialized by the Biot-Savart induced velocity and electric field direction for each case is listed as: (a) $\boldsymbol{E} \downarrow$, (b) $\boldsymbol{E} \uparrow$ and (c) $\boldsymbol{E} \rightarrow$.

beyond the KR value dictated by the Biot-Savart law, which will in turn cause an acceleration in the x-direction because of the term $\dot{y}_i\Gamma_i$ in eq. (5.22). As a result, the two counter-rotating vortices attract towards one other. Note that the simulation should not be deemed valid when the vortices get very close to each other. On the other hand, reversing the direction of the electric field (i.e., opposite to the KR velocity), the KR y-motion is decelerated, leading the counter-rotating vortices to repel, as shown in fig. 5.5b. Interestingly, applying an electric field in the horizontal direction ($+x$), we obtain the response in fig. 5.5c, which is non-intuitive. Although the applied electric force is in the x-direction, the net effect is much more significant in the y-direction. Moreover, even the effect in the x-motion is counter-intuitive; both vortices drift in the negative x-axis (opposite to the direction of the applied electric force). At the beginning, there is an acceleration for both vortices in the x-direction. However, the slightest velocity in x activates the term $-\dot{x}_i\Gamma_i$ in the $\ddot{y}_i$ eq. (5.23), which causes a downward acceleration for the right vortex and an upward acceleration for the left vortex (of negative strength). These vertical accelerations, in turn, affect the x-motion through the term $\dot{y}_i\Gamma_i$ in eq. (5.22), causing both vortices to drift to the left (opposite to the applied force). This interesting interaction between the motion induced by the electric force and the motion induced by the *vortex force* ($\dot{y}_i\Gamma_i$,-$\dot{x}_i\Gamma_i$) is naturally captured in the developed dynamic model. Although the KR motion is not really relevant here, it is presented for comparison in figs. 5.5 and 5.6. It is not intended to pitfall the resulting KR motion with comparing it the new variational model

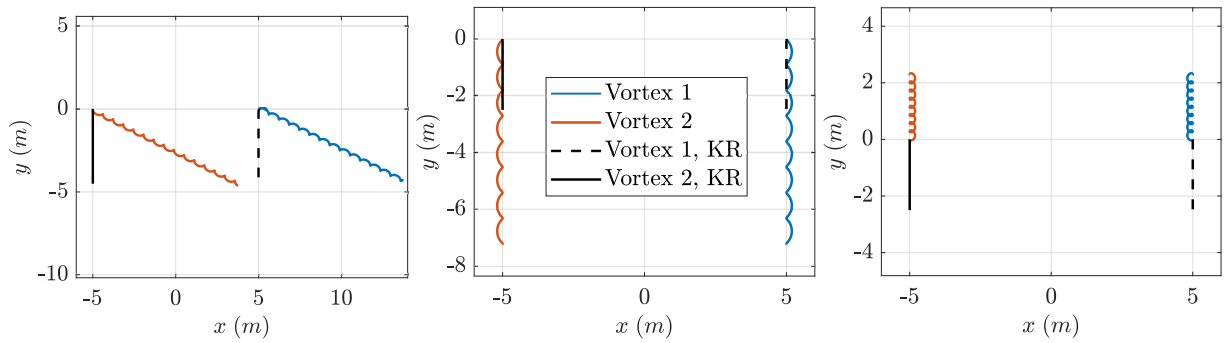

(a) (b) (c)

Figure 5.6: Different simulations for counter-rotating pair of vortices with opposite charge placed in a constant-strength electric field. Simulations are initialized by the Biot-Savart induced velocity; electric field direction and charge sign for each case are listed as: (a) $\boldsymbol{E} \uparrow$, $+q_1$ and $-q_2$, (b) $\boldsymbol{E} \rightarrow$, $+q_1$ and $-q_2$ and (c) $\boldsymbol{E} \rightarrow$, $-q_1$ and $+q_2$.

dynamics, it is presented to facilitate explaining the new dynamics in comparison with the ordinary KR motion, because the KR on its own does not have the capability of predicting the interaction between the hydrodynamic and elector-dynamic forces.

Figure 5.6 shows the motion of a pair of counter-rotating vortices of equal strength, but of equal and opposite charges placed in a constant-strength electric field. Figure 5.6a shows the response to an upward electric field causing an upward force on the right vortex (with positive charge) and a downward force on the left vortex (with negative charge). Yet, both vortices move downward and the significant effect is a drift in the x-direction due to the interaction mentioned above: the downward acceleration of the left vortex causes an acceleration in the x-direction through the term $\dot{y}_i\Gamma_i$ in eq. (5.22), which in turn causes an upward acceleration through the term $-\dot{x}_i\Gamma_i$ in eq. (5.23). Similar behavior occurs with the right vortex; initially, it experiences an upward acceleration from the electric force, which causes an x-acceleration through the term $\dot{y}_i\Gamma_i$ in eq. (5.22). This x-motion, in turn, causes a negative y-acceleration through the term $-\dot{x}_i\Gamma_i$ in eq. (5.23). As a result, the right vortex, though forced by an upward force, moves to the right and downward, which is quite a non-intuitive behavior.

Figure 5.6b shows the response to an electric field in the x-direction, causing a right force on the right

vortex and a left force on the left vortex (with the opposite charge); i.e., pulling the vortices away from each other. However, no considerable net effect is observed in contrast to the other scenarios. The initial right motion of the right vortex due to the electric force causes a downward acceleration, which in turn causes a negative x-acceleration that opposes the electrodynamic acceleration. The situation leads to an equilibrium with a periodic solution close to the KR motion. The behavior in fig. 5.6c is quite interesting, which presents the motion due to an electric field to the left, causing a left force on the right vortex and a right force on the left vortex; i.e., pushing the vortices towards one another. However, the response is counter-intuitive as usual due to the interesting interaction between the electrodynamic force and the hydrodynamic vortex force. Instead of getting closer to each other (to comply with the applied force), the two vortices move upward opposite to their initial KR velocity. As usual, the vortices initially follow the applied electric force (i.e., get closer to one another). This x motion causes an upward acceleration to both vortices, which causes an x-acceleration opposite to the electrodynamic one for both vortices.

The interaction between the electrodynamic force and the vortex force ($\dot{y}_i\Gamma_i$ in the x-direction and $-\dot{x}_i\Gamma_i$ in the y-direction) leads to very interesting behaviors: when pulling vortices downward (i.e., in the same direction as their KR initial velocity), they attract (fig. 5.5a); when pulling them upward (i.e., opposite to their KR initial velocity), they repel (fig. 5.5b); when they are pushed together to the right, they both end up moving to the left with one upward and one downward (fig. 5.5c); when pulling them away from each other, they almost did not respond (fig. 5.6b); and when pushing them towards one another, they move upward (fig. 5.6c). It is quite non-intuitive, yet explainable from the physics of the dynamic model in eqs. (5.22) and (5.23). This nonlinear behavior presents the dynamic model (5.22, 5.23) as a rich mechanical system for geometric mechanics and control analysis using Lie brackets [Bullo and Lewis, 2019, Hassan and Taha, 2019, Taha et al., 2021] where the concepts of *anholonomy* [Baillieul and Lehman, 1996], geometric phases [Marsden et al., 1991, Marsden, 1997], and nonlinear controllability [Hassan and Taha, 2017, Taha et al., 2021] can be demonstrated.

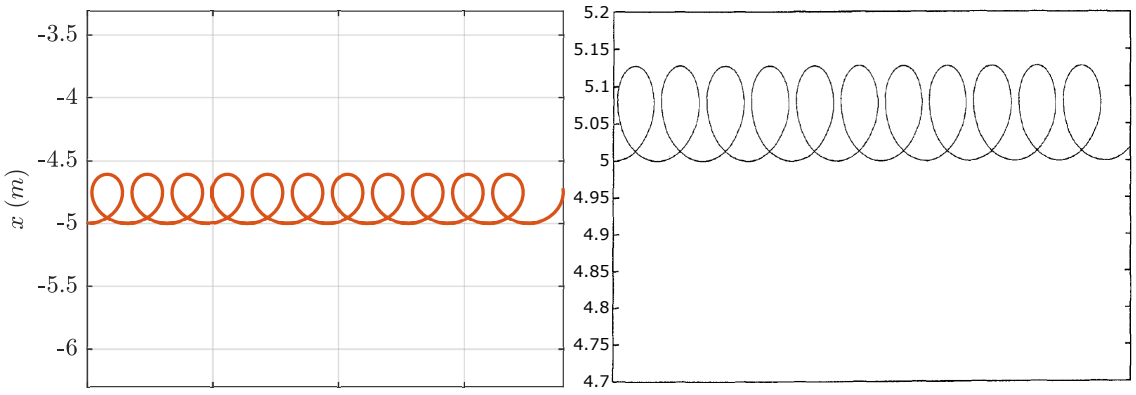

(a) (b)

Figure 5.7: Comparison between the proposed variational vortex dynamics model and the model of Ragazzo et al. [1994] when vortices are initialized with a velocity different from the Biot-Savart induced velocity. (a) Simulation of counter-rotating pair initialized with five multiples of the Biot-Savart induced velocity, showing only one vortex. (b) Counter-rotating pair simulated as a single vortex in the half-plane [Ragazzo et al., 1994].

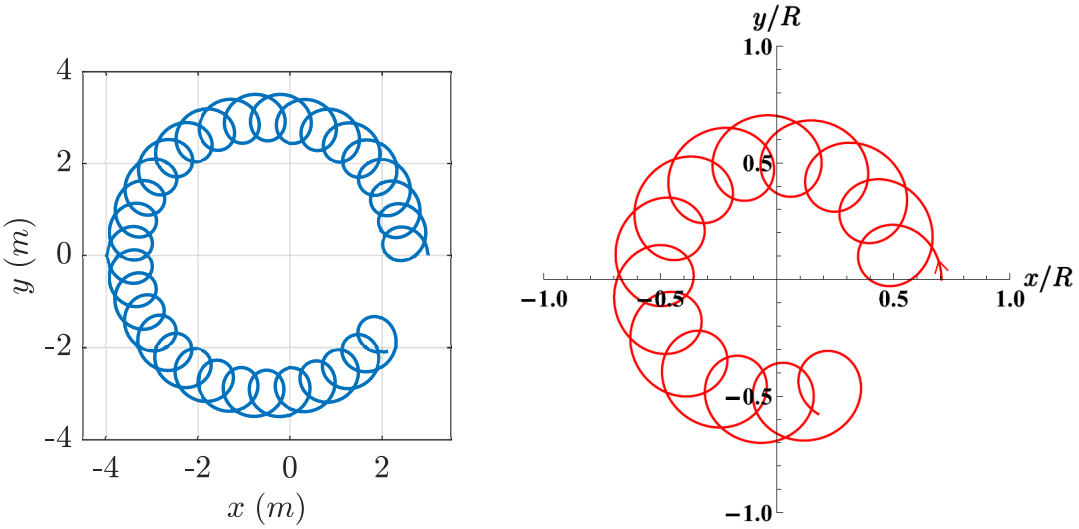

(a) (b)

Figure 5.8: Comparison between the proposed variational vortex dynamics model and Richaud et al. [2021] model. Vortices are initialized with a velocity different from the Biot-Savart induced velocity. (a) Simulation of co-rotating pair initialized with $u_{1_0} = (0i, 5.83j)$ and $u_{2_0} = (0i, 4.16j)$, showing only the first vortex on the right-hand-side. (b) Single vortex simulated in a confined circular domain [Richaud et al., 2021].

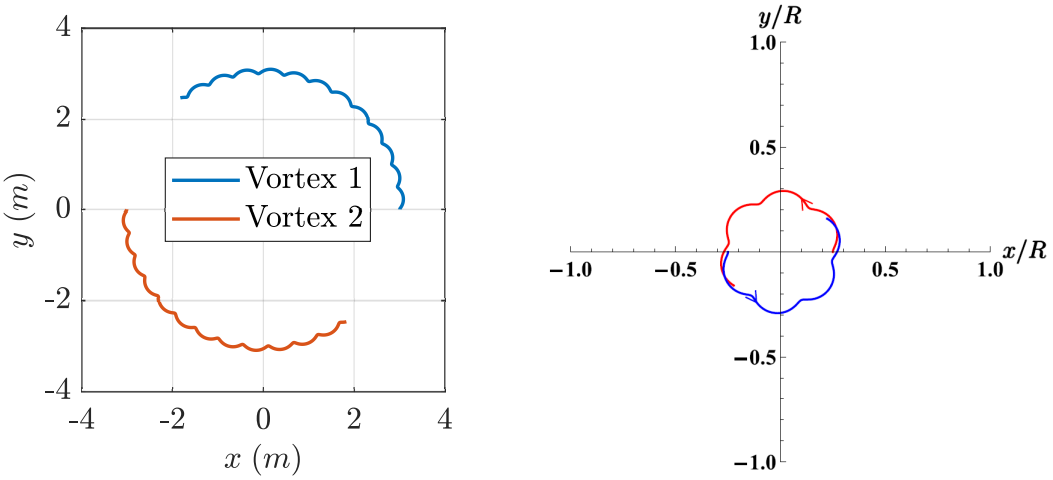

Figure 5.9: Comparison between the proposed variational vortex dynamics model and Richaud et al. [2021] model when vortices are initialized with a velocity different from the Biot-Savart induced velocity. (a) Simulation of co-rotating pair initialized with $u_{1_0} = (-0.5i, 0.83j)$ and $u_{2_0} = (0.5i, -0.83j)$. (b) Co-rotating vortices initially perturbed with a radial velocity in the inward direction [Richaud et al., 2021]

5.4 Comparison with Previous Efforts

In this section, the resulting dynamics from the proposed variational formulation is compared against available data from the literature, particularly the results of Ragazzo et al. [1994] and Richaud et al. [2021, 2022]. The current comparison is established on the fact that the results of Richaud et al. [2021, 2022] using the Hamiltonian proposed by Ragazzo et al. [1994] were validated against direct numerical simulation of the GP equation for a super-fluid (i.e., an inviscid fluid). Hence, the results of Ragazzo et al. [1994] are deemed credible according to the validation against direct numerical simulations of GP. Nevertheless, the Hamiltonian adopted by Ragazzo et al. [1994] and Richaud et al. [2021, 2022] was devised based on analogy with electrodynamics and was not formally derived from variational principles of classical fluid mechanics, in contrast to the current effort. As mentioned before, the proposed variational model recovers the KR dynamics for core-less and massless vortices when the vortices are initialized with the Biot-Savart induced velocity. However, as shown in section 5.3, the proposed model introduces intriguing dynamics when initialized with various velocities, and when body forces are included. For instance, if core-

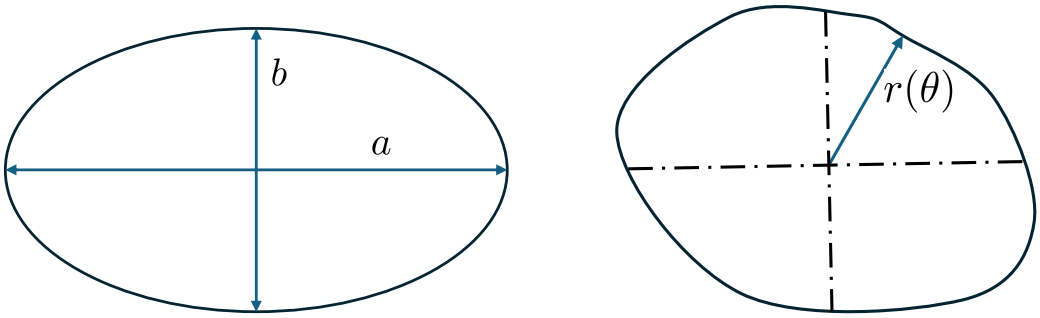

(a) (b)

Figure 5.10: Different vortex core shape parameterization. (a) Cartesian parameterization based on vortex patches ellipses mode shapes. (b) Generic parameterization in polar co-ordinates.

less but massive, point-vortices are considered (in this case, the integrals $I_{x_{ij}}, I_{y_{ij}}$ vanish, but the core mass m_i is retained), then the resulting dynamics could be compared against Ragazzo et al. [1994]. Interestingly, the resulting equations of motion along with the Hamiltonian (see appendix C) from the proposed variational model reduce to those deduced by Ragazzo et al. [1994]. The similarity between the equations of motions and the Hamiltonian between the two approaches is reinforced by the matched trajectories, as shown in fig. 5.7. Moreover, resulting dynamics are compared against Richaud et al. [2021] in figs. 5.8 and 5.9, highlighting almost exact matching. The recovery of the proposed formulation to the special cases of the KR formulation, Ragazzo's and Richaud's provides credibility to the presented approach.

5.5 Future Directions

This section relaxes most of the previously invoked constraint over the cases studies and discusses the future direction for the current formulation model. It is well noted before that the vortices are assumed to have rigid boundary, as a consequences, the vortices are not allowed to come into near vicinity of each other and because the vortices should deform in this situation. As a relaxation to this assumption, vortices could be allowed to deform by assuming family of ellipses shapes in Cartesian x, y that deform by changing a, b, or even a generic parameterization in polar r, θ coordinates

that allows for more shape modes as represented in fig. 5.10. The ellipses parameterization was considered based on each of Saffman [1992], Saffman and Szeto [1980] efforts where they showed that the most dominant mode shapes for deforming vortex patches are ellipses. The new Lagrangian will take account the new parameters included in the parameterization as general co-ordinates. The new invoked parameter for shape deformation will affect the core Lagrangian (mainly the moment of inertia term) and will have their one ODE that describes their dynamics.

Another constraint was forced on the current case studies was the constant strength. This constraint resulted in having the $\dot{\theta}$ co-ordinate in the equations of motion to be ignorable co-ordinate. However, if the vortex strength Γ_i is allowed to be a function of time, then the $\dot{\theta}$ co-ordinate will not be ignorable any more and its dynamics must be taken into account. Then, a separate equation for the time dynamics of Γ_i will be included along with the equation of motion describing the vortex motion. This extension will allow the comparison between current unsteady aerodynamic literature. Most of these model extensions are a straight forward implementation, and they did not needed a complete reformulation of the model to specifically suite the case of interest as it was shown before in previously mentioned efforts. This strength of the model stems out from the formal variational analysis and derivation in fluid mechanics that was adopted while laying the model foundation.

Chapter 6

Conclusion

The hypothesis that dynamic stall possesses a three-dimensional nature was tested through various simulations (URANS, DDES, and IDDES) of a pitching NACA 0012 airfoil. The findings revealed that the lift coefficient from a 3D simulation was more consistent with experimental data compared to results from a 2D simulation. URANS, due to its averaging of turbulent scales, failed to capture key features of the dynamic stall phenomenon, leading to discrepancies between numerical and experimental lift coefficients, particularly at the maximum value and the onset of the downstroke. Conversely, both DDES and IDDES performed better than URANS. The LES solver in these simulations captured additional turbulent scales across the flow field, with a significant increase in the IDDES due to WMLES. The intricate dynamics of DSV creation, characterized by the interaction of multiple LEVs and the TSV, were only evident in the IDDES simulation, resulting in an almost exact match of the numerical lift coefficient time histories with the experimental data for 85% of the cycle. These findings collectively support the argument that, despite dynamic stall being studied for a 2D infinite airfoil, the flow physics are inherently three-dimensional. This underscores the fact that the dynamic stall phenomenon is intrinsically three-dimensional.

In terms of the variational efforts, we introduced the use of Hamilton's principle of least action

to develop a variational formulation for vortex dynamics. The developed model is fundamentally different from previous models in the literature, which are typically devised to recover a pre-known set of ODEs that are first-order in position. In fact, they provide a Hamiltonian formulation of the vortex motion induced by the Biot-Savart law. In contrast, the new model is based on formal variational principles for a continuum of inviscid fluid. As such, the model is dynamic in nature, constituting of second-order ODEs in position, which allows arbitrary initial velocities and external forces (e.g., electromagnetic). The model provided rich and intriguing dynamics for counter and co-rotating vortex pairs. In the limit to a vanishing core size, the Biot-Savart behavior is recovered. For a finite core size, there is a multi-time-scale behavior: a slow dynamics that resembles the Biot-Savart motion, and a fast dynamics that results in rapid oscillations around the Biot-Savart motion. However, for some given initial conditions, the averaged motion is considerably different from the Biot-Savart motion. The situation becomes interesting when an electric field is applied to a charged particle inside the vortex core. In this case, the interaction between the electrodynamic force and the hydrodynamic vortex force leads to non-intuitive behavior. For example, when a pair of counter-rotating vortices were pulled away from each other by the electric force, they moved normal to this force and opposite to their initial Biot-Savart motion; and when they were pulled in the same direction of their initial velocity, they attract to one another (normal to the applied force). This interesting nonlinear dynamics present the developed dynamical model as a rich example in geometric mechanics and control where concepts of anholonomy, geometric phases, and nonlinear controllability can be demonstrated. The dynamical model is also applicable to three-dimensional flows as long as the flow can be reconstructed from a few set of variables (e.g., location and strength of vortex filaments and rings), which will be tackled in future exploitation of the current variational model.

Bibliography

[1] Serge Vladimirovich Alekseenko, Pavel Anatolevich Kuibin, and Valeri Leonidovich Okulov. *Theory of concentrated vortices: an introduction*. Springer Science & Business Media, 2007.

[2] Hassan Aref. Motion of three vortices. *The Physics of Fluids*, 22(3):393–400, 1979.

[3] Hassan Aref. Integrable, chaotic, and turbulent vortex motion in two-dimensional flows. *Annual Review of Fluid Mechanics*, 15(1):345–389, 1983.

[4] Hassan Aref. Stirring by chaotic advection. *Journal of fluid mechanics*, 143:1–21, 1984.

[5] Hassan Aref. Three-vortex motion with zero total circulation: Addendum. *Zeitschrift für angewandte Mathematik und Physik ZAMP*, 40(4):495–500, 1989.

[6] Hassan Aref. Point vortex dynamics: a classical mathematics playground. *Journal of mathematical Physics*, 48(6):065401, 2007.

[7] Hassan Aref and Neil Pomphrey. Integrable and chaotic motions of four vortices. *Physics Letters A*, 78(4):297–300, 1980.

[8] Hassan Aref and Neil Pomphrey. Integrable and chaotic motions of four vortices. i. the case of identical vortices. *Proceedings of the Royal Society of London. A. Mathematical and Physical Sciences*, 380(1779):359–387, 1982.

[9] Hassan Aref and Mark A Stremler. Four-vortex motion with zero total circulation and impulse. *Physics of Fluids*, 11(12):3704–3715, 1999.

[10] Hassan Aref, Nicholas Rott, and Hans Thomann. Gröbli's solution of the three-vortex problem. *Annual Review of Fluid Mechanics*, 24(1):1–21, 1992.

[11] J. Baillieul and B. Lehman. Open-loop control using oscillatory inputs. *CRC Control Handbook*, pages 967–980, 1996.

[12] GK Batchelor. *An introduction to fluid dynamics*. Cambridge university press, 1967.

[13] Harry Bateman. Notes on a differential equation which occurs in the two-dimensional motion of a compressible fluid and the associated variational problems. *Proceedings of the Royal Society of London. Series A, Containing Papers of a Mathematical and Physical Character*, 125(799):598–618, 1929.

[14] SI Benton and MR Visbal. The onset of dynamic stall at a high, transitional reynolds number. *Journal of Fluid Mechanics*, 861:860–885, 2019.

[15] Victor L Berdichevsky. Variational principles. In *Variational Principles of Continuum Mechanics*, pages 3–44. Springer, 2009.

[16] Alexey V Borisov, Ivan S Mamaev, and Sergey M Ramodanov. Dynamic interaction of point vortices and a two-dimensional cylinder. *Journal of mathematical physics*, 48(6):065403, 2007.

[17] Alexey Vladimirovich Borisov and Ivan Sergeevich Mamaev. Integrability of the problem of the motion of a cylinder and a vortex in an ideal fluid. *Mathematical Notes*, 75(1):19–22, 2004.

[18] Alexey Vladimirovich Borisov, Ivan Sergeevich Mamaev, and Sergei M Ramodanov. Motion of a circular cylinder and n point vortices in a perfect fluid. *arXiv preprint nlin/0502029*, 2005.

[19] AV Borisov, IS Mamaev, and SM Ramodanov. Dynamics of a circular cylinder interacting with point vortices. *Discrete & Continuous Dynamical Systems-B*, 5(1):35, 2005.

[20] Francis P Bretherton. A note on hamilton's principle for perfect fluids. *Journal of Fluid Mechanics*, 44(1):19–31, 1970.

[21] CE Brown and WH Michael. Effect of leading-edge separation on the lift of a delta wing. *Journal of the Aeronautical Sciences*, 21(10):690–694, 1954.

[22] Francesco Bullo and Andrew D Lewis. *Geometric control of mechanical systems: modeling, analysis, and design for simple mechanical control systems*, volume 49. Springer, 2019.

[23] Ulf Bunge, Charles Mockett, and Frank Thiele. Guidelines for implementing detached-eddy simulation using different models. *Aerospace Science and Technology*, 11(5):376–385, 2007.

[24] John A Burns. *Introduction to the calculus of variations and control with modern applications*. CRC Press, 2013.

[25] Lawrence W Carr. Progress in analysis and prediction of dynamic stall. *Journal of aircraft*, 25(1):6–17, 1988.

[26] David MF Chapman. Ideal vortex motion in two dimensions: symmetries and conservation laws. *Journal of Mathematical Physics*, 19(9):1988–1992, 1978.

[27] Alfred Clebsch. Ueber die integration der hydrodynamischen gleichungen. 1859.

[28] Georges-Henri Cottet, Petros D Koumoutsakos, et al. *Vortex methods: theory and practice*, volume 8. Cambridge university press Cambridge, 2000.

[29] Chris C Critzos, Harry H Heyson, and Robert W Boswinkle Jr. Aerodynamic characteristics of naca 0012 airfoil section at angles of attack from 0 deg to 180 deg. Technical report, NATIONAL AERONAUTICS AND SPACE ADMINISTRATION WASHINGTON DC, 1955.

[30] Darren Crowdy. *Solving problems in multiply connected domains*. SIAM, 2020.

[31] Russell M Cummings, Scott A Morton, and David R McDaniel. Experiences in accurately predicting time-dependent flows. *Progress in Aerospace Sciences*, 44(4):241–257, 2008.

[32] Dipan Deb, Pawan Shetty, Kamal Poddar, and Sanjay Kumar. Flow induced oscillation of two rigid rectangular plates in a side-by-side configuration. *Journal of Fluids and Structures*, 99:103133, 2020.

[33] Gary S Deem and Norman J Zabusky. Vortex waves: Stationary" v states," interactions, recurrence, and breaking. *Physical Review Letters*, 40(13):859, 1978.

[34] Carlos R dos Santos, Douglas RQ Pacheco, Haithem E Taha, and Mohamed Y Zakaria. Nonlinear modeling of electro-aeroelastic dynamics of composite beams with piezoelectric coupling. *Composite Structures*, 255:112968, 2021.

[35] Bruno Eckhardt and Hassan Aref. Integrable and chaotic motions of four vortices ii. collision dynamics of vortex pairs. *Philosophical Transactions of the Royal Society of London. Series A, Mathematical and Physical Sciences*, 326(1593):655–696, 1988.

[36] Ahmed I El-Nadi, Nabil M Khalifa, and Haitham E Taha. Compressible unsteady aerodynamic loads on oscillating airfoils in a subsonic flow. In *AIAA SCITECH 2022 Forum*, page 1980, 2022.

[37] Jeff D Eldredge. *Mathematical Modeling of Unsteady Inviscid Flows*. Springer, 2019.

[38] Gregory L Eyink. Stochastic least-action principle for the incompressible navier–stokes equation. *Physica D: Nonlinear Phenomena*, 239(14):1236–1240, 2010.

[39] Moatasem Fouda, Nabil M Khalifa, Mahmoud M Rashad, Mingdong Shao, Mostafa Elsharif, and Haitham E Taha. Static and dynamic characteristics of the aerodynamic forces on pitching airfoils between 0 to 360 degrees angle of attack. In *AIAA SCITECH 2022 Forum*, page 1663, 2022.

[40] Hiroki Fukagawa and Youhei Fujitani. A variational principle for dissipative fluid dynamics. *Progress of Theoretical Physics*, 127(5):921–935, 2012.

[41] Chad R Galley, David Tsang, and Leo C Stein. The principle of stationary nonconservative action for classical mechanics and field theories. *arXiv preprint arXiv:1412.3082*, 2014.

[42] François Gay-Balmaz and Hiroaki Yoshimura. A lagrangian variational formulation for nonequilibrium thermodynamics. part ii: continuum systems. *Journal of Geometry and Physics*, 111:194–212, 2017.

[43] Kobra Gharali and David A Johnson. Dynamic stall simulation of a pitching airfoil under unsteady freestream velocity. *Journal of Fluids and Structures*, 42:228–244, 2013.

[44] Hermann Glauert. *The elements of aerofoil and airscrew theory*. Cambridge university press, 1926.

[45] Konrad A Goc, Oriol Lehmkuhl, George Ilhwan Park, Sanjeeb T Bose, and Parviz Moin. Large eddy simulation of aircraft at affordable cost: a milestone in computational fluid dynamics. *Flow*, 1, 2021.

[46] Herbert Goldstein, Charles Poole, and John Safko. Classical mechanics, 2002.

[47] Diogo Aguiar Gomes. A variational formulation for the navier-stokes equation. *Communications in mathematical physics*, 257(1):227–234, 2005.

[48] Cody Gonzalez and Haithem E Taha. A variational theory of lift. *Journal of Fluid Mechanics*, 941, 2022.

[49] Mikhail S Gritskevich, Andrey V Garbaruk, Jochen Schütze, and Florian R Menter. Development of ddes and iddes formulations for the k-ω shear stress transport model. *Flow, turbulence and combustion*, 88(3):431–449, 2012.

[50] Walter Gröbli. *Specielle Probleme über die Bewegung geradliniger paralleler Wirbelfäden*, volume 8. Druck von Zürcher und Furrer, 1877.

[51] Rohit Gupta and Phillip J Ansell. Investigation of the effects of reynolds number on the unsteady flow physics of airfoil dynamic stall. In *2018 AIAA Aerospace Sciences Meeting*, page 0354, 2018.

[52] Ole Hald and Vincenza Mauceri Del Prete. Convergence of vortex methods for euler's equations. *Mathematics of Computation*, 32(143):791–809, 1978.

[53] Ole H Hald. Convergence of vortex methods for euler's equations. ii. *SIAM Journal on Numerical Analysis*, 16(5):726–755, 1979.

[54] R Hargreaves. Xxxvii. a pressure-integral as kinetic potential. *The London, Edinburgh, and Dublin Philosophical Magazine and Journal of Science*, 16(93):436–444, 1908.

[55] Ahmed M Hassan and Haithem E Taha. Geometric control formulation and nonlinear controllability of airplane flight dynamics. *Nonlinear Dynamics*, 88:2651–2669, 2017.

[56] Ahmed M Hassan and Haithem E Taha. Differential-geometric-control formulation of flapping flight multi-body dynamics. *Journal of Nonlinear Science*, 29:1379–1417, 2019.

[57] Ahmed M Hassan and Haithem E Taha. Design of a nonlinear roll mechanism for airplanes using lie brackets for high alpha operation. *IEEE Transactions on Aerospace and Electronic Systems*, 57(1):462–475, 2020.

[58] H von Helmholtz. Über integrale der hydrodynamischen gleichungen, welche den wirbelbewegungen entsprechen. 1858.

[59] H von Helmholtz. Lxiii. on integrals of the hydrodynamical equations, which express vortex-motion. *The London, Edinburgh, and Dublin Philosophical Magazine and Journal of Science*, 33(226):485–512, 1867.

[60] JW Herivel. The derivation of the equations of motion of an ideal fluid by hamilton's principle. In *Mathematical Proceedings of the Cambridge Philosophical Society*, volume 51, pages 344–349. Cambridge University Press, 1955.

[61] Julian CR Hunt, Alan A Wray, and Parviz Moin. Eddies, streams, and convergence zones in turbulent flows. *Studying turbulence using numerical simulation databases, 2. Proceedings of the 1988 summer program*, 1988.

[62] Ahmed A Hussein, Haithem E Taha, Saad Ragab, and Muhammad R Hajj. A variational approach for the dynamics of unsteady point vortices. *Aerospace Science and Technology*, 78:559–568, 2018.

[63] Ahmed A Hussein, Ahmed E Seleit, Haithem E Taha, and Muhammad R Hajj. Optimal transition of flapping wing micro-air vehicles from hovering to forward flight. *Aerospace Science and Technology*, 90:246–263, 2019.

[64] Daniel T Kennedy and Robert A Van Gorder. Motion of open vortex-current filaments under the biot–savart model. *Journal of Fluid Mechanics*, 836:532–559, 2018.

[65] RR Kerswell. Variational principle for the navier-stokes equations. *Physical Review E*, 59 (5):5482, 1999.

[66] Nabil M Khalifa. Geometric representation for euler's equation, 2019. URL `http://dx.doi.org/10.13140/RG.2.2.10279.36008`.

[67] Nabil M Khalifa, Amir S Rezaei, and Haitham E Taha. Comparing the performance of different turbulence models in predicting dynamic stall. In *AIAA Scitech 2021 Forum*, page 1651, 2021.

[68] Gustav Kirchhoff and Kurt Hensel. *Vorlesungen über mathematische Physik*, volume 1. Druck und Verlag von BG Teubner, 1883.

[69] Andrey Kozelkov, Vadim Kurulin, Vladislav Emelyanov, Elena Tyatyushkina, and Konstantin Volkov. Comparison of convective flux discretization schemes in detached-eddy simulation of turbulent flows on unstructured meshes. *Journal of Scientific Computing*, 67(1):176–191, 2016.

[70] Horace Lamb. *Hydrodynamics*. University Press, 1924.

[71] Cornelius Lanczos. The variational principles of mechanics. In *The Variational Principles of Mechanics*. University of Toronto press, 2020.

[72] Jesper Winther Larsen, Søren RK Nielsen, and Steen Krenk. Dynamic stall model for wind turbine airfoils. *Journal of Fluids and Structures*, 23(7):959–982, 2007.

[73] Johan Larsson, Soshi Kawai, Julien Bodart, and Ivan Bermejo-Moreno. Large eddy simulation with modeled wall-stress: recent progress and future directions. *Mechanical Engineering Reviews*, 3(1):15–00418, 2016.

[74] T Lee and P Gerontakos. Investigation of flow over an oscillating airfoil. *Journal of Fluid Mechanics*, 512:313–341, 2004.

[75] Gordon J Leishman. *Principles of helicopter aerodynamics with CD extra*. Cambridge university press, 2006.

[76] Anthony Leonard. Vortex methods for flow simulation. *Journal of Computational Physics*, 37(3):289–335, 1980.

[77] CC Lin. On the motion of vortices in two dimensions: I. existence of the kirchhoff-routh function. *Proceedings of the National Academy of Sciences of the United States of America*, 27(12):570, 1941.

[78] CC Lin. On the motion of vortices in two dimensions-ii some further investigations on the kirchhoff-routh function. *Proceedings of the National Academy of Sciences of the United States of America*, pages 575–577, 1941.

[79] CC Lin. Hydrodynamics of helium ii. Technical report, Massachusetts Inst. of Tech., Cambridge, 1961.

[80] Maria I Loffredo. Eulerian variational principle for ideal hydrodynamics and two-fluid representation. *Physics Letters A*, 135(4-5):294–297, 1989.

[81] Jon Christian Luke. A variational principle for a fluid with a free surface. *Journal of Fluid Mechanics*, 27(2):395–397, 1967.

[82] JE Marsden, OM O'Reilly, FJ Wicklin, and BW Zombros. Symmetry, stability, geometric phases, and mechanical integrators. *Nonlinear Science Today*, 1(1):4–11, 1991.

[83] Jerrold E Marsden. Geometric foundations of motion and control. In *Motion, Control, and Geometry: Proceedings of a Symposium, Board on Mathematical Science, National Research Council Education, National Academies Press, Washington, DC*, 1997.

[84] Guillaume Martinat, Marianna Braza, Yannick Hoarau, and Gilles Harran. Turbulence modelling of the flow past a pitching naca0012 airfoil at 105 and 106 reynolds numbers. *Journal of Fluids and Structures*, 24(8):1294–1303, 2008.

[85] J Maxwell. Remarks on the mathematical classification of physical quantities. *Proceedings of the London Mathematical Society*, 1(1):224–233, 1869.

[86] Kenneth W McAlister, Lawrence W Carr, and William J McCroskey. Dynamic stall experiments on the naca 0012 airfoil. Technical report, 1978.

[87] William J McCroskey. The phenomenon of dynamic stall. Technical report, National Aeronuatics and Space Administration Moffett Field Ca Ames Research . . . , 1981.

[88] William J McCroskey. Unsteady airfoils. *Annual review of fluid mechanics*, 14(1):285–311, 1982.

[89] William J McCroskey, Lawrence W Carr, and Kenneth W McAlister. Dynamic stall experiments on oscillating airfoils. *Aiaa Journal*, 14(1):57–63, 1976.

[90] MV Melander, NJ Zabusky, and AS Styczek. A moment model for vortex interactions of the two-dimensional euler equations. part 1. computational validation of a hamiltonian elliptical representation. *Journal of Fluid Mechanics*, 167:95–115, 1986.

[91] Vyacheslav V Meleshko and Hassan Aref. A bibliography of vortex dynamics 1858-1956. *Advances in Applied Mechanics*, 41(197):197–292, 2007.

[92] Florian R Menter. Two-equation eddy-viscosity turbulence models for engineering applications. *AIAA journal*, 32(8):1598–1605, 1994.

[93] Florian R Menter. Best practice: scale-resolving simulations in ansys cfd. *ANSYS Germany GmbH*, 1, 2012.

[94] FR Menter and M Kuntz. Adaptation of eddy-viscosity turbulence models to unsteady separated flow behind vehicles. In *The aerodynamics of heavy vehicles: trucks, buses, and trains*, pages 339–352. Springer, 2004.

[95] Sébastien Michelin and Stefan G Llewellyn Smith. An unsteady point vortex method for coupled fluid–solid problems. *Theoretical and Computational Fluid Dynamics*, 23(2):127–153, 2009.

[96] Louis Melville Milne-Thomson. *Theoretical aerodynamics*. Courier Corporation, 1973.

[97] Louis Melville Milne-Thomson. *Theoretical hydrodynamics*. Courier Corporation, 1996.

[98] Charles Mockett. *A Comprehensive Study of Detached Eddy Simulation*. Univerlagtuberlin, 2009.

[99] Philip J Morrison. Hamiltonian description of the ideal fluid. *Reviews of modern physics*, 70(2):467, 1998.

[100] Karen Mulleners and Markus Raffel. The onset of dynamic stall revisited. *Experiments in fluids*, 52(3):779–793, 2012.

[101] Karen Mulleners and Markus Raffel. Dynamic stall development. *Experiments in fluids*, 54 (2):1–9, 2013.

[102] Fady M Najjar and Surya Pratap Vanka. Effects of intrinsic three-dimensionality on the drag characteristics of a normal flat plate. *Physics of fluids*, 7(10):2516–2518, 1995.

[103] Ali H Nayfeh. *Introduction to perturbation techniques*. John Wiley & Sons, 2011.

[104] Ali H Nayfeh and Dean T Mook. *Nonlinear oscillations*. John Wiley & Sons, 2008.

[105] Paul K Newton. *The N-vortex problem: analytical techniques*, volume 145. Springer Science & Business Media, 2013.

[106] Paul K Newton. Point vortex dynamics in the post-aref era. *Fluid Dynamics Research*, 46 (3):031401, 2014.

[107] NV Nikitin, Franck Nicoud, B Wasistho, KD Squires, and Philippe R Spalart. An approach to wall modeling in large-eddy simulations. *Physics of fluids*, 12(7):1629–1632, 2000.

[108] W Olva. The motion of two dimensional vortices with mass as a singular perturbation hamiltonian problem. *New Trends for Hamiltonian Systems and Celestial Mechanics*, 8: 301–310, 1996.

[109] Purvic Patel and Gecheng Zha. Improved delayed detached eddy simulation of separated flow. In *AIAA Aviation 2020 Forum*, page 3013, 2020.

[110] Paul Penfield. Hamilton's principle for fluids. *The Physics of Fluids*, 9(6):1184–1194, 1966.

[111] Justin L Petrilli, Ryan C Paul, Ashok Gopalarathnam, and Neal T Frink. A cfd database for airfoils and wings at post-stall angles of attack. In *31st AIAA Applied Aerodynamics Conference*, page 2916, 2013.

[112] RT Pierrehumbert. A family of steady, translating vortex pairs with distributed vorticity. *Journal of Fluid Mechanics*, 99(1):129–144, 1980.

[113] L Pla Olea and HE Taha. Geometric control analysis of the unsteady aerodynamics of a pitching–plunging airfoil in dynamic stall. *Physics of Fluids*, 36(3), 2024.

[114] Laura Pla Olea, Nabil M Khalifa, and Haitham E Taha. Geometric control study of the beddoes-leishman model in a pitching-plunging airfoil. In *AIAA SCITECH 2022 Forum*, page 2415, 2022.

[115] Stephen B Pope. *Turbulent flows*. Cambridge university press, 2000.

[116] Brandon James Pruski and RDW Bowersox. Leading-edge flow structure of a dynamically pitching naca 0012 airfoil. *AIAA journal*, 51(5):1042–1053, 2013.

[117] DI Pullin. Contour dynamics methods. *Annual review of fluid mechanics*, 24(1):89–115, 1992.

[118] Yunpeng Qin, Qiulin Qu, Peiqing Liu, Yun Tian, and Zhe Lu. Ddes study of the aerodynamic forces and flow physics of a delta wing in static ground effect. *Aerospace Science and Technology*, 43:423–436, 2015.

[119] C Grotta Ragazzo, J Koiller, and WM Oliva. On the motion of two-dimensional vortices with mass. *Journal of Nonlinear Science*, 4(1):375–418, 1994.

[120] Sergey M Ramodanov and Sergey V Sokolov. Dynamics of a circular cylinder and two point vortices in a perfect fluid. *Regular and Chaotic Dynamics*, 26(6):675–691, 2021.

[121] Sergey Mikhailovich Ramodanov. Motion of a circular cylinder and a vortex in an ideal fluid. *Regular and chaotic dynamics*, 6(1):33–38, 2001.

[122] Andrea Richaud, Vittorio Penna, Ricardo Mayol, and Montserrat Guilleumas. Vortices with massive cores in a binary mixture of bose-einstein condensates. *Physical Review A*, 101(1): 013630, 2020.

[123] Andrea Richaud, Vittorio Penna, and Alexander L Fetter. Dynamics of massive point vortices in a binary mixture of bose-einstein condensates. *Physical Review A*, 103(2):023311, 2021.

[124] Andrea Richaud, Pietro Massignan, Vittorio Penna, and Alexander L Fetter. Dynamics of a massive superfluid vortex in r k confining potentials. *Physical Review A*, 106(6):063307, 2022.

[125] Nicholas Rott. Three-vortex motion with zero total circulation. *Zeitschrift für angewandte Mathematik und Physik ZAMP*, 40(4):473–494, 1989.

[126] Nicholas Rott. Constrained three-and four-vortex problems. *Physics of Fluids A: Fluid Dynamics*, 2(8):1477–1480, 1990.

[127] Edward John Routh. Some applications of conjugate functions. *Proceedings of the London Mathematical Society*, 1(1):73–89, 1880.

[128] PG Saffman and R Szeto. Equilibrium shapes of a pair of equal uniform vortices. *The Physics of Fluids*, 23(12):2339–2342, 1980.

[129] Philip G Saffman. *Vortex dynamics*. Cambridge university press, 1992.

[130] Pierre Sagaut. *Large eddy simulation for incompressible flows: an introduction*. Springer Science & Business Media, 2006.

[131] Rick Salmon. Hamiltonian fluid mechanics. *Annual review of fluid mechanics*, 20(1): 225–256, 1988.

[132] Hermann Schlichting, Klaus Gersten, Egon Krause, Herbert Oertel, and Katherine Mayes. *Boundary-layer theory*, volume 7. Springer, 1960.

[133] Robert L Seliger and Gerald Beresford Whitham. Variational principles in continuum mechanics. *Proceedings of the Royal Society of London. Series A. Mathematical and Physical Sciences*, 305(1480):1–25, 1968.

[134] YM Selim, HE Taha, and GM El Bayoumi. Describing function of the nonlinear dynamics of viscous unsteady lift response for a pitching airfoil. *Physics of Fluids*, 35(11), 2023.

[135] James Serrin. Mathematical principles of classical fluid mechanics. In *Fluid Dynamics I/Strömungsmechanik I*, pages 125–263. Springer, 1959.

[136] James A Sethian et al. *Level set methods and fast marching methods*, volume 98. Cambridge Cambridge UP, 1999.

[137] Banavara N Shashikanth, Jerrold E Marsden, Joel W Burdick, and Scott D Kelly. The hamiltonian structure of a two-dimensional rigid circular cylinder interacting dynamically with n point vortices. *Physics of Fluids*, 14(3):1214–1227, 2002.

[138] Mohamed Shorbagy and Haithem Taha. Magnus force estimation using gauss's principle of least constraint. *AIAA Journal*, pages 1–8, 2024.

[139] M Shur, PR Spalart, M Strelets, and A Travin. Detached-eddy simulation of an airfoil at high angle of attack. In *Engineering turbulence modelling and experiments 4*, pages 669–678. Elsevier, 1999.

[140] Mikhail L Shur, Philippe R Spalart, Mikhail Kh Strelets, and Andrey K Travin. A hybrid rans-les approach with delayed-des and wall-modelled les capabilities. *International Journal of Heat and Fluid Flow*, 29(6):1638–1649, 2008.

[141] Kuldeep Singh and José Carlos Páscoa. Numerical modeling of stall and poststall events of a single pitching blade of a cycloidal rotor. *Journal of Fluids Engineering*, 141(1), 2019.

[142] Stefan G Llewellyn Smith. How do singularities move in potential flow? *Physica D: Nonlinear Phenomena*, 240(20):1644–1651, 2011.

[143] Philippe Spalart and Steven Allmaras. A one-equation turbulence model for aerodynamic flows. In *30th aerospace sciences meeting and exhibit*, page 439, 1992.

[144] Philippe R Spalart. Comments on the feasibility of les for wings, and on a hybrid rans/les approach. In *Proceedings of first AFOSR international conference on DNS/LES*. Greyden Press, 1997.

[145] Philippe R Spalart. Strategies for turbulence modelling and simulations. *International Journal of Heat and Fluid Flow*, 21(3):252–263, 2000.

[146] Philippe R Spalart. Detached-eddy simulation. *Annual review of fluid mechanics*, 41: 181–202, 2009.

[147] Philippe R Spalart and Craig Streett. Young-person's guide to detached-eddy simulation grids. 2001.

[148] Philippe R Spalart, Shur Deck, Michael L Shur, Kyle D Squires, M Kh Strelets, and Andrei Travin. A new version of detached-eddy simulation, resistant to ambiguous grid densities. *Theoretical and computational fluid dynamics*, 20(3):181, 2006.

[149] M Strelets. Detached eddy simulation of massively separated flows. In *39th Aerospace sciences meeting and exhibit*, page 879, 2001.

[150] JL Synge. On the motion of three vortices. *Canadian Journal of Mathematics*, 1(3):257–270, 1949.

[151] Haitham Taha and Muhammad Hajj. Unsteady nonlinear aerodynamics of hovering mavs/insects. In *51st AIAA Aerospace Sciences Meeting Including the New Horizons Forum and Aerospace Exposition*, page 504, 2013.

[152] Haithem Taha and Amir S Rezaei. Viscous extension of potential-flow unsteady aerodynamics: the lift frequency response problem. *Journal of Fluid Mechanics*, 868:141–175, 2019.

[153] Haithem Taha, Cody Gonzalez, and Mohamed Shorbagy. A minimization principle for incompressible fluid mechanics. *Physics of Fluids*, 35(12), 2023.

[154] Haithem E Taha and Cody Gonzalez. What does nature minimize in every incompressible flow? *arXiv preprint arXiv:2112.12261*, 2021.

[155] Haithem E Taha and Cody Gonzalez. Refining kutta's flow over a flat plate: Necessary conditions for lift. *AIAA Journal*, 61(5):2060–2068, 2023.

[156] Haithem E Taha and Amir S Rezaei. On the high-frequency response of unsteady lift and circulation: A dynamical systems perspective. *Journal of Fluids and Structures*, 93:102868, 2020.

[157] Haithem E Taha and Amir S Rezaei. State-space modeling of viscous unsteady aerodynamic loads. *AIAA Journal*, 60(4):2251–2265, 2022.

[158] Haithem E Taha, Ahmed Hassan, and Moatasem Fouda. Nonlinear flight physics of the lie bracket roll mechanism. *Nonlinear Dynamics*, 106:1627–1646, 2021.

[159] Haithem E Taha, Laura Pla Olea, Nabil Khalifa, Cody Gonzalez, and Amir S Rezaei. Geometric-control formulation and averaging analysis of the unsteady aerodynamics of a wing with oscillatory controls. *Journal of Fluid Mechanics*, 928:A30, 2021.

[160] Phanindra Tallapragada and Scott David Kelly. Reduced-order modeling of propulsive vortex shedding from a free pitching hydrofoil with an internal rotor. In *2013 American Control Conference*, pages 615–620. IEEE, 2013.

[161] Andrew A Tchieu and Anthony Leonard. A discrete-vortex model for the arbitrary motion of a thin airfoil with fluidic control. *Journal of fluids and structures*, 27(5-6):680–693, 2011.

[162] Hendrik Tennekes and John L Lumley. *A first course in turbulence*. MIT press, 2018.

[163] A Travin, M Shur, MM Strelets, and PR Spalart. Physical and numerical upgrades in the detached-eddy simulation of complex turbulent flows. In *Advances in LES of complex flows*, pages 239–254. Springer, 2002.

[164] Andrei Travin, Michael Shur, Michael Strelets, and Philippe Spalart. Detached-eddy simulations past a circular cylinder. *Flow, turbulence and combustion*, 63(1-4):293–313, 2000.

[165] Andrey K Travin, Mikhail L Shur, Philippe R Spalart, and Mikhail Kh Strelets. Improvement of delayed detached-eddy simulation for les with wall modelling. In *ECCOMAS CFD 2006: Proceedings of the European Conference on Computational Fluid Dynamics, Egmond aan Zee, The Netherlands, September 5-8, 2006*. Delft University of Technology; European Community on Computational Methods . . . , 2006.

[166] Clifford Truesdell. *The kinematics of vorticity*. Indiana University Press, 1954.

[167] Miguel R Visbal. Analysis of the onset of dynamic stall using high-fidelity large-eddy simulations. In *52nd Aerospace Sciences Meeting*, page 0591, 2014.

[168] Miguel R Visbal and Daniel J Garmann. Analysis of dynamic stall on a pitching airfoil using high-fidelity large-eddy simulations. *AIAA Journal*, 56(1):46–63, 2018.

[169] Miguel R Visbal and Daniel J Garmann. Investigation of spanwise end effects on dynamic stall of a pitching wing section. *Journal of Aircraft*, 56(6):2118–2130, 2019.

[170] Chengjie Wang and Jeff D Eldredge. Low-order phenomenological modeling of leading-edge vortex formation. *Theoretical and Computational Fluid Dynamics*, 27(5):577–598, 2013.

[171] Shengyi Wang, Derek B Ingham, Lin Ma, Mohamed Pourkashanian, and Zhi Tao. Numerical investigations on dynamic stall of low reynolds number flow around oscillating airfoils. *Computers & fluids*, 39(9):1529–1541, 2010.

[172] Shengyi Wang, Derek B Ingham, Lin Ma, Mohamed Pourkashanian, and Zhi Tao. Turbulence modeling of deep dynamic stall at relatively low reynolds number. *Journal of Fluids and Structures*, 33:191–209, 2012.

[173] David C Wilcox. Formulation of the kw turbulence model revisited. *AIAA journal*, 46(11): 2823–2838, 2008.

[174] David C Wilcox et al. *Turbulence modeling for CFD*, volume 2. DCW industries La Canada, CA, 1998.

[175] GS Winckelmans and Anthony Leonard. Contributions to vortex particle methods for the computation of three-dimensional incompressible unsteady flows. *Journal of Computational Physics*, 109(2):247–273, 1993.

[176] Jie-Zhi Wu, Hui-Yang Ma, and M-D Zhou. *Vorticity and vortex dynamics*. Springer Science & Business Media, 2007.

[177] Zhimiao Yan, Haithem E Taha, and Muhammad R Hajj. Geometrically-exact unsteady model for airfoils undergoing large amplitude maneuvers. *Aerospace Science and Technology*, 39: 293–306, 2014.

[178] Kunio Yasue. A variational principle for the navier-stokes equation. *Journal of Functional Analysis*, 51(2):133–141, 1983.

[179] Norman J Zabusky, MH Hughes, and KV Roberts. Contour dynamics for the euler equations in two dimensions. *Journal of computational physics*, 30(1):96–106, 1979.

[180] MY Zakaria, HE Taha, and MR Hajj. Measurement and modeling of lift enhancement on plunging airfoils: A frequency response approach. *Journal of Fluids and Structures*, 69: 187–208, 2017.

Appendices

Appendix A

Flow KE Integrals

The two-dimensional KE is given as

$$T = \frac{\rho}{2} \int_A (\nabla \phi)^2 \; dA, \tag{A.1}$$

substituting the following relations

$$u = \frac{\partial \psi}{\partial y}, \quad v = \frac{-\partial \psi}{\partial x}, \quad \omega_z = \frac{\partial v}{\partial x} - \frac{\partial u}{\partial y} = 0, \tag{A.2}$$

and the integral reads as:

$$T = \frac{\rho}{2} \int_A \left(u \frac{\partial \psi}{\partial y} - v \frac{\partial \psi}{\partial x} - \psi \omega_z \right) \; dA = \frac{\rho}{2} \int_A \left(\frac{\partial (u\psi)}{\partial y} - \frac{\partial (v\psi)}{\partial x} \right) \; dA = \frac{\rho}{2} \int_A \psi \omega_z \; dA. \tag{A.3}$$

Equation (A.3) applies for irrotational and rotational flows, however, we restrict the current analysis for irrotational flows only. The KE integral is computed over a multiply-connected domain, and to transform the area integral to a line one using Stokes' theorem, the domain must be transformed to a simply-connected domain by the creation of fictitious barriers, as shown in fig. 5.1. Then, the KE

integral reads as:

$$T = -\frac{\rho}{2} \oint_{R+\sigma_i+c_i} \psi \boldsymbol{u} \cdot \boldsymbol{dl} = -\frac{\rho}{2} \int_{R+\sigma_i+c_i} \psi d\phi. \tag{A.4}$$

The above expression is evaluated over the domain boundaries while taking in consideration the cyclic behavior of the multi-valued function ϕ, and assuming $r_{ij} >> a$. The result is represented as:

$$T = -\frac{\rho}{2} \left[\int_{c_i} \psi d\phi + \int_R \psi d\phi + \int_{\sigma_i} \psi d\phi \right]$$
$$= -\frac{\rho}{2} \left[\sum_{i \neq j} \sum \Gamma_i \psi_j |_i + \sum \Gamma_i \psi_i |_{c_i} + \Psi|_R \Gamma_R + \sum \Gamma_i \Psi|_R \right]. \tag{A.5}$$

Equation (A.5) concludes the KE computation, and further analysis along with more simplifications are discussed in section 5.1.1.

Appendix B

$\partial_t \phi$ Lagrangian Calculation

Equation (5.15) is decomposed into two separate integrals, I_y and I_x

$$\frac{d}{dt}\left(\frac{\partial \mathcal{L}_{\phi_t}}{\partial \dot{x}_i}\right) - \frac{\partial \mathcal{L}_{\phi_t}}{\partial x_i} = \rho \dot{y}_i \Big[\underbrace{\partial_{y_i} \int \partial_{x_i} \phi_i \, dA}_{I_y} - \underbrace{\partial_{x_i} \int \partial_{y_i} \phi_i \, dA}_{I_x} \Big]. \tag{B.1}$$

Relying on the reciprocal property of the potential function ϕ between the parameterization (x, y) co-ordinates and generalized one (x_i, y_i),

$$\partial_{y_i} \phi_i = -\partial_y \phi_i, \qquad \partial_{x_i} \phi_i = -\partial_x \phi_i, \tag{B.2}$$

the I_y integral can be simplified and transformed to a boundary one as:

$$I_y = \partial_{y_i} \int \partial_{x_i} \phi_i \, dA = -\partial_{y_i} \int \partial_x \phi_i \, dx dy = -\partial_{y_i} \int_{\partial} \phi_i \, dy. \tag{B.3}$$

The integral is evaluated for each boundary in fig. 5.1. Without loss of generality, if the barriers are taken parallel to the x axis, then I_y will be

$$I_y = -\partial_{y_i}\left\{\sum_{\substack{j \\ i\neq j}} \int_{c_j} \phi_i \, dy + \int_R \phi_i \, dy + \int_{\sigma_i^+} \phi_i \, dy + \int_{\sigma_i^-} \phi_i \, dy + \int_{c_i} \phi_i \, dy\right\}. \tag{B.4}$$

The last and second integrals will vanish when ϕ_i is treated as a single-valued function after constructing the barriers. Moreover, the third and fourth integrals will vanish, the former because of the barrier location and the latter due to selecting $\phi_i^- = 0$, hence, we are left with the first integral. The differentiation can act over the first integrand because the integral boundary c_j is independent of y_i (i.e., no need for Leibniz rule). The final form of I_y integral is

$$I_y = -\sum_{\substack{j \\ i\neq j}} \int_{c_j} \partial_{y_i}\phi_i \, dy, \tag{B.5}$$

where it is evaluated numerically over the j^{th} vortex boundary.

The I_x integral is computed following the same analysis, and it can be written as

$$I_x = -\partial_{x_i}\left\{\sum_{\substack{j \\ i\neq j}} \int_{c_j} \phi_i \, dx + \int_R \phi_i \, dx + \int_{\sigma_i^+} \phi_i \, dx + \int_{\sigma_i^-} \phi_i \, dx + \int_{c_i} \phi_i \, dx\right\}. \tag{B.6}$$

Again as before, the second, fourth and last term vanishes with the same analogy. However, the third term will not vanish as $\phi_i^+ = 2\pi$, resulting in

$$I_x = -\partial_{x_i}\left\{\sum_{\substack{j \\ i\neq j}} \int_{c_j} \phi_i \, dx + \Gamma_i(r_\infty - x_i - a)\right\} = -\sum_{\substack{j \\ i\neq j}} \int_{c_j} \partial_{x_i}\phi_i \, dx + \Gamma_i. \tag{B.7}$$

The end result can be substituted back in eq. (5.15) to get eq. (5.16).

B.1 Numerical Integration

The numerical evaluation of the terms $I_{x_{ij}}, I_{y_{ij}}$ is given as:

$$I_{x_{ij}} = \frac{\Gamma_i}{2\pi}\Bigg[\int_{x_j+a}^{x_j-a} \frac{-(y_j - \sqrt{a^2-(x-x_j)^2} - y_i)}{(x-x_i)^2 + (y_j - \sqrt{a^2-(x-x_j)^2} - y_i)^2}dx + \int_{x_j-a}^{x_j+a} \frac{-(y_j + \sqrt{a^2-(x-x_j)^2} - y_i)}{(x-x_i)^2 + (y_j + \sqrt{a^2-(x-x_j)^2} - y_i)^2}dx\Bigg], \quad \text{(B.8)}$$

$$I_{y_{ij}} = \frac{\Gamma_i}{2\pi}\Bigg[\int_{y_j+a}^{y_j-a} \frac{x_j + \sqrt{a^2-(y-y_j)^2} - x_i}{(y-y_i)^2 + (x_j + \sqrt{a^2-(y-y_j)^2} - x_i)^2}dx + \int_{y_j-a}^{y_j+a} \frac{x_j - \sqrt{a^2-(y-y_j)^2} - x_i}{(y-y_i)^2 + (x_j - \sqrt{a^2-(y-y_j)^2} - x_i)^2}dx\Bigg]. \quad \text{(B.9)}$$

Appendix C

Comparison with Ragazzo's Hamiltonian

A Hamiltonian formulation for the derived Lagrangian in chapter 5 is computed relying on the Legendre transformation [46]. The transformation is

$$H(\boldsymbol{q}, \boldsymbol{p}, t) = \sum_i \dot{q}_i p_i - L(\boldsymbol{q}, \dot{\boldsymbol{q}}, t), \tag{C.1}$$

where p_i's are the generalized momenta given by:

$$p_i = \frac{\partial L\left(\boldsymbol{q}, \dot{\boldsymbol{q}}, t\right)}{\partial \dot{q}_i}. \tag{C.2}$$

Recall the derived Lagrangian in eq. (5.2) and substitute it into eq. (C.2), then the generalized momenta is

$$p_i = \frac{\partial L_{\phi_t}}{\partial \dot{q}_i} + \sum m_i \dot{q}_i, \tag{C.3}$$

where the first term is determined from eq. (5.12) (whose detailed computation is given in appendix B). The final form for the first term in eq. (C.3) includes a numerical integration over the cores circumferences, as shown in eq. (B.7). To simplify the Legendre transformation analysis,

and to allow for comparison with Ragazzo et al. [119] Hamiltonian, massive-point vortices without cores is considered instead of vortex patches. As a result, the integrals $I_{x_{ij}}$, $I_{y_{ij}}$ defined in (5.17) vanish. By this, and relying on eq. (B.7), eq. (C.3) yields

$$p_i = \sum m_i \dot{q}_i - \Gamma_i \rho \left(q_i \times \boldsymbol{e}_3 \right), \tag{C.4}$$

and the Hamiltonian takes the form

$$\mathcal{H} = \sum \frac{1}{2m_i} \left\| p_i + \Gamma_i \rho \left(q_i \times \boldsymbol{e}_3 \right) \right\|^2 - T. \tag{C.5}$$

Interestingly, the previous results are in agreement with the Hamiltonian and generalized momenta of Ragazzo et al. [119] (there is a sign difference because of the arbitrary sign definition for the stream function) as presented below.

$$\mathbf{p}_j = \sum m_j \mathbf{q}_j + \frac{\Gamma_j \rho}{2} \left(\mathbf{q}_j \times \mathbf{e}_3 \right) \tag{C.6}$$

$$\mathcal{H} = \sum \frac{1}{2m_j} \left\| \mathbf{p}_j - \frac{\Gamma_j \rho}{2} \left(\mathbf{q}_j \times \mathbf{e}_3 \right) \right\|^2 + (-\rho W) \tag{C.7}$$

Also, setting the core size to zero in our formulation (so the integrals $I_{x_{ij}}$, $I_{y_{ij}}$ vanish) while considering non-zero core mass (i.e., considering massive-point vortices), the resulting equations of motion are exactly the same as those by Ragazzo et al. [119].